ISSN: 1847-9286
Open Access Journal
www.jese-online.org

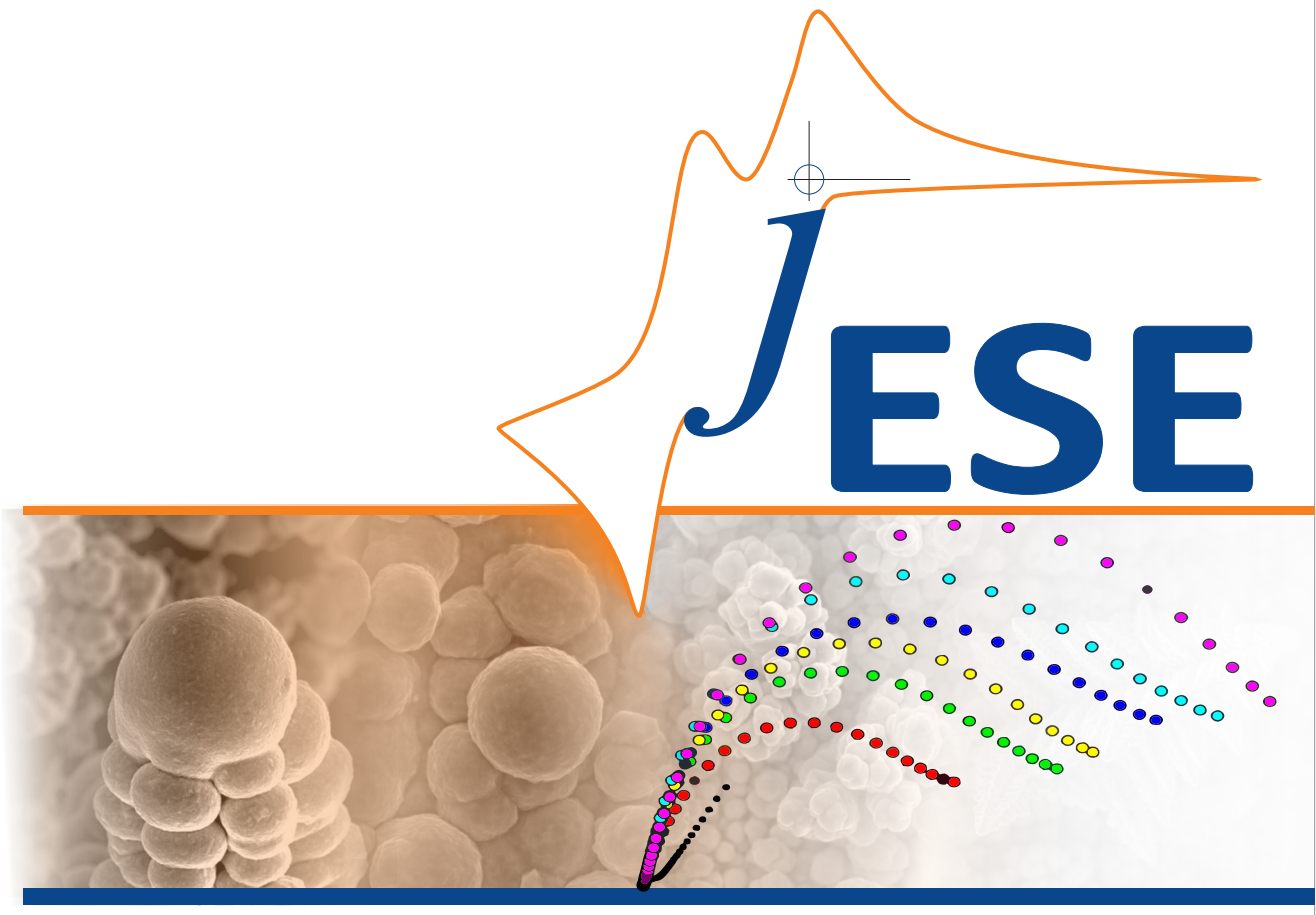

Journal of Electrochemical Science and Engineering

J. Electrochem. Sci. Eng. **8**(**1**) 2018, 1-110

Special Issue dedicated to the
6th Regional Symposium on Electrochemistry – South East Europe

IAPC Publishing

J. Electrochem. Sci. Eng. **8(1)** (2018) 1-2; DOI: http://dx.doi.org/10.5599/jese.513

Open Access : : ISSN 1847-9286

www.jESE-online.org

Editorial

This special issue of the Journal of Electrochemical Science and Engineering (jESE) is dedicated to selected papers contributed to the 6th Regional Symposium on Electrochemistry – South East Europe (RSE–SEE), held in Balatonkenese, Hungary, from 11–15 June 2017. This issue constitutes Part 1 of the proceedings of the Symposium (6 articles). Part 2 will appear in the next issue of jESE.

Following five successful symposia in Croatia (Rovinj, Red Island, 2008), Serbia (Belgrade, 2010), Romania (Bucharest, 2012), Slovenia (Ljubljana, 2013) and Bulgaria (Pravetz, 2015), the 6th Regional Symposium on Electrochemistry – South East Europe (RSE–SEE) was hosted in Hungary, supported by the electrochemical societies of the region. The scientific theme of the meeting "Renaissance of Electrochemistry in the 21st century and its effect on the development of South East Europe" underscored the key role of electrochemistry as a fundamental discipline bringing together *societal needs* from the one side and technology *from the* other side.

Over the past 10 years this series of symposia has attracted an international group of scientists and engineers with broad experience in electrochemical measurement and modeling. Building on already established traditions, RSE-SEE6 crossed regional borders, creating a common platform for scientists and experts from regional and international research and industrial institutions who brought their extensive knowledge, novel ideas, and boundless enthusiasm to the conference venue. More than 110 participants from 24 countries presented papers (66 talks including 4 plenary and 7 keynote lectures, 40 posters) and discussed recent progress during seven sessions (Electrochemical Energy Storage, Batteries, Fuel Cells and Supercapacitors; Analytical Electrochemistry, Sensors and Biosensors, Electrochemistry at Interfaces, Thermodynamic, Kinetic and Methodological Aspects; Electrocatalysis, New, Non-Noble Metal Catalysts, Electrochemistry of New Functional Materials, Conducting Polymers and Composites, General Session).

We would like to acknowledge the financial and other support of the Hungarian Academy of Sciences, the International Society of Electrochemistry, the Furukawa Electric Group, Jászplasztik, Ametek, Zahner, Metrohm, PalmSens, Ivium and Paks Nuclear Power Plant.

We wish to express our gratitude to the members of the Scientific and Organizing Committees for their continued dedication and support.

We would like to sincerely thank the authors for their contribution, the reviewers for their commitment and professional work and the *j*ESE–Editorial Office for their invaluable assistance in the Proceedings publication.

The next (7th) Regional Symposium on Electrochemistry – South East Europe will be held in Croatia in 2019.

***Gyözö G. Láng**, Guest Editor*

Members of the RSE-SEE6 local organizing committee: György **Inzelt** (honorary chairman), Tamás **Pajkossy** and Győző G. **Láng** (co-chairs), Soma **Vesztergom** (secretary).
(Homepage: http://rse-see2017.hu/ . Photos: Dóra Zalka and Krisztina J. Szekeres)

J. Electrochem. Sci. Eng. **8(1)** (2018) 3-37; DOI: http://dx.doi.org/10.5599/jese.448

Open Access : : ISSN 1847-9286

www.jESE-online.org

Review article

Conducting polymers: past, present, future

György Inzelt

Department of Physical Chemistry, Institute of Chemistry, Eötvös Loránd University, Pázmány Péter sétány 1/A, 1117 Budapest, Hungary

E-mail: inzeltgy@chem.elte.hu

Received: September 29, 2017; Revised: October 30, 2017; Accepted: November 2, 2017

Abstract

In my plenary lecture delivered at the 6th Regional Symposium on Electrochemistry of South-East Europe (RSE-SEE) that was held between June 11 and 15, 2017, in Balatonkenese, Hungary I surveyed the developments in the field of conducting polymers based on my 40 years of experience in this area. It is intended to give an overview including thermodynamical considerations, redox transformations and transport processes, methods of investigation, redox polymers, electropolymerization, characterization, and applications with abundant examples from my research results.

Keywords

Synthesis; Redox behaviour; Composites; Sensors; Biosensors; Supercapacitors; Electrocatalysis

Introduction

The preparation, characterization and application of electrochemically active, electronically conducting polymeric systems are still at the foreground of research activity in electrochemistry [1-3]. There are at least two major reasons for this intense interest. First is the intellectual curiosity [1-4] of scientists, which focuses on understanding the behavior of these systems, in particular on the mechanism of charge transfer and on charge transport processes that occur during redox reactions of conducting polymeric materials [2, 4-6]. Second is the wide range of promising applications of these compounds in the fields of energy storage, electrocatalysis, organic electrochemistry, bioelectrochemistry, photoelectrochemistry, electroanalysis, sensors, electrochromic displays, microsystem technologies, electronic devices, microwave screening and corrosion protection [2]. After 40 years of research in the field, the fundamental nature of charge propagation is now in general understood; *i.e.*, the transport of electrons can be assumed to occur via an electron exchange reaction (electron hopping) between neighboring redox sites in redox polymers, and by the movement of delocalized electrons through conjugated systems in the case of so-called intrinsically conducting polymers (*e.g.*, polyaniline, polypyrrole). (In fact, several conduction

mechanisms, such as variable-range electron hopping and fluctuation-induced tunneling, have been considered.) In almost every case, the charge is also carried by the movement of electroinactive ions during electrolysis; in other words, these materials constitute mixed conductors [2,5,6]. Owing to the diversity and complexity of these systems — just consider the chemical changes (dimerization, cross-linking, ion-pair formation, *etc.*) and polymeric properties (chain and segmental motions, changes in the morphology, slow relaxation) associated with them, the discovery of each new system brings new problems to solve, and much more research is still needed to achieve a detailed understanding of all of the processes related to the dynamic and static properties of various interacting molecules confined in a polymer network.

Although the conductivity of these polymers is an interesting and a utilizable property in itself, their most important feature is the *variability of their conductivity*, *i.e.*, the ease with which the materials can be reversibly switched between their insulating and conducting forms (Figure 1). (The conductivity of copper is still better but not variable!)

An evidence of the existence of the mobile electrons in the system is the practically uniform absorbance at high wavelengths in half-oxidized state (emeraldine form of polyaniline). It is characteristic to the metals (metallic conduction) since the excitation of the mobile electrons needs small and practically the same energy. At lower wavelenghts the variation of the spectra indicates the color change related to the leucoemeraldine – emeraldine – pernigraniline transitions (Figure 2).

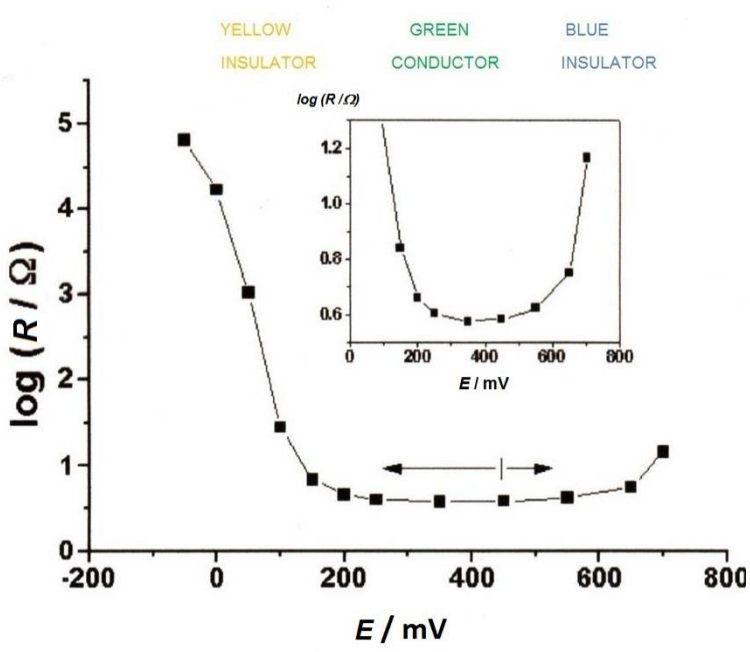

Figure 1. *Variation of the resistance of polyaniline as a function of potential (charging state) in contact with 1 mol dm^{-3} H_2SO_4 (compiled from the results of [7])*

We can utilize the variation of the conductivity in electronic devices including thin film transistors and insulated gate field effect transistors or in gas sensors; the color change in electrochromic display devices or in smart windows, the electroluminescence in light emitting devices, the swelling-deswelling accompanying the charging-discharging processes in artificial muscles, the charge storage capacity in energy technologies (batteries, supercapacitors). There are properties, which are useful in a certain application, *e.g.*, volume change, however, those may cause problem in other utilization. In fact, during the redox transformations generally we create a polyelectrolyte from an uncharged polymer, which alter many physical and chemical properties. For instance, the charged,

salt-form is insoluble, while the neutral form is soluble in certain organic solvents. The overcharging (overoxidation) may lead to the hydrolytic degradation of the polymer. In some cases the mechanical properties including adhesion is of importance, e. g., in corrosion protection or in membranes where gas evolution occurs, which are less crucial in batteries. In the early period several attempts were made to vary the morphology and the swelling properties by using different counterions. The derivatization of the monomers frequently lead to more flexible polymers.

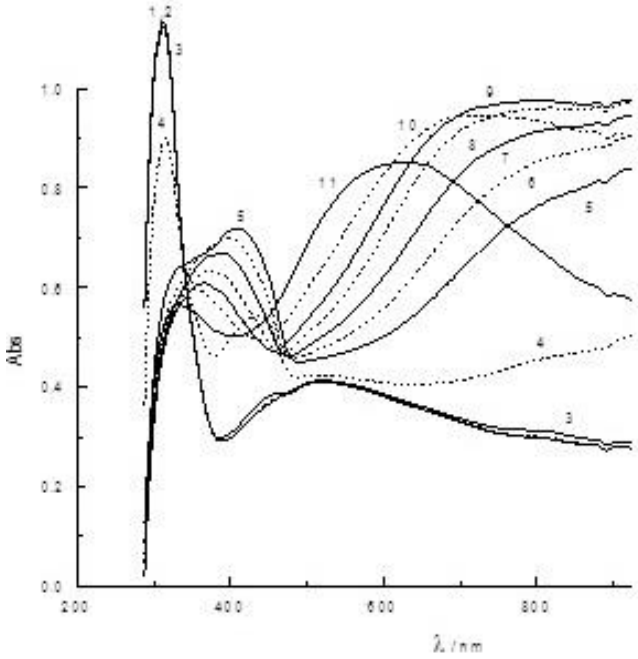

Figure 2. *UV–VIS–NIR spectra of PANI obtained in situ at different potentials: (1) −0.35, (2) −0.25, (3) −0.15, (4) −0.05, (5) 0.05, (6) 0.15, (7) 0.25, (8) 0.35, (9) 0.45, (10) 0.55, and (11) 0.65 V. Solution: 1 mol dm^{-3} H_2SO_4 [8]*

In the last decade the researchers have started to apply novel approaches. The new trend is the fabrication of composites including nanocomposites of polymers and other materials such as carbon nanotubes, graphene or inorganic compounds having special structure and properties. In sensors and biosensors of different kinds (conductometric, impedimetric, potentiometric, amperometric and voltammetric) conducting polymers are used as active, sensing or catalytic layers, however, in the the majority of application those serve as matrices entrapping enzymes or other biologically active compounds. The biocompatibility of several conducting polymers provides opportunity for the application in medicine as artificial muscles and limbs, as well as artificial nerves. The biomimetic (bionic) applications certainly will continue in the future. (References [1-6] contain hundreds of cited papers which were considered by the author as the most important ones. Therefore, most of the citations in this review are the author's works in connection with the results presented. It is worth to mention that the total number of papers on counducting polymers until 2017 according to the scientific database is ca. 300 000 [1].)

Historical background

Somewhat surprisingly, a new class of polymers possessing high electronic conductivity (electronically conducting polymers) in the partially oxidized state was discovered. Alan J. Heeger, Alan G. MacDiarmid and Hideki Shirakawa played a major role in this breakthrough, and they received the Nobel Prize in Chemistry in 2000 "for the discovery and development of electronically conductive polymers" [9-14]. The preparation of polyacetylene and the discovery of the large

increase in its conductivity after "doping" actually launched this new field of research. However, as Thomas Mann wrote: "Very deep is the well of the past". Our case is also curious because the most important representatives of these materials, polyaniline and polypyrrole, were already being prepared by chemical or electrochemical oxidation in the nineteenth century. Of course, for a long time they were not called polymers, since the existence of macromolecules was not accepted until the 1920s. Therefore, it is somewhat interesting to review the story of polyaniline here, because it provides an insight into the nature of the development of science. One may recall that aniline was prepared from the coal tar residues of the gas industry in the first half of the nineteenth century, and later played a fundamental role in the development of organic chemistry and the chemical industry. First, aniline dyes replaced dyes from natural sources. Then coal tar dyes found use in medicine (to stain tissues), and the selective toxicity of these compounds was also discovered. This initiated the chemical production of medicines, and the establishment of the pharmaceutical industry. In 1862 Dr. Henry Letheby, who was a physician and a member of the Board of Health in London, was interested in aniline because it was poisoning workers. Letheby observed that a bluish-green precipitate was formed at the anode during electrolysis, which became colorless when it was reduced and regained its blue color when it was oxidized again [15]. In 1840 Fritzsche observed the appearance of a blue color during the oxidation of aniline in acidic media [16]. In 1950 Khomutov and Gorbachev discovered the autocatalytic nature of the electrooxidation of aniline [17]. In 1962 Mohilner, Adams and Argersinger reinvestigated the mechanism of the electrooxidation of aniline in aqueous sulfuric acid solution at a platinum electrode. They proposed a free radical mechanism, and wrote that "the final product of this electrode reaction is primarily the octamer emeraldine, or a very similar compound" [18].

The first real breakthrough came in 1967, when Buvet delivered a lecture at the 18th Meeting of CITCE (later ISE), and this presentation appeared a year later in Electrochimica Acta [19]. Here we cite the first sentence of this paper, which speaks for itself: "Polyanilines are particularly representative materials in the field of organic protolytic polyconjugated macromolecular semiconductors, because of their constitution and chemical properties". They also established that polyanilines "also have redox properties," and that "the conductivity appears to be electronic". It was also shown that "polyanilines are also ion-exchangers". Finally, they proposed that "polyanilines... can be utilized for making accumulators with organic compounds". While Josefowicz et al. used chemically prepared PANI pellets as an electrode and for conductivity measurements, investigations of the mechanism of electrochemical oxidation also continued, and the name polyaniline became generally accepted. The paper of Diaz and Logan that appeared in 1980 [20] initiated research into polymer film electrodes based on polyaniline, which continues even today.

Definition and classification

Electrochemically active polymers can be classified into several categories based on the mode of charge propagation (note that insulating polymers are not considered here except for those with variable conductivity). The mode of charge propagation is linked to the chemical structure of the polymer. The two main categories are electron-conducting polymers and proton (ion)-conducting polymers. We will focus on electron-conducting polymers here.

We can also distinguish between two main classes of electron-conducting polymers based on the mode of electron transport: redox polymers and electronically (intrinsically) conducting polymers (ECPs or ICPs).

Redox polymers contain electrostatically and spatially localized redox sites which can be oxidized or reduced, and the electrons are transported by an electron exchange reaction (electron hopping) between neighboring redox sites if the segmental motions enable this. Redox polymers can be divided into several subclasses: i) polymers that contain covalently attached redox sites, either built into the chain, or as pendant groups; the redox centers are mostly organic or organometallic molecules; ii) ion-exchange polymeric systems (polyelectrolytes) where the redox active ions (mostly complex compounds) are held by electrostatic binding.

A simple distinction between the intrinsically conducting and redox polymers is that in dry state the ICPs are conducting while redox polymers are not. In the case of redox polymers water (or other solvent) acts as a plasticizer, and makes the chain and segmental motions possible which is inevitable to ensure the electron hopping between the localized redox groups.

Conducting polymers are mostly used as polymer film electrodes by electrochemists. A polymer film electrode can be defined as an electrochemical system in which at least three phases are contacted successively in such a way that between a first-order conductor (usually a metal) and a second-order conductor (usually an electrolyte solution) is an electrochemically active polymer layer which is usually a mixed conductor. The polymer layer is more or less stably attached to the metal, mainly by adsorption (adhesion).

Methods of investigation

Conducting polymers have been studied using the whole arsenal of methods available to chemists and physicists [2]. Electrochemical techniques, mostly transient methods such as cyclic voltammetry (CV), chronoamperometry (CA) and chronocoulometry (CC), are the primary tools used to follow the formation and deposition of polymers, as well as the kinetics of their charge transport processes. Electrochemical impedance spectroscopy (EIS) has become the most powerful technique used to obtain kinetic parameters such as the rate of charge transfer, diffusion coefficients (and their dependence on potential), the double layer capacity, the pseudocapacitance of the polymer film, and the resistance of the film [21].

The application of combinations of electrochemical methods with non-electrochemical techniques, especially spectroelectrochemistry (UV-VIS, FTIR, ESR), the electrochemical quartz crystal nanobalance (EQCN), radiotracer methods, probe beam deflection (PBD), various microscopies (STM, AFM, SECM), ellipsometry, and in situ conductivity measurements, has enhanced our understanding of the nature of charge transport and charge transfer processes, structure–property relationships, and the mechanisms of chemical transformations that occur during charging/discharging processes. In several cases to elucidate more complicated reaction mechanism it is necessary to apply the combination of more than one technique, *e.g.*, transient electrochemical technique with UV-VIS spectroelectrochemistry and ESR, or with spectroelectrochemistry and EQCN.

It is not necessary to deal with these techniques in detail here, since there are several books, monographs and papers on the subject [2, 21-24].

Preparation of conducting polymers

Both redox and electronically conducting polymers can be prepared using chemical and/or electrochemical methods of polymerization, although most redox polymers have been synthesized by chemical polymerization. Electrochemically active groups are either incorporated into the polymer structure inside the chain or included as a pendant group (prefunctionalized polymers),

added to the polymer phase during polymerization, or fixed into the polymer network in an additional step after the coating procedure (post-coating functionalization) in the case of polymer film electrodes. The latter approach is typical of ion-exchange polymers. The electrochemical polymerization is preferable, especially if the polymeric product is intended for use as a polymer film electrode, thin-layer sensor, in microtechnology, *etc.*, because potential control is a prerequisite for the production of good-quality material and the formation of the polymer film at the desired spot in order to serve as an anode during synthesis. A chemical route is recommended if large amounts of polymer are needed.

Electropolymerization

In the majority of cases the polymers are prepared by electrooxidation of the respective monomer compound. The oxidation of the monomer results in the formation of a cation radical. The chain propagation occurs via dimerization of the radicals formed and elimination of hydrogen ions. The dimer is oxidized (more easily than the monomer) and a next coupling step takes place with a monomeric cation radical. The radical cation—radical cation coupling (RR coupling) –due to the strong Coulombic repulsion– is considered less likely than the radical cation—substrate coupling (RS coupling), *i.e.*, the coupling of a charged and a neutral species. However, in condensed phase RR coupling can proceed in a substantial rate. The nature of the rate-determining step (rds) depends on the conditions; since the rate of the deprotonation, the solubility of the oligomer, the stability of the cation radical depend on the nature of the solvent (*e.g.*, its effect on the proton elimination), electrolyte (especially on the nature of the anion which may stabilize the cation), and temperature [2, 25, 26]. One has to consider also the deposition step which strongly depends on the nature of the substrate (metal, carbon *etc.*). Some metals can catalyze the oxidation of the monomer or a first layer of monomers may be formed due to the chemisorption on the metal which is characteristic in several monomers on Pt or PtO [27].

During the very first potential cycle a characteristic loop (a crossing pattern that appears in the cyclic voltammogram on reverse scan) (Fig. 3) can be observed which is due to the energy needed for the nucleation. According to another view in some cases the loop is due to a homogeneous comproportionation reaction [25] which facilitates the oxidation of the monomer.

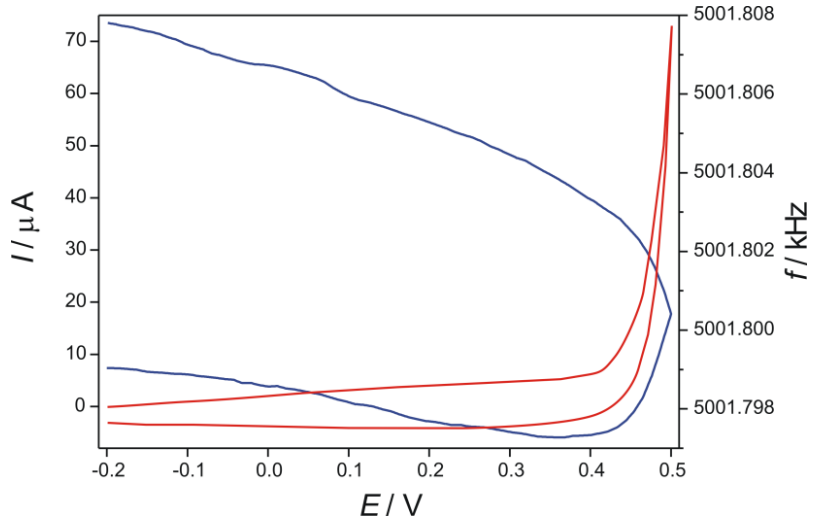

Figure 3. *The 1st cyclic voltammogram (–) and the simultaneously detected EQCN response (–) during the electrooxidation of 6-aminoindole (1.5 × 10^{-2} mol dm^{-3}) on Au in 1 mol dm^{-3} H_2SO_4 solution. Scan rate: 25 mV s^{-1}, switching potential: 0.5 V [27].*

A huge anodic current appears and simultaneously the EQCN resonant frequency starts to decrease which continues until anodic current flows. This indicates a deposition of the oxidation product on the gold surface. The –5 Hz frequency decrease corresponds to a ca. 0.7 nm thin film, assuming 1.2 g cm^{-3} for the density of the film or a surface concentration of 6-aminoindole, Γ = 6.7 $\times$ 10^{-10} mol cm^{-2}. It follows that barely a monolayer or even submonolayer film was formed, *i.e.*, it can be considered just a nucleation. While the nucleation process is somewhat hindered, the growth of the film is a much faster process. In Fig. 3 the so-called nucleation loop, *i.e.*, the crossing pattern of the anodic current and the current after switching is not well seen, because the switching potential was limited to 0.5 V in order to avoid the overoxidation. However, it exists, and well-seen when a higher positive switching potential was applied during the first scan. It has been interpreted as the start of the nucleation process.

The progress of the electropolymerization and the deposition of the polymers can be nicely seen on the cyclic voltammograms since the peak currents (and the charge under the waves) related to the redox responses of the conducting polymer increases. By using electrochemical quartz crystal nanobalance the increase of the deposited mass can be monitored directly. It can be seen in the following figures (Fig. 4 polyaniline, Figs. 5-7 polyindole and poly(4-aminoindole, respectively).

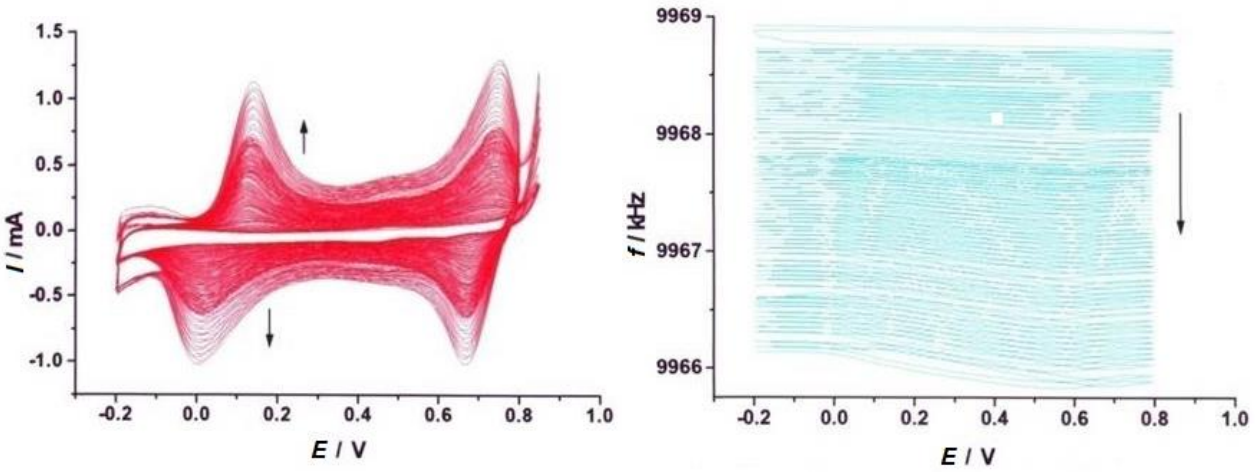

Figure 4. *The cyclic voltammograms and the simultaneously detected EQCN frequency changes during the electropolymerization of aniline at a platinum electrode. Scan rate: 100 mV* s^{-1}*. Solution composition: 0.2 mol* dm^{-3} *aniline in 1 mol* dm^{-3} $HClO_4$ *[28].*

The mechanism of polyaniline formation is influenced by the deposition of oligomers, and the highest growth rate in cyclic electropolymerization occurs during the cathodic potential scan. The film morphology (compactness, swelling) is strongly dependent on the composition of the solution, notably on the type of counter-ions present in the solution, and the plasticizing ability of the solvent molecules. Due to the autocatalytic nature of the electropolymerization, the positive potential limit of cycling can be decreased after 2–10 cycles, which is a common practice used to avoid the degradation of the polymer due to the hydrolysis of the oxidized polyaniline (pernigraniline form). The head-to-tail coupling that results in the formation of *p*-aminodiphenylamine, tail-to-tail dimerization (benzidine) also occurs; however, the latter is considered to be a minor dimer intermediate because the rate constant of dimerization for RR coupling that produces the former product is about 2.5 times higher than that for the tail-to-tail dimer. Two types of nucleation (instantaneous and progressive) and three types of growth (1-, 2-, and 3-dimensional) have been observed in the case of different polymers and conditions. Although the region close to the electrode surface exhibits a more or less well-defined and compact structure, in general the polymer

layer can be considered to be an amorphous material with decreasing density as a function of the distance of the substrate.

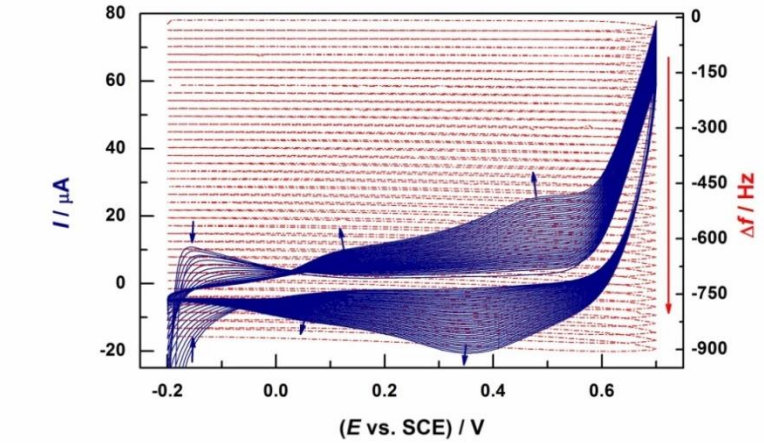

***Figure 5**. Cyclic voltammograms and the simultaneous change of the EQCN frequency (Δf) during the oxidative electropolymerization of indole (1 mmol dm^{-3}) in 1 mol dm^{-3} $HClO_4$ on Pt during 40 consecutive cycles. Scan rate: 10 mV s^{-1} [29]*

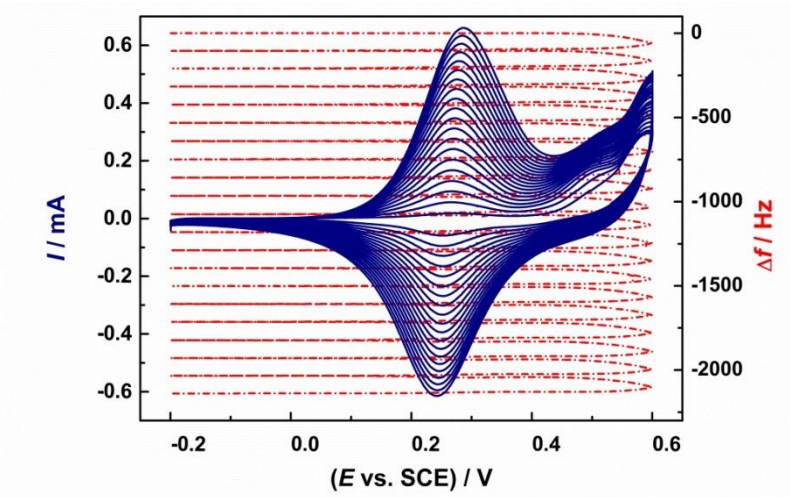

***Figure 6.** Cyclic voltammograms and the simultaneous change of the frequency (Δf) during the electropolymerization of 4-aminoindole (1 mmol dm^{-3}) in 1 mol dm^{-3} $HClO_4$ on Pt, during 20 consecutive cycles. Scan rate: 10 mV s^{-1} [29]*

While the usual representation, *i.e.*, the decrease of the EQCN frequency (or the increase of the surface mass) during consecutive voltammetric cycles can be found in the majority of papers (Figs. 5 and 6), displaying the variation of the EQCN frequency as a function of time can be more instructive. In this case the changes in the course of each cycle are much better seen (Figs. 7). It is well seen that while the surface mass increases from cycle to cycle (continuous decrease of the frequency at the beginning of the subsequent cycles), there is a change during each cycle. In the case of indole this change is getting higher and higher (Fig. 7a) since during the oxidation and reduction counter-ions enter and leave the surface film, respectively, and as the film is getting thicker more and more counter-ions (in this case anions) enter or leave the film in the charge-compensating process. In the case of 4-aminoindole the Δ*f vs.* time curve resembles a staircase (Fig. 7b). This dependence reflects that the deposition occurs with the same rate from cycle to cycle and the frequency variation is independent of the film thickness. It is only possible if there is no movement of ions of considerable mass, *i.e.*, the transport of H^+ ions should be considered instead of anions.

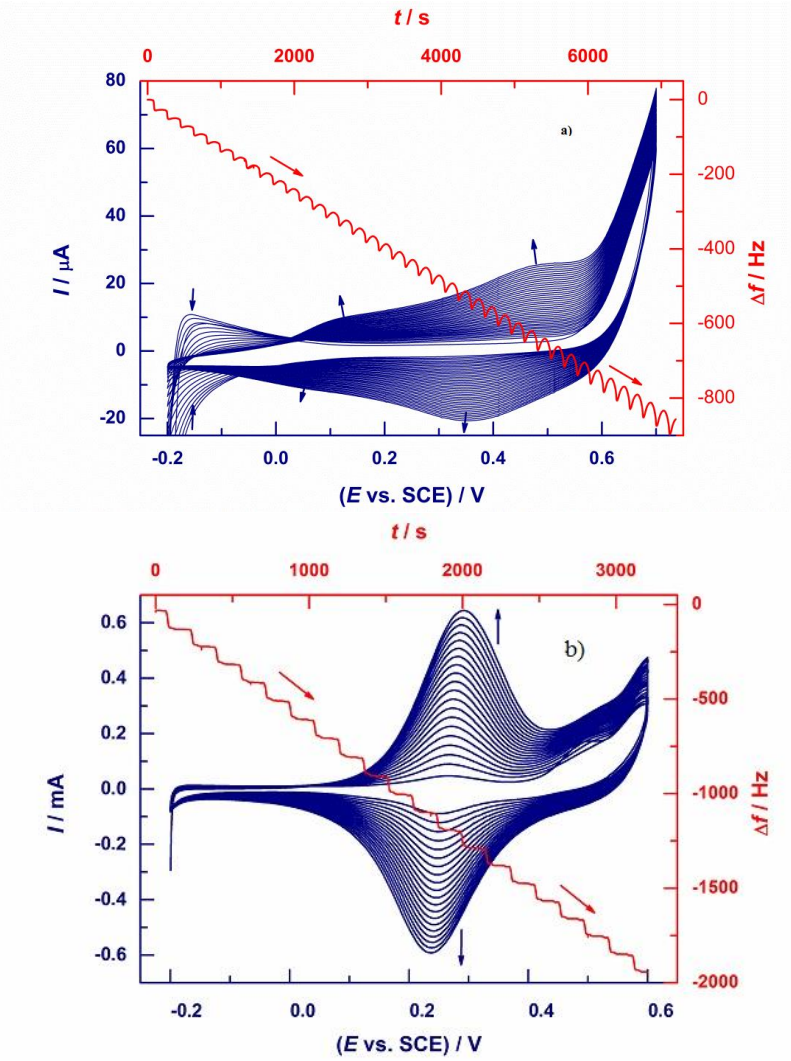

Figure 7. *Comparison of the electropolymerization of indole (a) and 4-aminoindole (b) under the same circumstances on the same type of electrode (1.37 cm^2 Pt) in 40 and 20 cycles, respectively. Cyclic voltammograms and the simultaneously detected frequency curves. The frequency curves are plotted as function of the time. $c_{monomer}$ = 1 mmol dm^{-3}, electrolyte: 1 mol dm^{-3} $HClO_4$. Scan rate: 10 mV s^{-1} [30].*

While electrochemical impedance spectroscopy has become a basic tool in the study of the rate of charge transport processes, film resistances and capacitances of polymer film electrodes, it is relatively seldom used to follow the electropolymerization process. Figures 8 and 9 show such results and the respective electrical equivalent circuit [30].

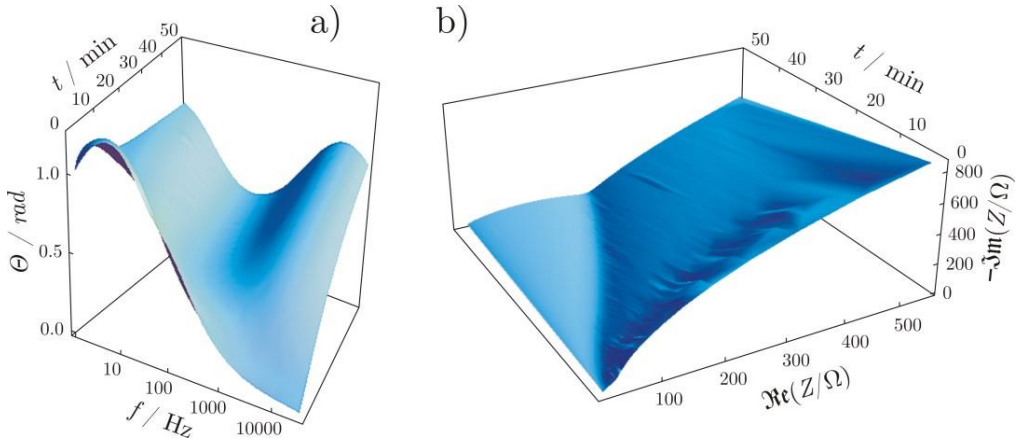

Figure 8. *Three-dimensional representation of the (a) Bode and (b) Nyquist plots of the measured impedance data during the electrodeposition of polyindole on Pt at 0.7 V in 0.1 mol dm^{-3} H_2SO_4 solution [31]*

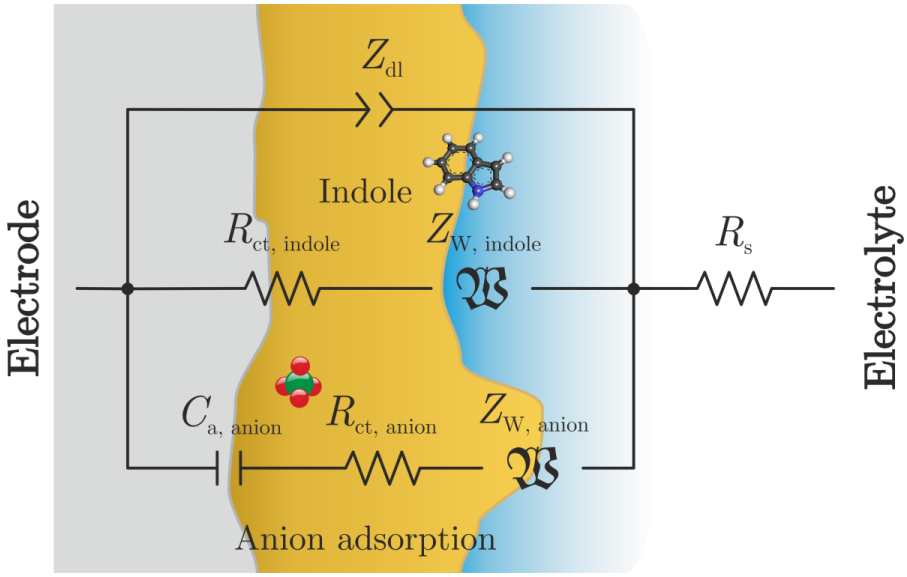

Figure 9. *Electrical equivalent circuit describing the EIS response of polyindole deposition on platinum. Z_{dl} represents the impedance of the double layer, $R_{ct,indole}$ and $Z_{W,indole}$ are the charge transfer and diffusional impedances of indole, respectively, $C_{a,anion}$ is the capacitive impedance related to the counter-ion adsorption (on Pt surface), $R_{ct,anion}$ is the charge transfer resistance associated with the counter-ion adsorption/desorption, $Z_{W,anion}$ is the diffusional impedance of the counter-ions, and R_s is the solution resistance. The equivalent electric circuit has been elucidated based on a priori chemical knowledge about this system [31].*

Following the variation of the characteristic parameters several conclusions could be drawn concerning the events at the surface (adsorption of indole and ions, polymerization *etc.*). The charge transfer resistance and Warburg coefficient associated with indole itself vary with time, providing evidence that after an inductive period, the process of generation of active centers is at its maximum contributing to noticeable diffusion limitations. The apparent rate coefficient reflects the relative contribution of slow and fast electrochemical stages involving the interfacial charge transfer during the film growth. In general, formation of nuclei of a new phase is considerably slower than their growth. At higher times the surface of Pt is covered by the polymer film, so that the growth at the Pt/polyindole boundary is suppressed. However, the diffusion coefficient of the indole molecules in/at the relatively thick indole film is decreased. The sulfate adsorption capacitance significantly changes during the polymer film growth. At the anodic potential selected for polymerization, it is known that the sulfate surface coverage is ~0.2 monolayer (ML) in H_2SO_4, and the adsorption capacitance is approximately a few μF cm^{-2} as the adsorbate layer is almost "saturated". After 5 min of indole electropolymerization, the adsorption capacitance increases up to ~200 μF cm^{-2}. This value roughly corresponds to 0.1 ML of sulfates adsorbing and desorbing during the low-amplitude ac probing, *i.e.* ~50 % of the available adsorbed sulfates are "disturbed" during initial stages of polymerization. However, after ~10 min, the adsorption capacitance decreases (~100 μF cm^{-2}) and remains approximately constant. The non-zero values of the adsorption capacitance after ~10 min indirectly suggest that redox transformations at the polymer/Pt interface still significantly disturb the adsorbed sulfate layer.

Overoxidation

The overoxidation is a general problem in the course of the electropolymerization and also the investigation or the use of conducting polymer modified electrodes. The choice of positive potential limit in the case of electropolymerization or the application of proper oxidant (redox couple which does not possess too positive equilibrium potential) in the case of chemical oxidation is essential to

have a good quality polymer. At high anodic potentials the further oxidation of the polymer occurs, and this oxidation product undergoes a chemical reaction, *e.g.*, in the case of polyaniline quinone groups appear due to hydrolysis reaction. It manifests itself in the so-called "middle peak" between the two main voltammetric peaks (see Fig. 10).

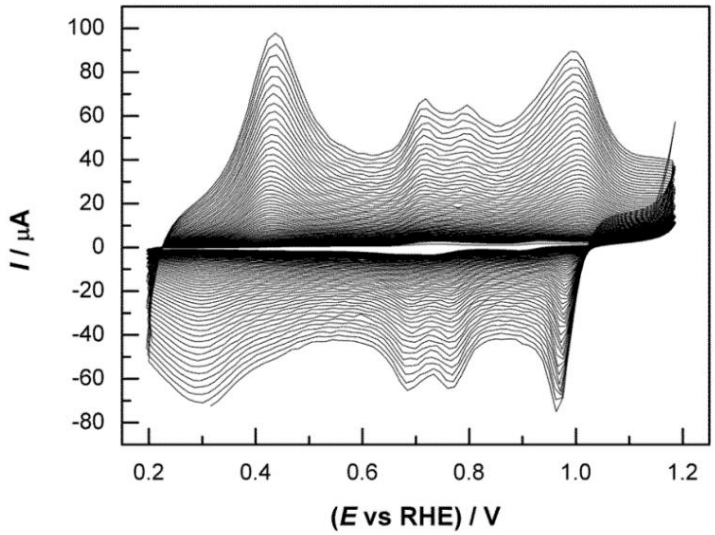

Figure 10. *The consecutive cyclic voltammograms during the electropolymerization of aniline at a platinum electrode. Scan rate: 100 mV s^{-1}. Solution composition: 0.2 mol dm^{-3} aniline in 0.5 mol dm^{-3} H_2SO_4*

In the case of the electropolymerization of 4-aminoindole it can be seen that during the consecutive cyclic voltammograms (2-6th and 7-9th) the current continuously decreases during the cycling together with a shift of the peak potential. The rate of the frequency change shows also decreasing characteristics from cycle to cycle (Fig. 11). By using positive potential limits above 0.6 V an overoxidation and hydrolysis occur and the electroactivity and conductivity of the film become negligible. Nevertheless, a bluish-purple layer, which was formed, remained on the surface. Similar phenomenon can be observed practically for all indole derivatives as shown in Figures 12-14 in the case of 6-aminoindole.

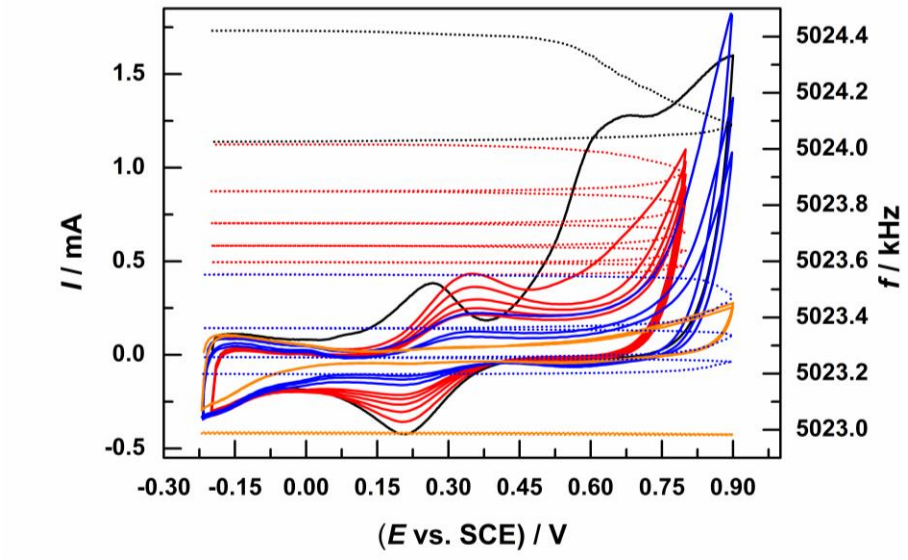

Figure 11*. Effects of the extended positive potential limit. The figure shows the first cycle (black), from the 2nd to the 9th cycle (red), and the 19th and 20th cycles (yellow) from a series of measurements. Solution: 1 mmol·dm^3 4-aminoindole in 0.5 mol·dm^3 H_2SO_4. Pt electrode, v = 20 mV·s^1 [29].*

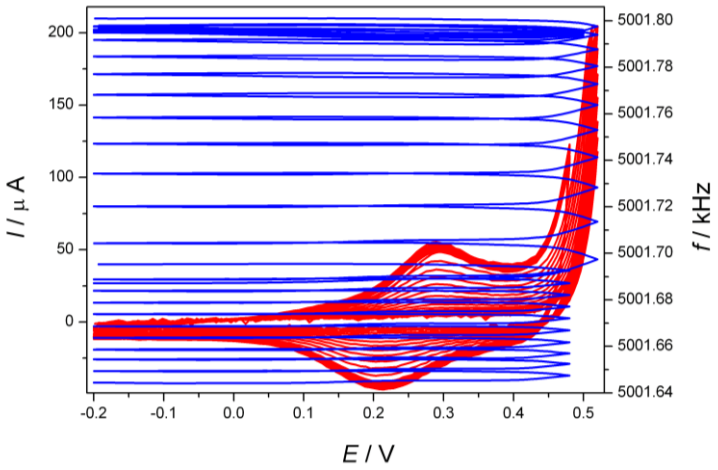

Figure 12. *Subsequent cyclic voltammograms and the simultaneously detected EQCN responses during the electrooxidation of 6-aminoindole (1.5 × 10^{-2} mol dm^{-3}) on Au in 1 mol dm^{-3} H_2SO_4 solution. Scan rate: 25 mV s^{-1}. After the 17th cycle the switching potential was decreased to 0.48 V [27]*

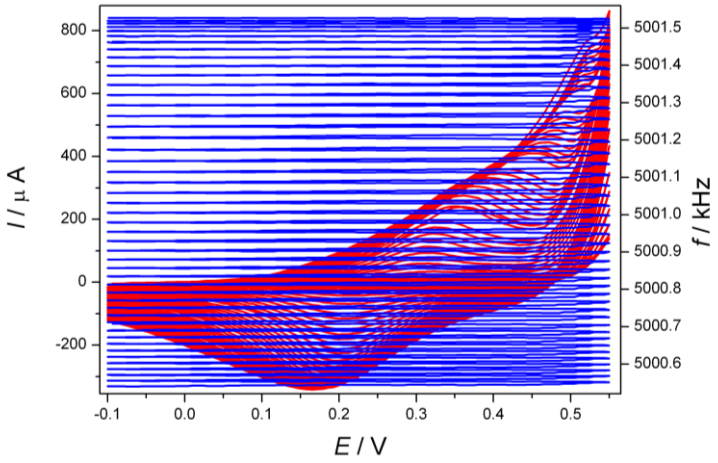

Figure 13. *Subsequent cyclic voltammograms and the simultaneously detected EQCN responses during the electrooxidation of 6-aminoindole (1.5 × 10^{-2} mol dm^{-3}) on Au in 1 mol dm^{-3} H_2SO_4 solution. Scan rate: 50 mV s^{-1}. The first 46 cycles between –0.1 V and 0.55 V without changing the switching potential [27].*

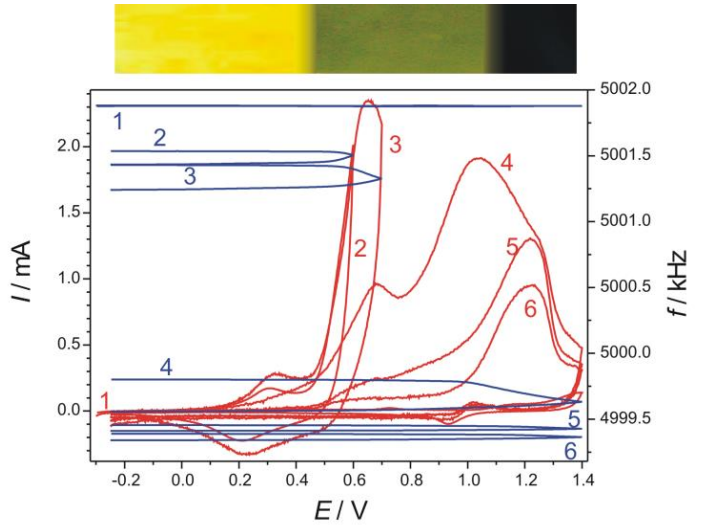

Figure 14. *Cyclic voltammograms and the simultaneously detected EQCN responses during the electro-oxidation of 6-aminoindole film on Au in contact with 1 mol dm^{-3} H_2SO_4. The change of the color of the film by using the original photos of the electrode is also displayed. The positive potential limit was increased during the consecutive cycling. The responses of the clean gold electrode in the potential range between –0.3 V and 1.40 V (1). Positive potential limits were as follows: 0.55 V (2), 0.65 V (3), and 1.4 V (4-6) (three subsequent cycles) [27].*

The oxidation peak of the polymer, appearing at 0.27 V in the course of the first cycles when 0.5 V potential limit was kept, gradually shifts into the direction of more positive potentials. Its height shows decreasing tendency with cycling to higher positive switching potentials (curves 2-4 of Fig. 14). The oxidation peak of the monomer appears at 0.6 V, the frequency decrease related to the deposition of the polymer gradually increases (curves 2 and 3 of Fig. 14). During continuous cycling using higher and higher positive potential limits the deposited mass increases. However, the peak height and the charge consumed during the oxidation of the monomer (together with the oxidation of the film) decreases, and eventually both the charge and the frequency observed earlier by applying a given switching potential gradually diminishes (for the sake of clarity not all cycles are shown in Fig. 14). When 1.4 V switching potential was applied (curves 4-6) the effect described above is well seen. Finally, during cycling 7 Hz frequency variation can be observed, which is approximately equal to the magnitude of the usual double layer charging, *i.e.*, no further deposition takes place, and the film redox activity also diminishes. Nevertheless, a bluish-purple layer, which was formed, remained in the surface. Because of the loss of electrochemical activity it can be concluded that the conjugated polymer bonds break down, and an indigo or indirubin-like insoluble but colored layer is formed.

Thermodynamical considerations

Thermodynamical considerations (the question of equilibria)

No equilibrium (adsorption equilibrium) exists between the surface phase and the solution with respect to the polymer. In most cases no chemical bonds exist between the substrate and the polymer, the polymer layer remains at the surface due to the van der Waals forces between the substrate and the polymer, as well as between the polymer chains in multilayer films. The adsorption model of de Gennes predicts a diminishing layer density which has been observed, indeed, *i.e.*, the polymer film is more compact close to the substrate surface.

Equilibrium situation is seldom established within the time scale of the experiments since the relaxation process of the polymer network (gel) may be extremely long. It is true not only with respect to the polymer morphology (conformation) but also to the membrane equilibria with participation of ions and solvent molecules. In the first approach the surface polymer layer can be treated as an amorphous swollen gel with a uniform structure and density in contact with a solution containing solvent molecules and ions. In this case, both non-osmotic and osmotic membrane equilibria, as well as the mechanical work done in swelling the polymer, must be taken into account. In most cases the situation is even more complicated than that usually treated using membrane equilibrium, since the charge in the polymer changes during the redox reaction; in most cases a neutral polymer is transformed into a polyelectrolyte, and vice versa.

Membrane equilibria

Even in the case of a neutral polymer one should consider the partitioning equilibria of the solvent molecules, the neutral salt and the ions formed by dissociation. The solvent content in the polymer phase obviously depends on the difference between the standard chemical potentials of the solvent molecules in the two contacting phases. Ions enter the film if their van der Waals and ion-dipole interactions with the polymer are large. Ions can be solvated (hydrated) by both the polymer and the solvent. When the polymer is hydrophobic and the solvent is hydrophilic the interaction energies between the polymer segments and between the solvent molecules are higher than those between the polymer segments and the solvent molecules. In this case, the polymer

segments are not solvated by the solvent molecules, and hence there is no solvent swelling of the polymer film. If the neutral polymer contains polar groups, water molecules will enter the polymer and the polymer phase will eventually contain substantial amounts of water.

The situation is different when the interface is not permeable for one of the ions; *i.e.*, the polymer film behaves like an ion-exchange membrane. This is the case when the polymer is charged, which is usually achieved by oxidation or reduction; however, this can also be the result of protonation. Two cases should be considered: (i) non-osmotic membrane equilibrium; (ii) osmotic membrane equilibrium. In the latter case, where solvent molecules can enter the surface layer or the membrane, the situation is more complicated since mechanical equilibria are also involved. The non-osmotic membrane equilibrium is illustrated in Fig. 15.

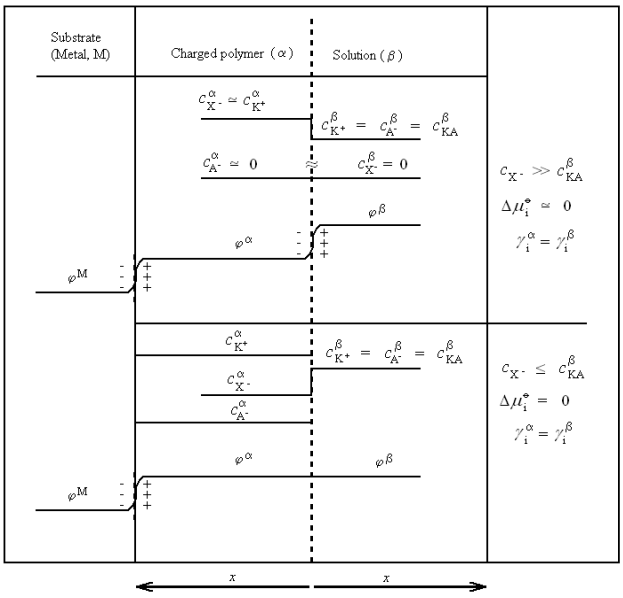

Figure 15*. Charged polymer in contact with an electrolyte solution. Non-osmotic membrane equilibrium [2]*

In the case of osmotic membrane equilibrium incorporation of ions and solvent molecules into the polymer phase, a swelling of the polymer layer occurs, *i.e.*, the state of the polymer phase depends on the potential. For the thermodynamical description of the expansion or contraction of the polymer network a mechanical work term has to be considered. The deformation of the polymer layer: plastic (break-in period) or elastic (reversibly coupled to the redox reaction).

Redox transformations and the accompanying processes

The electron transfer taking place at the metal|polymer interface is accompanied by ionic charge transfer at the polymer|solution interface, in order to maintain the electroneutrality within the polymer phase. Counter-ions usually enter the polymer phase. However, less frequently the electroneutrality is established by the movement of co-ions present in the polymer phase, *e.g.*, in so-called "self-doped" polymers. Oxidation reactions are often accompanied by deprotonation reactions, and H^+ ions leave the film, removing the excess positive charge from the surface layer. It should also be mentioned that simultaneous electron and ion transfer is also typical of electrochemical insertion reactions; however, this case is somewhat different since the ions do not have lattice places in the conducting polymers, and both cations and anions may be present in the polymer phase without any electrode reaction occurring. A general scheme of the charge transport and the accompanying processes is shown in Fig. 16.

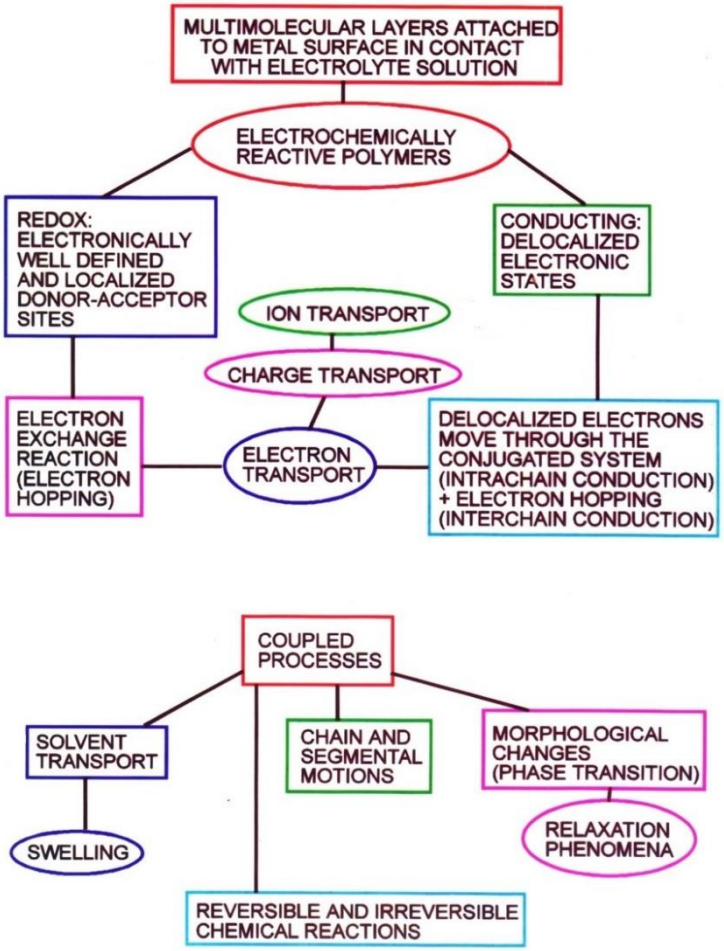

Figure 16*. The charge transport and the accompanying processes in the case of a polymer film electrode*

Owing to the complexity of the system and its redox transformations to gain a deeper understanding of the mechanism combined techniques should be applied. In many cases even the combination of more techniques is necessary. Two examples will be presented below. The considerable difference between the anodic and cathodic peak potentials of the cyclic voltammograms for the poly(tetracyanoquinodimethane) (TCNQ) redox electrode has been explained by the formation of dimeric species; *i.e.*, the slow formation of mixed-valence dimers during reduction (charging) and the fast re-oxidation of dimer dianions resulting in mixed-valence dimers during the discharging process [31]. The concentrations of the anion radicals and the dimer dianions were derived from UV-VIS spectroelectrochemical data. The concentration of the mixed-valence dimer was calculated from the variation in the ESR intensity and the concentration of the other paramagnetic species, $TCNQ^{\cdot-}$ and $TCNQ^{\cdot-}_2$ (Fig. 17). It is striking evidence that even UV-VIS spectroelectrochemistry is not enough to reveal all the intermediate products since the mixed-valence dimer, $TCNQ^{\cdot-}_2$ is silent within the available spectral lengths.

In order to monitor the transport and equilibria of ions and solvent molecules the electrochemical quartz crystal nanobalance (EQCN) and radiotracer techniques are relatively simple but highly effective methods. A comparison of the behavior of polyindole and poly(4-aminoindole) serves as an illustration (Figures 18 and 19).

The reduction peak belonging to the first oxidation peak is rather undeveloped and suppressed by the second one. The frequency change follows the charging–discharging processes. The apparent molar mass, that corresponds to the $\Delta f/Q$ quotient is 90.6 g mol^{-1} (n = 1). Therefore, ClO_4^--anions enter and leave the film during its oxidation and reduction, respectively.

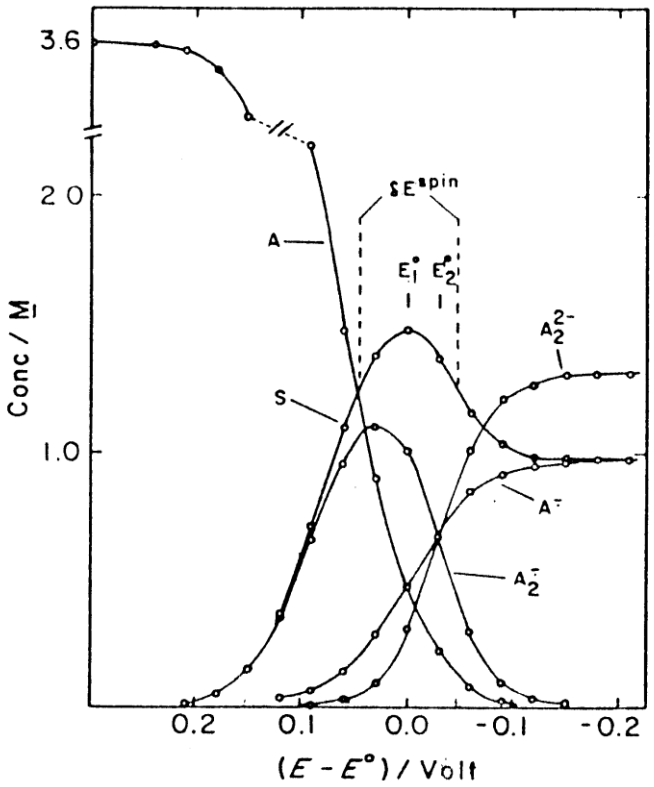

***Figure 17**. Distribution diagram for the species formed during the electroreduction of poly(tetracyanoquinodimethane). A = TCNQ, A^- = $TCNQ^-$, A_2^- =$TVNQ_2^-$, A_2^{2-}=$TCNQ_2^{2-}$, and S = c_{TNCQ^-} + $c_{TNCQ_2^-}$ [32]*

In the case of poly(4-aminoindole) based on the frequency change vs. potential curve three processes can be distinguished in both scan directions (Fig. 19).

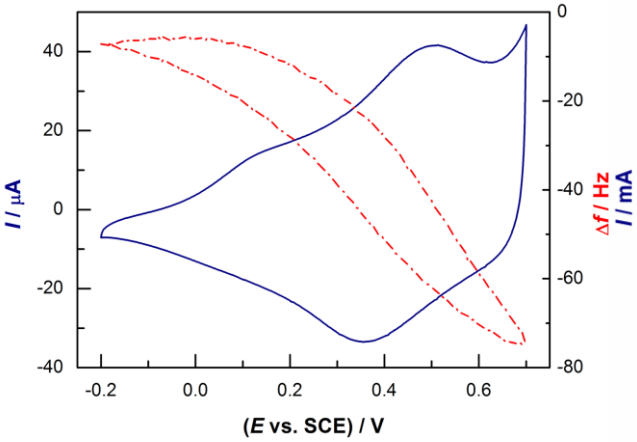

***Figure 18.** Cyclic voltammogram with the frequency change curve of a polyindole film in 1 mol dm^{-3} $HClO_4$. Scan rate: 10 mV s^{-1} [29]*

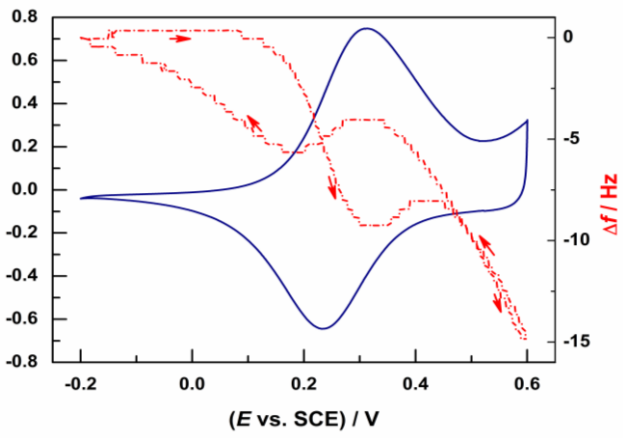

***Figure 19**. Cyclic voltammograms and the corresponding frequency curves of a poly(4-aminoindole) layer on Au, measured in (1 mol dm^{-3} $HClO_4$) at 10 mV s^{-1} [29]*

In the positive scan direction, from 0.1 V an increasing current can be detected. Simultaneously a mass increase starts, which is attributable to anion incorporation. However, the apparent molar mass value (M = 10 g mol^{-1}) that can be calculated from the mass vs. charge function is much lower than the molar mass of the perchlorate ions. While the frequency decrease during the ascending part of the cyclic voltammetry wave is evident, its value is rather small especially compared to the relatively substantial charge consumed. This observation can be elucidated by assuming simultaneous anion sorption and deprotonation, and the latter process is the dominant one. Together with

protons water molecules also leave the film, *i.e.*, desorption of hydrated H_3O^+ can be considered. From 0.3 V, a strange frequency increase-decrease pattern can be detected before the next frequency decrease section. This type of changes has been detected in the cases of other systems, and has been assigned to a structural rearrangement which occurs simultaneously with a partial deprotonation and dehydration of polymer layer. Further charging results in anion incorporation and deprotonation again. The EQCN technique can resolve the events occurring under the wide voltammetric wave, and these results reveal that the charge compensating processes are more complicated than that are usually expected. Therefore, at least three consecutive processes can be considered despite the single pair of peaks that appears in the current response.

A direct way to monitor the ion exchange processes can be achieved by radiotracer technique. Using the radiotracer method, the strength of the ion–polymer interactions can also be studied, which is certainly a special advantage of this technique. When unlabeled species are added to the solution phase in great excess, the sorbed species are exchanged provided that there are no strong interactions (chemical bonds) between the ions or molecules and the polymer. At a given potential the mobility of the ions can be tested (Fig. 20).

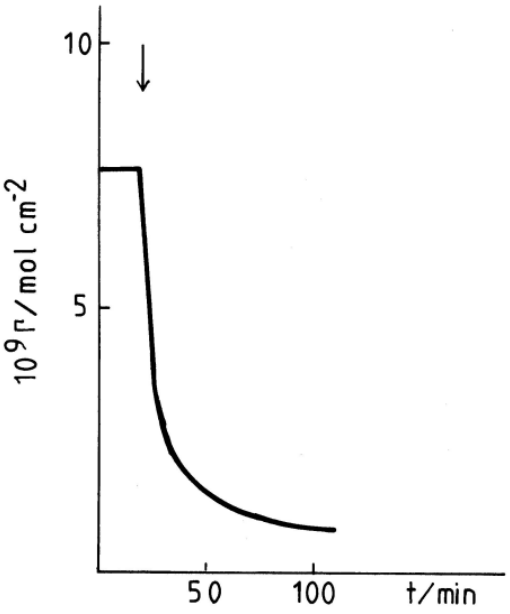

Figure 20*. The exchange of labeled SO_4^{2-} ions sorbed in polypyrrole film with unlabeled SO_4^{2-} ions added to a solution phase containing 10^{-5} mol dm^{-3} ^{35}S-labeled H_2SO_4 and 10^{-2} mol dm^{-3} $HClO_4$ at the moment indicated by the arrow. E = 0 V. Final H_2SO_4 concentration: 2×10^{-2} mol dm^{-3} [33]*

The results presented in Fig. 20 attest that ions embedded in polypyrrole (PP) film are mobile, despite the fact that the interactions between PP and SO_4^{2-} are much stronger than those between PP and ClO_4^- ions, since ClO_4^- ions are present at a concentration that is three orders of magnitude greater.

The periodical sorption/desorption of Cl^- ions during four consecutive potential cycles in the case of a polypyrrole electrode can be seen in Fig. 21. As expected Cl^- ions enter the PP film during oxidation and leave it during reduction.

A comparison of the data obtained by radiotracer and piezoelectric nanogravimetric techniques (EQCN) is especially useful, because the latter supplies information on the total surface mass change due to the deposition or sorption of different species, while the contributions originating from the different species can be unambiguously separated by labeling the respective molecules or ions.

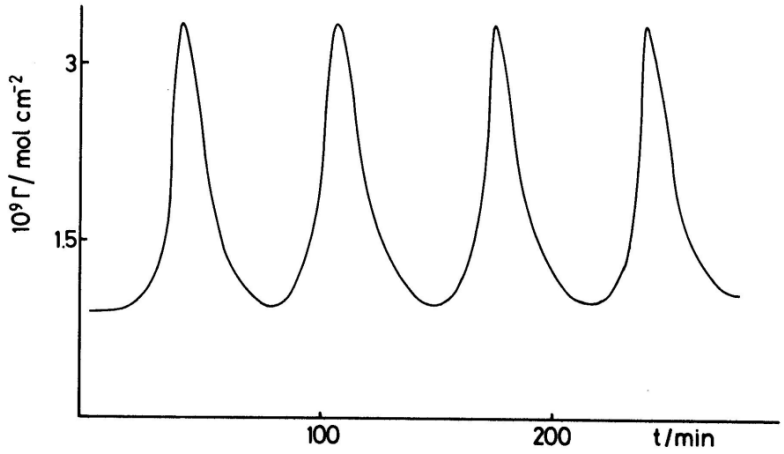

***Figure 21**. The change in the amount of Cl^- ions in a polypyrrole electrode during four consecutive oxidation--reduction cycles. Solution: 2×10^{-4} mol dm^{-3} ^{36}Cl-labeled HCl. Scan rate: 0.4 mV s^{-1}. [33]*

Recently, a new software controlled electrochemical measuring system for the simultaneous measurements of surface mass changes and optical absorbance spectra has been developed [34]**.** By using an EQCN, extremely useful quantitative information about electrode processes such as adsorption, deposition and dissolution, ion and solvent exchange between the surface film and the solution can be obtained. However, by using EQCN only the total mass change can be measured even in the case of ideal behavior. Therefore, one can draw reliable conclusion concerning the mechanism, if the nature of the intermediates and products of the electrochemical reactions will be determined by an independent technique. If the formed products or intermediates are colored species, spectroelectrochemistry is a plausible choice. The simultaneous use of the EQCN technique with spectroscopic UV-VIS measurements certainly helps to solve this problem (Fig. 22)**.**

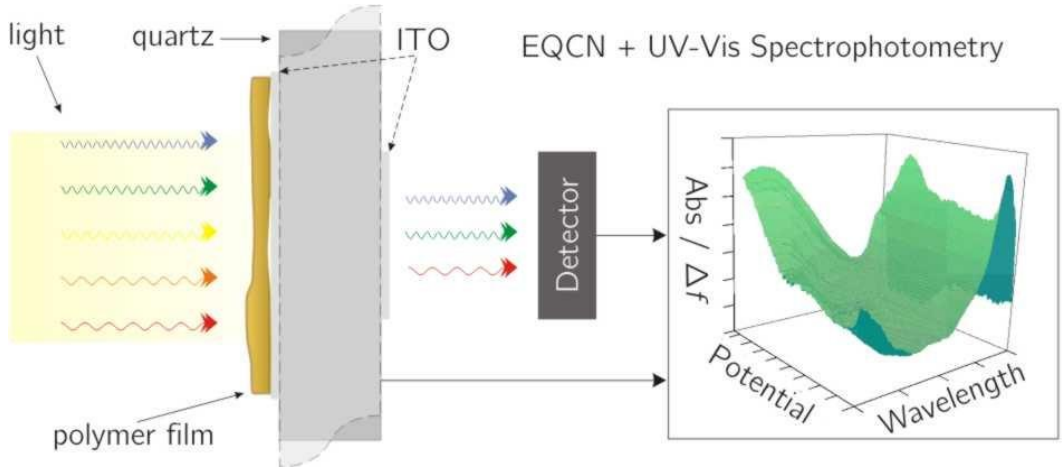

***Figure 22**. Absorbance of the polyaniline layer during a single anodic potential scan. Bare ITO crystal was taken as reference. Scan rate: 10 mV s^{-1}, electrolyte: 0.1 mol dm^{-3} H_2SO_4, $c_{aniline}$ = 0.01 mol dm^{-3} [34]*

Polymeric (polyelectrolyte) properties

Effect of temperature. Difference between redox and conducting polymers

The increase of temperature enhances the chain and segmental motions, therefore a more reversible, surface cyclic voltammetric behavior can be observed due to the more effective electron transport (Fig. 23). Of course, the rate of the counter-ion's motion also increases, however, in the case of redox polymers the polymeric motion and consequently the rate of the electron hopping is usually the rate-determining process.

In the case of intrinsically conducting polymers usually the intrachain electron transport is dominating, and consequently the temperature has no or a minor effect on the cyclic voltammograms (Fig. 24). Albeit in the case of polyaniline at higher pH values a strange effect can be observed, *i.e.*, shift of the voltammetric wave occurring at more positive potentials. It is related to the temperature dependence of the protonation constant of the weak base, therefore similar phenomenon appears with pH variation (Fig. 25).

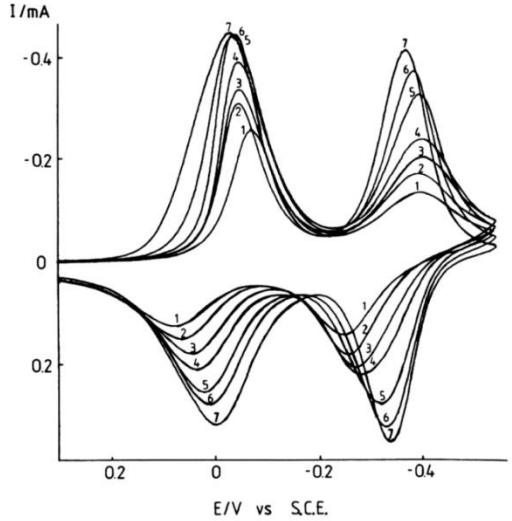

Figure 23*. Cyclic voltammograms of a poly(tetracyanoquinodimethane) (TCNQ) electrode (Γ= 5.1×10^{-8} mol cm^{-2}) in contact with aqueous 10 mol / dm^3 LiCl. Scan rate: 6 mV s^{-1}. Temperatures: (1) 22.5, (2) 34.2, (3) 43, (4) 50.5, (5) 61, and (6) 77 °C [35]*

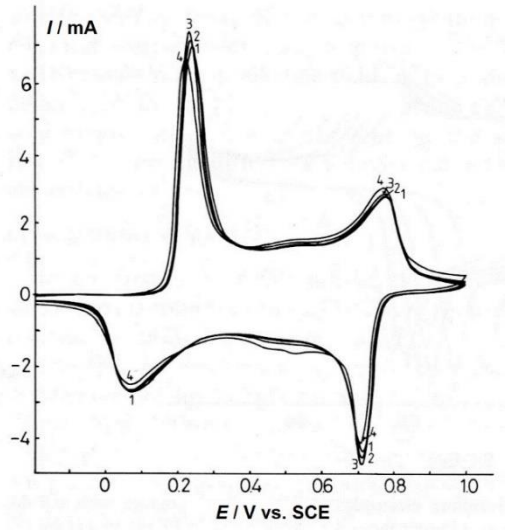

Figure 24. *Temperature dependence of cyclic voltammetric response of a polyaniline film at different temperatures. Temperatures: 1.5 (1), 4 (2), 13 (3) 29 °C (4); 1 mol dm^{-3} HCl pH = 0 v = 60 mV s-^{1} [36]*

The electrochemical responses and also the change of other properties, *e.g.*, color changes remain still fast at rather low temperatures. This is of practical importance because it allows using this system in electrochromic display devices at very low temperatures where the usual displays based on liquid crystals fail (Fig. 26).

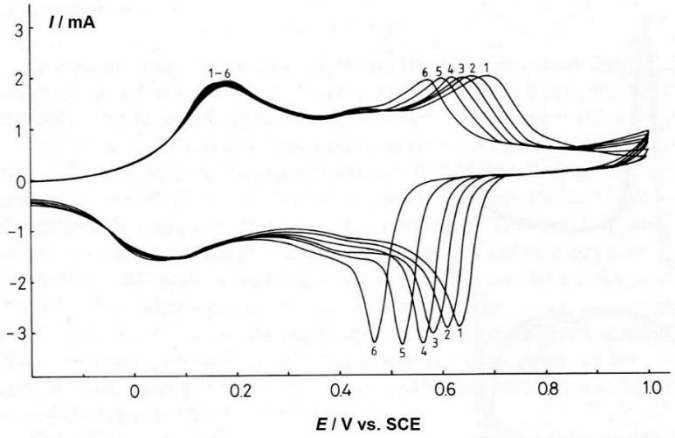

Figure 25. *Temperature dependence of cyclic voltammetric response of a polyaniline film at different temperatures. Temperatures: 19 (1), 29 (2), 36 (3), 46 (4), 58 (5), 66 °C (6); 0.9 mol dm^{-3} Na_2SO_4 mol dm^{-3} + 0.2 $NaHSO_4$ pH = 2.65 (lower part). v = 60 mV s^{-1} [36]*

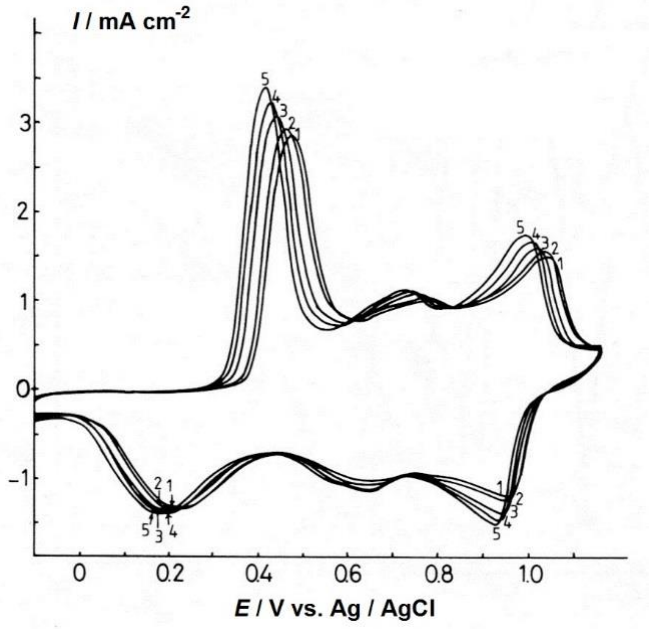

Figure 26. *Temperature dependence of cyclic voltammetric response of a polyaniline film in contact with moist acetonitrile containing 0.1 mol dm^{-3} H_2SO_4, 0.1 mol dm^{-3} tetrabutylammonium perchlorate and 0.01 mol dm^{-3} HCl (water content: 1.5 %) at different temperatures. Temperatures: –42 (1), –36.5 (2), –31 (3), –26.5 (4), and –21 °C (5). v = 25 mV s^{-1} [36]*

Effect of the electrolyte concentration

The swelling and shrinking of a polyelectrolyte gel are strongly affected by the concentration of the contacting electrolyte solution and the temperature. Thermodynamic theory, which considers three contributions to the free energy of the gel (*i.e.*, mixing of constituents, network deformation, and electrostatic interactions), predicts gel shrinkage as the salt concentration is increased. The shrinking process usually occurs smoothly, but under certain conditions the process becomes discontinuous, and the addition of a tiny amount of salt will lead to the collapse of the gel; *i.e.*, a drastic decrease in the volume to a fraction of its original value. These effects have strong influence on the cyclic voltammograms especially in the case of redox polymers (Figs. 27 and 28).

In a more compact structure the rate of electron hopping may increase since the concentration of redox sites is high; however, deterioration in the film's permeability to the counter-ions due to

the decrease in the free volume is expected at the same time. The maximum observed in the peak current versus salt concentration curve is the result of the balanced effects of the enhanced electron-exchange process and the hindered counter-ion motion. The abrupt change in the free volume of solvent-filled cavities causes a sharp decrease in the charge transport diffusion coefficient. A rigorous theoretical treatment which takes into account the extension and contraction of the polymer chain as it is electrochemically converted into a polyelectrolyte is very difficult if not impossible due to the complexity of the polyelectrolyte systems and the lack of an appropriate set of data. These effects were modeled in an empirical approach by scaling the concentration of electroactive sites in the polymer film and the effective charge transport diffusion coefficient (D_{ct}) with $c_s^{1/2}$ [4, 37].

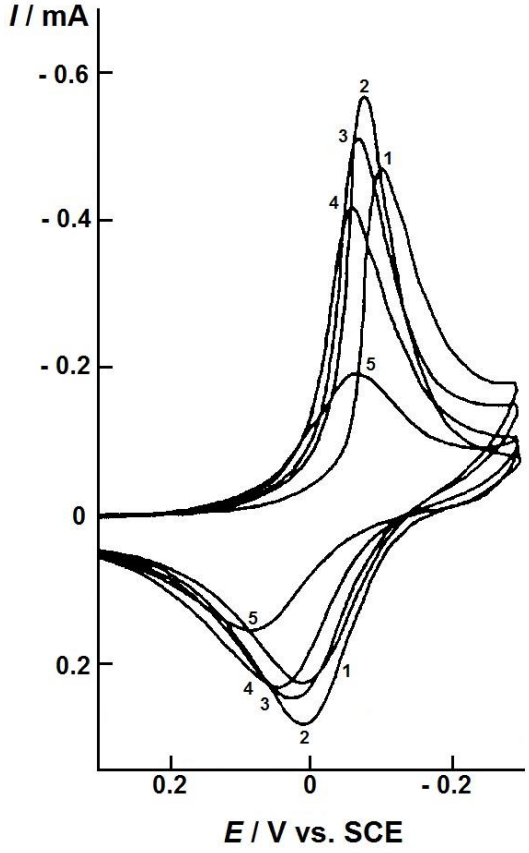

Figure 27. *Cyclic voltammograms of a poly(tetracyanoquinodimethane) electrode in contact with lithium chloride solutions of different concentrations: (1) 0.625, (2) 1.25, (3) 2.5, (4) 5.0 and (5) 10.0 mol dm^{-3}. Scan rate: 60 mV s^{-1} [37]*

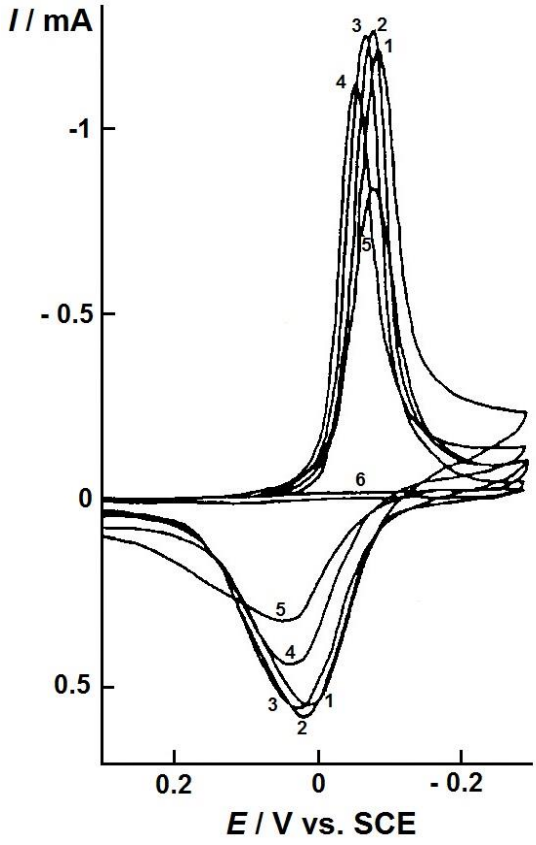

Figure 28. *Cyclic voltammograms of a poly(tetracyanoquinodimethane) electrode in contact with calcium chloride solutions of different concentrations: (1) 0.15, (2) 0.31 (3) 0.625, (4) 1.25, (5) 2.5, (6) 5.0 mol / dm^3 $CaCl_2$. Scan rate: 25 mV s^{-1} [37]*

By employing the empirical equations:

$$c = Z\,(\mathbf{1} + Bc_s^{\mathbf{1/2}}) \tag{1}$$

and

$$D_{ct} = D_{ct}^0(1 - H'c) \tag{2}$$

semi-quantitative description of the effect of concentration on peak currents and peak potentials has been obtained. D_{ct}^{o} is the effective diffusion coefficient of charge transport through the polymer

film in the absence of the addition of supporting electrolyte; *Z*, *B*, and *H′* are empirical parameters characteristic of the system under study. The values of these parameters depend on the nature of the solvent, on the counter-ions (their size and charge), and the polymer forming the film. Combining (1) and (2) with the Randles–Ševčík equation, as well as the appropriate Nernst equation, gives the relationships:

$$I_p = K_i \left[1 - H\left(1 + Bc_s^{1/2}\right)\right]^{1/2}\left(1 + Bc_s^{1/2}\right) \quad (3)$$

and

$$E_p = K_E + \frac{RT}{zF} ln\left\{c_s\left[1 - H\left(1 + Bc_s^{1/2}\right)\right]^{1/2}\right\} \quad (4)$$

where

$K_i = 2.69 \times 10^5 D_{ct}^{o1/2} A v^{1/2} Z$ and $H = ZH'$

$K_E = E_c^{\ominus\prime} - \frac{RT}{zF} ln K \pm 0.0285$.

The constant in the equation of the peak current (K_i) includes the quantities in the Randles–Ševčík equation; *i.e.*, *A* is the electrode area, *v* is the scan rate, and the charge number of the electrode reaction is assumed to be 1. The constant in the equation of the peak potential (K_E) contains the formal potential ($E_c^{\ominus\prime}$) and the formation constant of the salt, ion pair, or complex (*K*). +0.0285 V and −0.0285 V, respectively, have to be used for the anodic and cathodic peak potentials. Where a + or a − sign appears before the term of (*RT* / *zF*) ln*K* depends on the type of ions exchanged. When counter-ions enter the polymer film it is + for reduction and − for oxidation, respectively. For instance, for the reduction of TCNQ the sign is positive. However, when co-ions leave the film, the opposite sign applies, *i.e.*, during oxidation the sign is positive. The most remarkable conclusion of these calculations is the fact that the variation in the I_p and E_p values with c_s can be described with the same set of parameters for a given system. In addition, the variation in *Z*, which is characteristic of the chemical structure of the film, *B*, which in turn is linked to the swelling (solvent–polymer and ion–polymer interactions) and *H*, which expresses how the permeability of the film depends on the sizes of the penetrating ions and the solvent-filled cavities (the free volume in the film), exhibited rather reasonable, systematic changes as the solvent was replaced with a better one or univalent ions were substituted for bivalent ones.

Hysteresis and relaxation phenomena

Despite the quasi-equilibrium character of the cyclic voltammetric curves, a pronounced hysteresis (*i.e.*, a considerable difference between the anodic and cathodic peak potentials) appears. Slow heterogeneous electron transfer, effects of local rearrangements of polymer chains, slow mutual transformations of various electronic species, first-order phase transition due to an S-shaped energy diagram (*e.g.*, due to attractive interactions between the electronic and ionic charges), dimerization, and insufficient conductivity of the film at the beginning of the anodic process have been proposed as possible explanations for the hysteresis (Fig. 29).

Owing to the long relaxation times characteristic of polymeric systems, the equilibrium or steady-state situation is often not reached within the time-scale of the experiment. Fig. 30 shows the change in the resistance of polyaniline after potential steps. The achievement of a constant resistance value takes a rather long time, especially during the conducting-to-insulating transition.

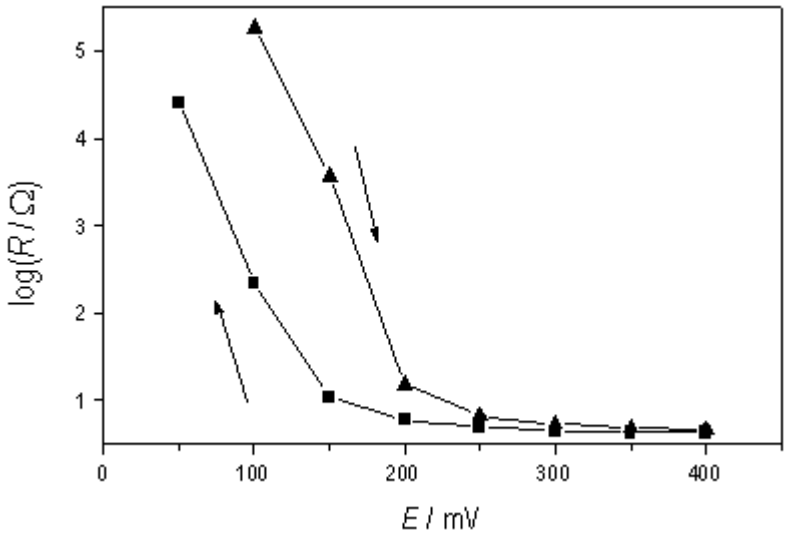

***Figure 29**. The change in the resistance of a polyaniline film in contact with 1 M H_2SO_4 as a function of the potential [7]. Arrows indicate the anodic and cathodic directions of the measurements, respectively*

Consequently, even slow sweep rate cyclic voltammetry does not supply reliable thermodynamic quantities that can otherwise be derived by analyzing the changes in the peak potentials. It is even more striking when the mass change is followed after potential steps. Due to the limited rate of the ion transport and especially the slower solvent transports the constant swelling is achieved often after tens of minutes [38].

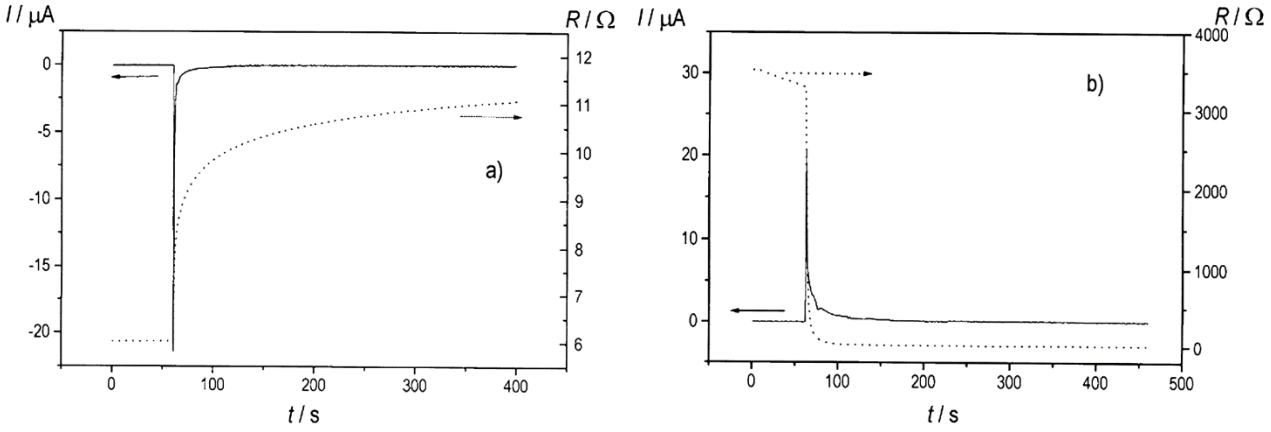

***Figure 30**. The current transients and the respective resistance–time curves obtained after performing potential steps (a) from 0.2 to 0.15 V and (b) from 0.15 to 0.2 V for a PANI electrode in contact with 2 mol dm^{-3} H_2SO_4 [7]*

While the effect of potential-induced relaxation phenomena has been studied extensively, less effort has been expended in exploring the effect of temperature. One notable exception is a temperature shock experiment on a poly(tetracyanoquinodimethane) electrode. It was found that when the electrode returned from elevated temperature to room temperature, a relatively long time (>30 min) was needed to restore the original room-temperature voltammetric response, as seen in Fig. 31.

Apparently, the polymer adopts an extended, perhaps solvent-swollen conformation at elevated temperatures that requires a long time to revert back to the room temperature structure. Such behavior is observed in studies of polymer gels, where varying the temperature results in the hysteresis of macroscopic polymer properties such as swelling, elasticity, turbidity, and so forth.

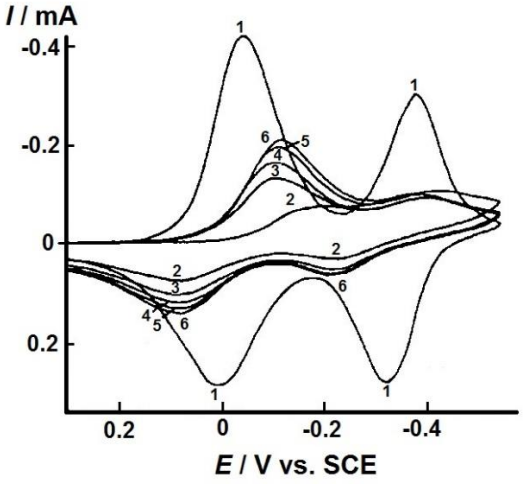

***Figure 31**. Cyclic voltammograms obtained for a poly(tetracyanoquinodimethane) electrode in contact with 10 M LiCl at (1) 69 °C and (2–6) after rapid cooling at 22 °C, recorded after delays of (2) 4, (3) 9, (4) 13.5, (5) 22.5, and (6) 38.5 min [39]*

Break-in and first cycle effects

For a range of neutral polymer films freshly deposited on metal substrates by solvent evaporation techniques several potential sweeps are required for the films to become fully electroactive. This phenomenon has been referred as the break-in effect. The break-in effect is attributed to the incorporation of solvent molecules and ions into the film phase during electrolysis, as well as to potential-dependent morphological changes. The rate of the diffusive transport of solvent molecules depends on the structure of the polymer and the motion of polymer segments. In crystalline and crosslinked polymers, or below the glass transition temperature, the movement of the incorporating species may be rather slow. On the other hand, solvent molecules act as plasticizers, and therefore increase the rate of diffusion for both neutral and ionic species inside the film.

The first cycle or waiting time effects (where the shapes of the cyclic voltammograms and the peak potentials depend on the delay time at potentials at which the polymer is in its neutral / discharged state: see also as "secondary break-in") have been interpreted in terms of slow morphological changes and / or the difficulty removing the remaining charges from insulating surroundings.

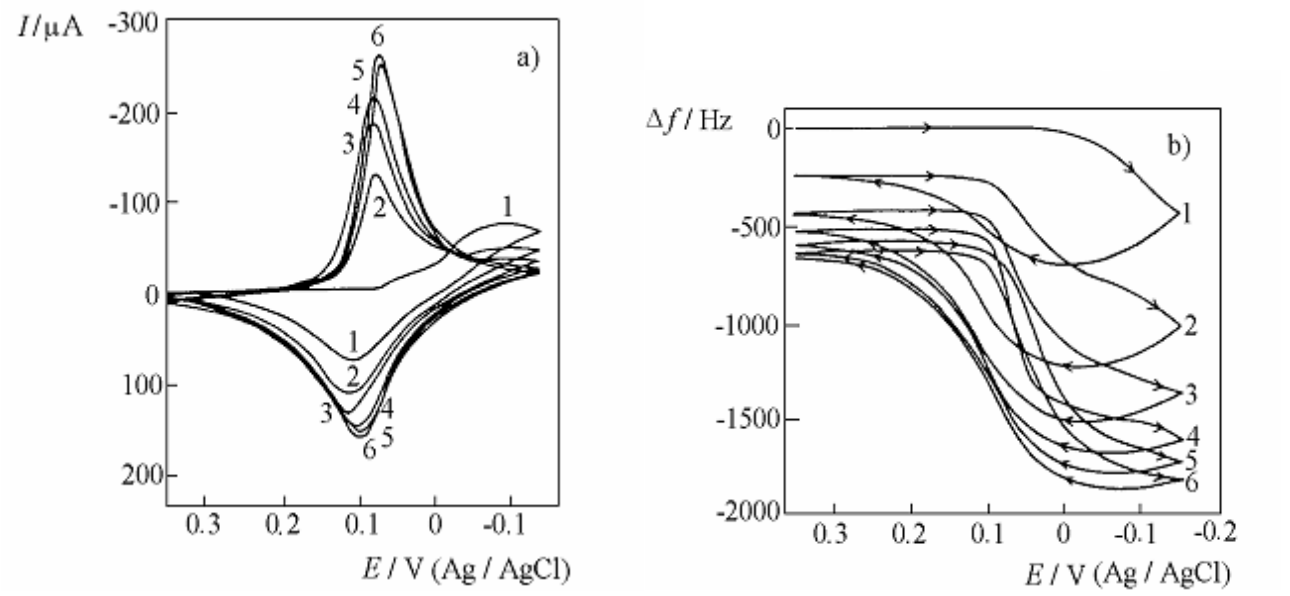

***Figure 32.** "Break-in effect," as observed in cyclic voltammetric and simultaneous EQCN measurements performed with a virgin and thick poly(tetracyanoquinodimethane) electrode. $\Gamma = 7\times10^{-8}$ mol cm^{-2}. Electrolyte: 2.5 M LiCl. Scan rate: 6 mV s^{-1}. a) Consecutive cyclic voltammograms; b) **s**imultaneously obtained EQCM frequency curves [40]*

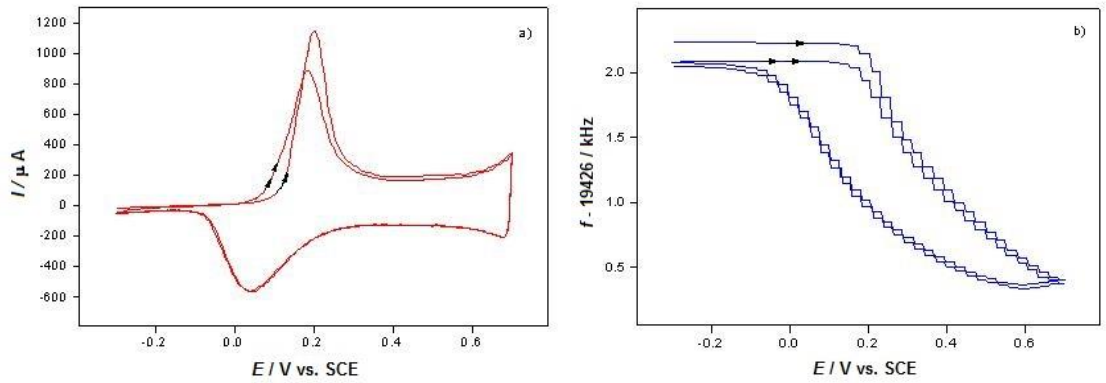

Figure 33. *Cyclic voltammograms (two cycles) a) and the simultaneously detected EQCN frequency changes b) for a polyaniline film (L = 2.9 µm) in contact with 1M H_2SO_4. Scan rate: 100 mV s^{-1} [38]*

Charging/discharging (or redox switching) processes are usually fast, but are rather complex in nature. The steady-state cyclic voltammograms in the case of polyaniline exhibit a combination of broad anodic and cathodic peaks with a plateau in the current at higher potentials (Fig. 33). The current is proportional to the scan rate, *i.e.*, from an electrical point of view the film behaves like a capacitor, however, this simple result is the consequence of a complicated phenomenon which includes a faradaic process (the generation of charged electronic entities at the polymer chains near the electrode surface by electron transfer to the metal), the transport of those species throughout the film, as well as the ion exchange at the film|solution interface. A closer inspection of the curves of Fig. 33 reveals two effects of importance. First, the so-called first-cycle effect, *i.e.*, the first anodic cycle after starting the investigation of a virgin film or after a long waiting time at negative potentials where the polymer is its reduced state, differs from the subsequent ones. The main reason is the incorporation of ions and solvent molecules, and the transformation and relaxation of the structure of the polymer layer. Second, at pH 0 in the beginning of the oxidation the mass change is minor, although a substantial amount of charge has already been injected. The low mass change is due to the low molar mass of H^+ ion, which is the species that leaves the surface layer. The incorporation of the anions, which have a much higher molar mass, clearly manifests itself in the observed EQCN frequency decrease in a later phase of oxidation at higher anodic potentials. Owing to the very high repulsion forces between the nearest-neighbor sites in the polymer chain, it is unfavorable that protons on the nitrogen atom and the benzenoid ring filled with a hole (polaron) should exist next to each other simultaneously. Consequently, deprotonation is a necessary process when positive charges are injected into the polymer.

Characterization

The complete characterization of conducting polymer and composite films, layers, membranes *etc.* includes the determination of all electrochemical properties (formal potential of the redox reaction, charge storage capacity, rates of electron transfers, rates of ionic and electronic charge transport processes, rate of solvent transport and phase equilibria, the mechanism and kinetics of the electrochemical-chemical reactions, the film morphology and all the useful properties, *e.g.*, the changes of color or conductivity. In order to achieve this goal usually several experimental techniques and their combination are needed as it had been mentioned. Furthermore, it is always worth to apply the variation of experimental conditions because in this, relatively simple way essential information can be obtained about the reaction mechanism, different interactions

between the polymer and the ions and molecules present. Two examples will be shown: the effect of the nature of electrolyte and the pH dependence.

Already the cyclic voltammograms reveal the strength of interaction between the polymer and the counter-ions but by using combined methods *e.g.*, EQCN, the transport and sorption of ions and solvent molecules can be understood by the help of such easy experiments.

Poly(vinylferrocene) is more swollen in the presence of SO_4^{2-} ions than in NO_3^- or ClO_4^-- containing electrolytes. This means that the different anions enter the film together with their hydration spheres, since the magnitude of the mass change is as follows: sulfate > nitrate > perchlorate. This corresponds to the order of degree of hydration of these anions. On the other hand, the ion-pair formation constant for the oxidized sites and the ClO_4^- - ions is greater than that for NO_3^- or SO_4^{2-} ions, which is reflected in the more positive formal potential of the ferrocene/ferricenium redox couple in Na_2SO_4 or $NaNO_3$ solutions compared with $NaClO_4$ electrolyte, as seen in Fig. 34. The more pronounced swelling also reflects the more extensive interaction between water and the charged ferricenium sites in the presence of SO_4^{2-} - or NO_3^- - compared to ClO_4^- -containing electrolytes.

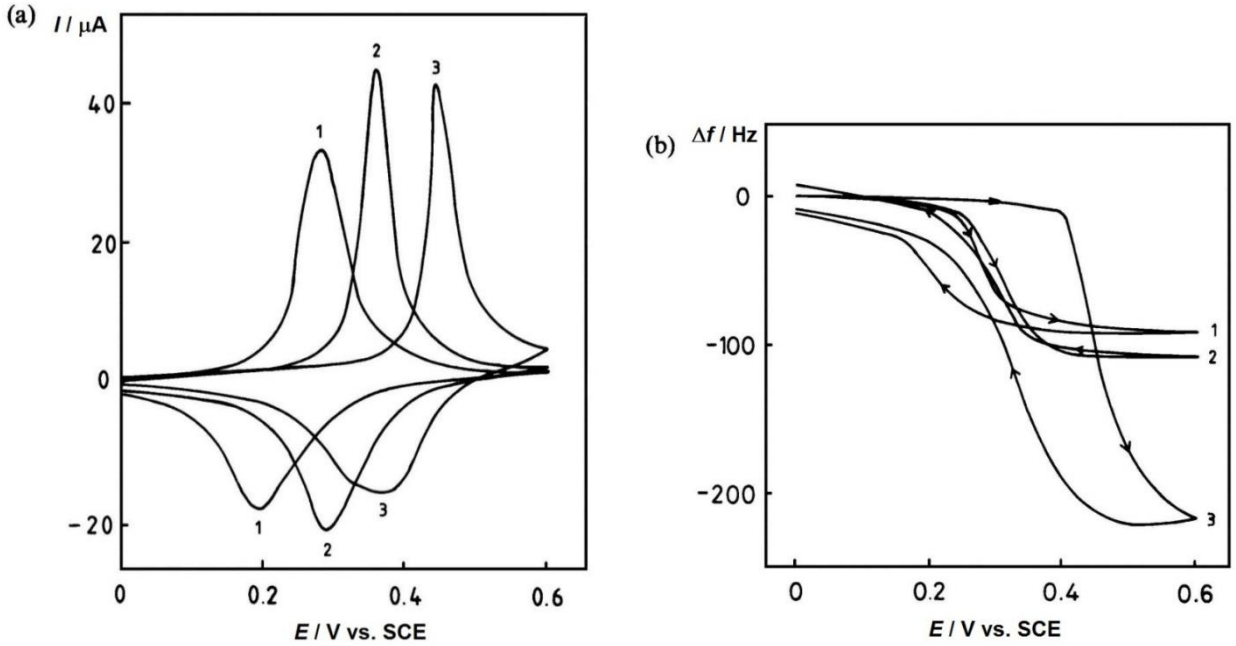

***Figure 34**. Cyclic voltammograms (**a**) and the simultaneously recorded EQCN curves (**b**) for an electrochemically deposited poly(vinylferrocene) film in contact with (1) $NaClO_4$; (2) $NaNO_3$; and (3) $Na_2SO_4|H_2SO_4$ pH 3.4, respectively. Electrolyte concentration: 0.5 mol dm^{-3}. Scan rate: 10 mV s^{-1}. [40]*

Because the polymers under study are organic compounds and/or contain groups available for protonation the execution of the experiments at different pH values is inevitable since the electron transfer steps are accompanied by protonation or deprotonation. As an example, the cyclic voltammograms obtained at different pH values in sulfate electrolytes for a poly(copper phthalocyanine) [poly(CuPc)] layer are presented (Fig. 35). It is evident that H^+ ions participate in the redox processes since with increasing pH the voltammetric peaks shift into the direction of the more negative potentials by –65 ± 5 mV/pH. Therefore, we can conclude that the redox reaction of poly(CuPc) is basically a 1 H^+/1 e^- or 2 H^+/2 e^- reaction. Albeit this reaction is much more complicated, and the electron transfers are accompanied with dimerization and morphological changes, the pH dependence serves as a starting point [41].

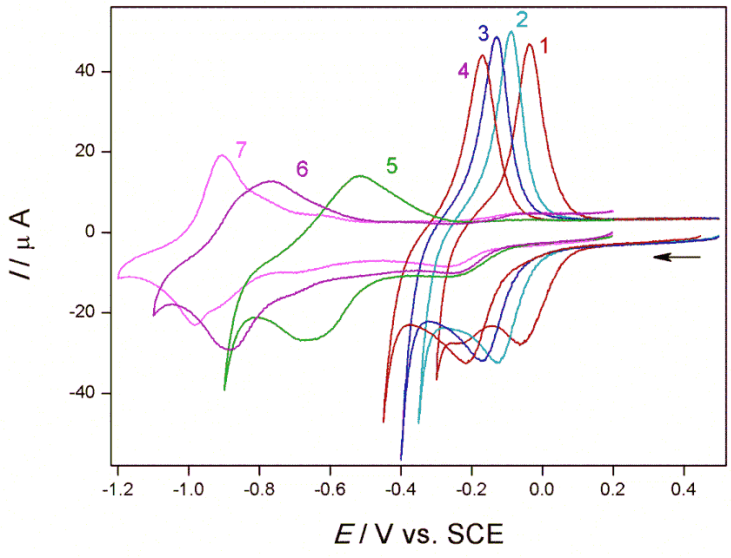

***Figure 35**. Au|poly(CuPc) electrode in contact with sulphate electrolytes (H_2SO_4 or H_2SO_4 + Na_2SO_4 or Na_2SO_4 + NaOH) pH values: 0.3 (1), 1.18 (2), 2.17 (3) 2.57, (4), 7.8 (5), 11.1 (6) and 12.7 (7). Scan rate: 10 mV s^{-1}. The total concentration of the sulfate ions was kept practically constant at 0.5 mol dm^{-3} [41]*

Applications

Material Properties of Conducting Polymers

Electronically conducting polymers can be prepared from cheap compounds such as aniline, pyrrole, thiophene and their derivatives by relatively simple chemical or electrochemical polymerization processes. Redox polymers are also applied in special cases, such as in biosensors or electrochromic display devices. Redox processes combined with the intercalation of anions or cations can therefore be used to switch the chemical, optical, electrical, magnetic, mechanic and ionic properties of such polymers. These properties can be modified by varying the anion size and preparation techniques; by including other chemical species for example. A qualitative summary of the relationship between the properties of a conducting polymer and its charge state is given in Table 1.

***Table 1.** Qualitative properties of conducting polymers that conduct in their oxidized state, as a function of their charge state [6]*

Properties/Charging state	Reduced	Oxidized
Stoichiometry	without anions (or: with cations)	with anions (or without cations)
Content of solvent	smaller	higher
Volume	smaller	higher
Color	transparent or bright	dark
Electronic conductivity	insulating, semiconducting	semiconducting, metallic
Ionic conductivity	smaller	high
Diffusion of molecules	dependent on structure	
Surface tension	hydrophobic	hydrophilic

Typical areas in which conducting polymers are applied can be described using a double logarithmic plot of ionic resistance versus electronic resistance, as shown in Fig. 36.

The positions of ideal metals, semiconductors and insulators in the diagram are shown at the top. Constant properties exist at high ionic resistances, *i.e.*, towards the top of the diagram. Here, ICPs can be applied in the dry state in an inert atmosphere. Contact with an electrolyte leads to a much wider field of applications, depending on the specific ionic and electronic resistances associated with the charge state, such as in batteries, displays, sensors, *etc.*

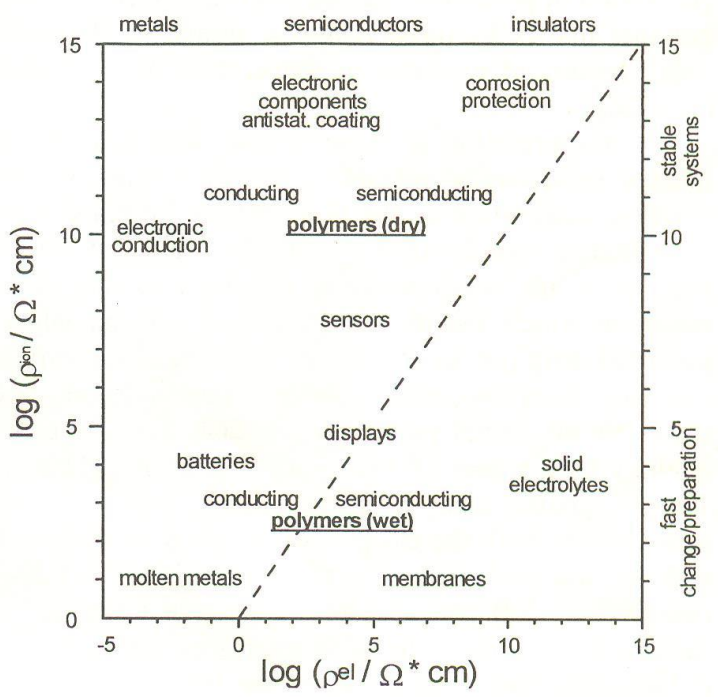

***Figure 36**. Double logarithmic plot of ionic resistance versus electronic resistance for conducting polymers, showing areas of application [6]*

Gas sensors

Gas sensors made of conducting polymers have high sensitivities and short response times, and —a great advantage compared with most commercially available sensors based on metal oxides— work at room temperature. The sensing principles employed in gas sensors using conducting polymers as active sensing materials vary. The principle used depends on the variables (resistance, current, absorbance, mass, *etc.*) measured and the type of interaction between the gas (analyte) and the polymer. The oxidation state (the charge or doping level) of the polymer is altered by the transfer of electrons from the analyte to the polymer, which causes a change in the properties (resistance, color, work function, *etc.*) of the polymer.

For instance, electron-donor gases such as NH_3 increase the resistance of polyaniline (PANI) because the electrons transferred neutralize the positive sites (polarons), and the polymer becomes neutral. Interestingly this is a reversible process; after flushing the polymer with air, the conductivity of the polymer (sensing layer) is recovered (Figs. 37-39).

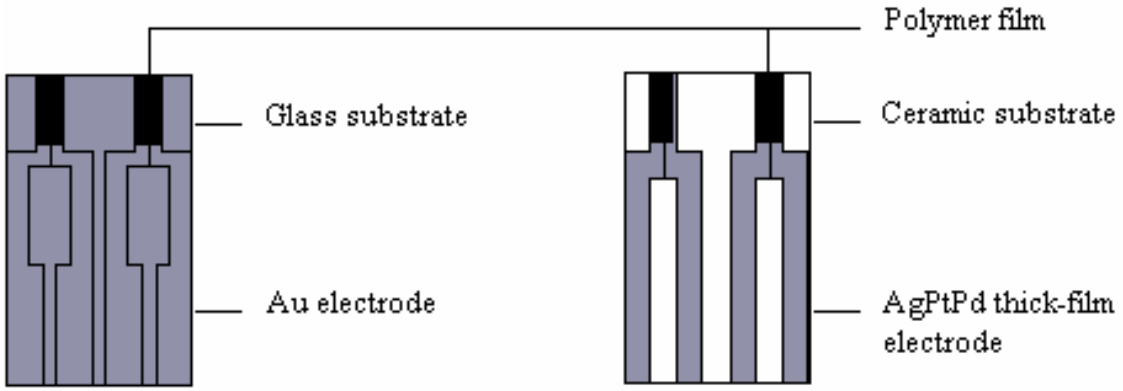

***Figure 37.** Layout designs of thin-film and thick-film polymer gas sensors [42]*

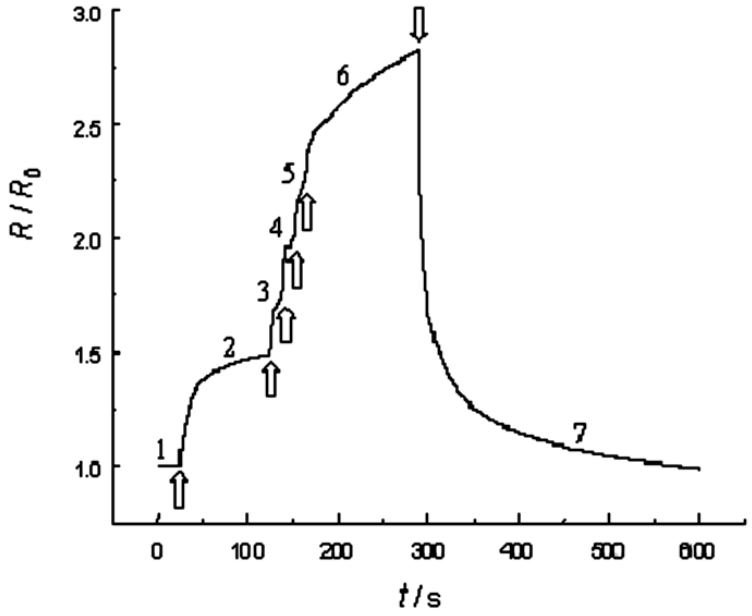

***Figure 38**. The response of a PANI gas sensor (relative resistance vs. time curves at 20 °C). 10 ppm ammonia was injected into the air at times indicated by the arrows. The total concentrations were: (1) 0, (2) 10, (3) 20, (4) 30, (5) 40, (6) 50 ppm; and (7) after flushing with clean air again [43]*

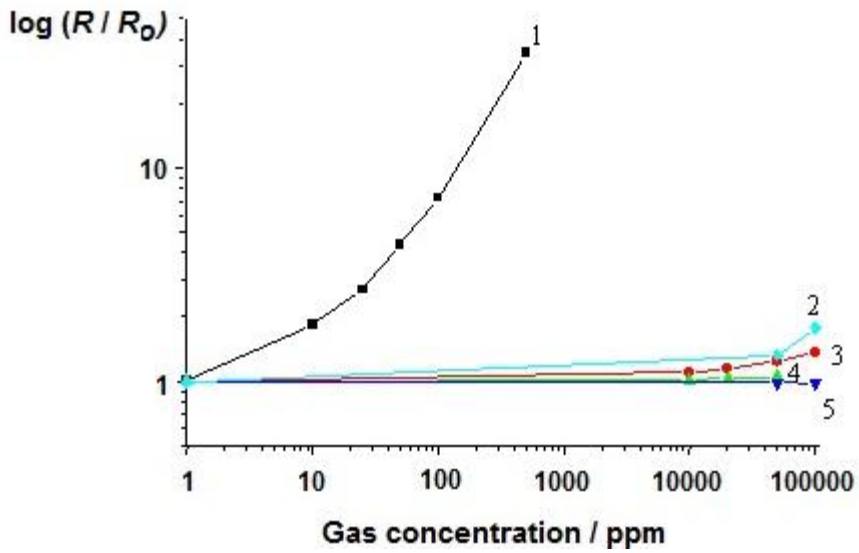

***Figure 39**. The response of a PANI ammonia sensor (log relative resistance–gas concentration plot) for different gases and vapors: (1) ammonia; (2) methanol; (3) ethanol; (4) CO; and (5) NO; at room temperature [43]*

Other sensors and biosensors

The use of conducting polymers as amperometric sensors, where the detection signal is amplified due to the catalytic properties of the polymer and / or built-in catalytic entities, is straightforward, although the application of these systems as ion-selective electrodes in potentiometry is problematic because redox state and acid–base or ionic equilibria need to be controlled simultaneously.

Poly(methylene blue) is a very good catalyst for the oxidation of hemoglobin. This property has been utilized in an amperometric sensor (see Figs. 40 and 41). A good correlation was found between the results of the electrochemical method and those of the spectrophotometric cyanidation analysis method, which is used in clinical practice as a standardized protocol [44].

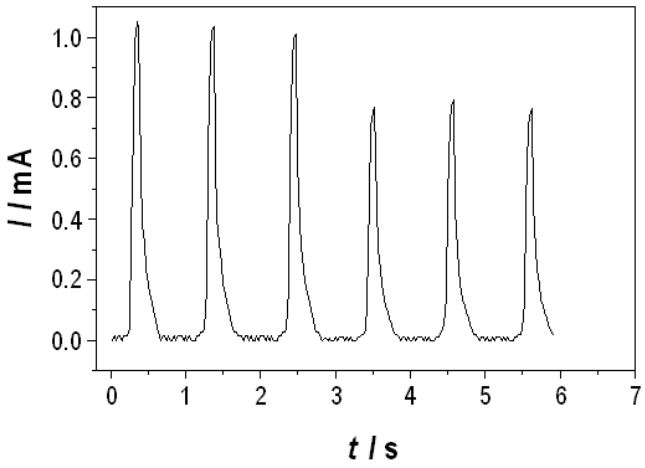

***Figure 40**. Chronoamperometric responses for consecutive injections into a flow cell of samples of whole blood diluted 1:10 in phosphate buffer (pH 6.24) and 0.5 mol dm^{-3} NaCl on a poly(methylene blue) electrode at E = 0.4 V vs. SCE. Flow rate: 4 ml min^{-1}. The tall and short waves are the responses to 6 cm^3 and 4 cm^3 dilute solutions, respectively [44]*

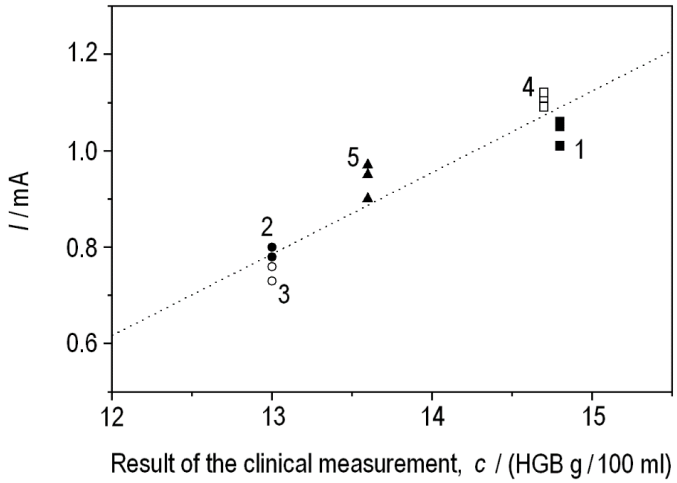

***Figure 41**. Comparison between electrochemical and cyanidation methods for the analysis of blood samples provided by five donors. Blood samples 2 and 3 were from females, while 1 and 4 were from male patients. Patients 1–4 were healthy, while patient 5 was a potentially ill donor. Experimental conditions were the same as for Fig. 40 [44]*

Electrochromic display devices

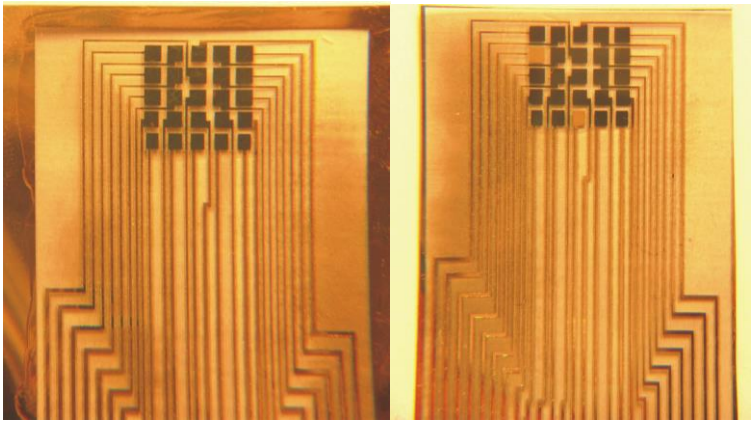

***Figure 42.** Photos of a PANI-based flexible electrochromic display device containing 25 pixels. The display region and the connections were made by depositing gold on a plastic sheet using an appropriate mask and an evaporation technique. Each pixel can be driven separately. Left: PANI is in its oxidized state in all pixels. Right: PANI is reduced in two pixels (the bleached ones)*

Due to its many advantageous properties (low cost, fast color change, good contrast, stability, *etc.*), PANI is also a favorite material for use in electrochromic display devices. Pictures of a PANI-based flexible device are shown in Fig. 42. The display pattern, which consists of 25 pixels and the connections that allow each pixel to be driven separately, was fabricated by depositing gold onto a plastic sheet. Another plastic sheet covers the display. The electrochemical switching is executed using a counter electrode, which also serves as a reference electrode, and an acidic gel electrolyte is placed between the two sealed plastic sheets.

Supercapacitors

In electric and hybrid vehicles during acceleration a high power density is needed or in backup power devices the fast response is crucial. Supercapacitors are ideal for these purposes, and that is the very reason for the intense quest regarding electrode materials, which can meet the requirements of reversibility, long-term stability, the high storage capacity and the fast charging/discharging characteristics.

Among the different metal oxides, the properly prepared hydrous RuO_2 shows the best properties. Its commercial use is, however, hindered due its high cost and limited availability. Another class of materials, which in principle is suitable for supercapacitor applications are the electrically conducting polymers. These materials are cheap, show reversible redox behavior and high capacitance, but their long-term stability is not good enough. The combinations of RuO_2 with conducting polymers seem to be a promising attempt to have a possible synergic effect, *i.e.*, simultaneously improving the electron transport, stability and decreasing the cost. A simple method resulting in a well-defined, well-dispersed RuO_2–polyaniline composite on the electrode surface is the use of the oxidation power of Ru (IV) that is the ability of RuO_2 crystals attached to the electrode surface to oxidize the aniline which process resulting in the formation of PANI on the external and internal surfaces of RuO_2 crystals [45]. The EQCN frequency decrease indicates the deposition of polyaniline (Fig. 42). The reduced ruthenium sites can be regenerated by using short positive potential pulses (Fig. 43).

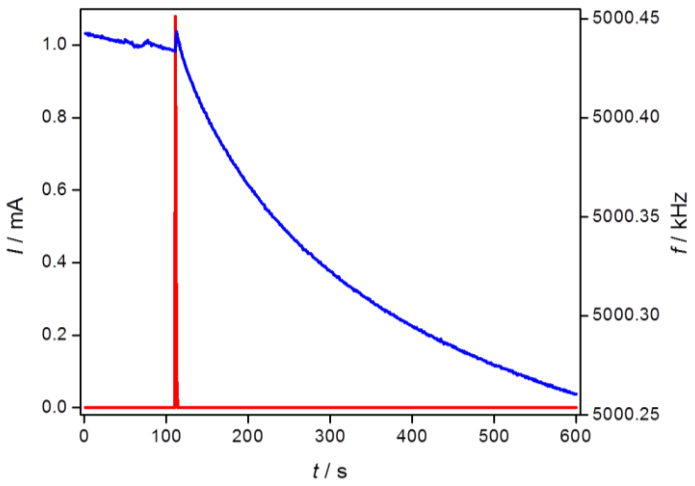

Figure 42. *(a) The EQCN frequency change vs. time curve (blue) observed for an Au|RuO_2 electrode after the addition of aniline into 0.5 M H_2SO_4 solution at open-circuit potential (0.85 V). The RuO_2 has been oxidized previously (current peak) [45]*

The respective cyclic voltammograms and EQCN curves are displayed in Figs. 44-46. After the first deposition step the response of the polyaniline appears, however, the response originating from RuO_2 dominates. Following further deposition steps the mass change during cycling also becomes higher, however, in the potential region of the leucoemeraldine – emeraldine transition, *i.e.*, from

–0.1 to 0.15 V the frequency change is mostly due to processes occurring simultaneously with the oxidation of the lower valence Ru sites. In acid media the EQCN response of the PANI is minor because only deprotonation takes place, and H^+ ions leave the surface phase. On the other hand, after the peak the incorporation of anions manifests itself in a frequency decrease. The effect of PANI is even better seen when a more positive switching potential is applied. At more positive potentials the second pair of waves due to the transition of the emeraldine form to pernigraniline form is nicely seen. In this case the redox transformation is accompanied by the desorption of anions and H^+ ions which causes a substantial mass loss.

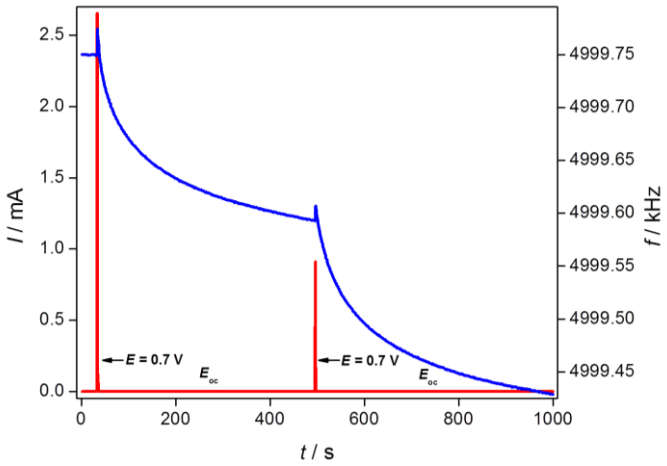

Figure 43. *The continuation of the experiment presented in Fig. 42. The EQCN frequency change* vs. *time curve observed for the Au | RuO_2 electrode after two additional reoxidation pulses [45]*

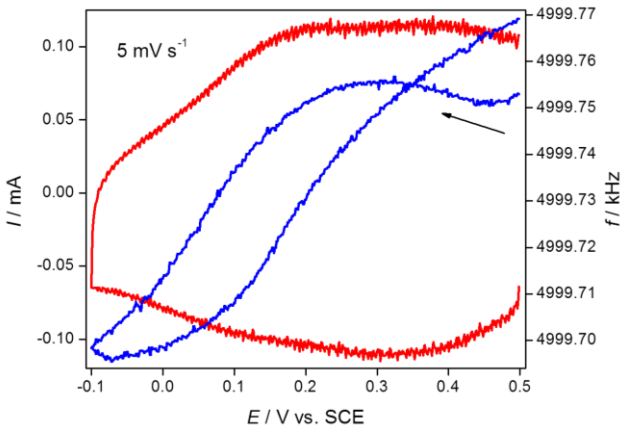

Figure 44. *Cyclic voltammogram (red) and the simultaneously obtained EQCN frequency response (blue) for the Au | RuO_2 + PANI electrode prepared above. Scan rate: 5 mV s^{-1}, Potential range: –0.15 – 0.5 V. Electrolyte: 0.5 M H_2SO_4 [45]*

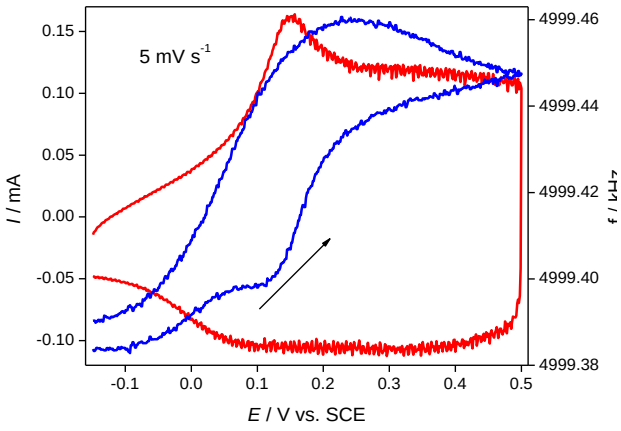

Figure 45. *Cyclic voltammogram (red) and the simultaneously obtained EQCN frequency response (blue) for the Au | RuO_2 + PANI electrode after three successive activation pulses. Scan rate: 5 mV s^{-1}, Potential range: –0.15 – 0.5 V. Electrolyte: 0.5 M H_2SO_4 [45]*

Fig. 46 shows the cyclic EQCN responses by using an extended potential range at pH 3.5.

One of the important features of the RuO_2/PANI composite is that the electrochemical activity of the polyaniline is remarkably preserved at higher pH values even at pH 7 a reasonable capacitive response can be obtained. For the RuO_2 samples used in this study in contact with 0.5 M H_2SO_4 solution the specific capacitance was found to be 540 $\pm$ 40 F g^{-1} in the potential range of –0.1 and 0.85 V at a scan rate of 20 mV s^{-1}. By PANI deposition, the specific capacitance can be increased as high as by 50 % without practical deterioration of the response time or stability. After successive

cycling in sulfuric acid the capacitance loss is not higher than 10-15 % after 1000 cycles. Even in some cases there is an increase of capacitance during cycling which is most likely due to the completion of hydration and sorption of electrolyte which enhances the ionic charge transfer in the pores of RuO_2 and polyaniline.

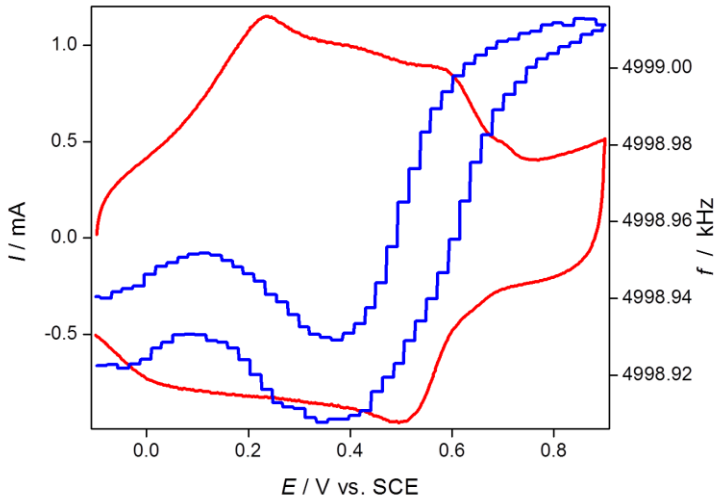

Figure 46. *Cyclic voltammogram (red) and the simultaneously obtained EQCN frequency response (blue) for the Au│ RuO_2 + PANI electrode after three successive activation pulses. Scan rate: 50 mV s^{-1}, Potential range: - 0.15 – 0.9 V. Electrolyte: 0.5 M H_2SO_4 + Na_2SO_4 pH 3.5 [45]*

New trends

In the last two decades the researchers have started to apply novel approaches. The new trend is the fabrication of composites including nanocomposites of polymers and other materials such as carbon nanotubes, graphene or inorganic compounds having special structure and properties. In sensors and biosensors of different kinds (conductometric, impedimetric, potentiometric, amperometric and voltammetric) conducting polymers are used as active, sensing or catalytic layers, however, in the majority of applications those serve as matrices entrapping enzymes or other biologically active compounds. The biocompatibility of several conducting polymers provides opportunity for the application in medicine as artificial muscles and limbs, as well as artificial nerves. The biomimetic (bionic) applications certainly will continue in the future. Microsystem technologies have been replacing by nanosystem technologies. More sophisticated and combined techniques have been developed, and have become widespread tools in the laboratories all around the world; *e.g.*, scanning microscopies, or the new versions of electrochemical quartz crystal nanobalance.

In the recent years we have reached a deeper level of understanding of the behavior of these systems that we can use to improve the performance of the devices based or use conducting polymers. The improvement occurs either by a fine-tuning of already promising systems or by using more sophisticated compositions and structures. Less often a quest of entirely novel applications has also been reported, however, most of the directions have already been set out 10-30 years ago. The use of the derivatives of the monomers or copolymerization of different monomers may be an option to obtain conducting polymers, which are more flexible or rigid or even crystalline for *e.g.*, heterojunction solar cells, as well as which are mechanically and chemically more stable, have a more advantageous processability *etc.* The functionalization of conducting polymers, which leads to smart materials interacting and responding to their environment, is also a great opportunity. The preparation of self-doped polymers is also a good way to overcome the problems of the ionic charge

transport during redox switching and other limitations of the use of the polymer. The other possibility is a combination of the arsenal of materials science with chemistry (electrochemistry) to improve the properties for special purposes. Nanocomposites, hybrid materials based on conducting polymers certainly become and will be important materials in the future. There is a high expectation concerning electroconducting nanomaterials such as nanofibers, nanorods and other nanostructures based on the supramolecular self-assembly of conducting polymers, *e.g.*, in the enhancement of the photoluminescence efficiency by utilization of the energy and charge transfer effect in surface resonance coupling. Manipulation of the microstructures of polymers may improve the performances of both the polymer-based transistors and electrochemical cells. There will be tasks for the chemists, electrochemists in the production and characterization of new materials, for the theoreticians to explain the phenomena observed or will be observed and to predict new opportunities, and also engineers to give a final form of the devices. The conducting polymers are relatively cheap materials; however, the specially improved properties can give a further boost concerning the mass production, which makes the products much less expensive. For instance, making ink from conducting polymers opens up new horizons for printing sensors, electronic circuits, solar cells, light emitting displays *etc.* The new trends can nicely be followed by studying the literature including papers and the topics of conferences.

Conclusions

Based on the review of the achievements during the last 40 years we can draw the conclusion that the development in the field of conducting polymers is unbroken, and we still expect new discoveries and novel utilizations in several areas such as energy storage and power sources, photovoltaics, health care, and different technologies.

References

[1] G. Inzelt, Recent advances in the field of conducting polymers. *Journal of Solid State Electrochemistry* **21** (2017) 1965–1975.
[2] G. Inzelt, *Conducting polymers - A new era in electrochemistry,* 2nd edn. In: F. Scholz (ed) Monographs in electrochemistry, Springer, Heidelberg, Berlin, Germany, 2012.
[3] G. Inzelt, Journal of Solid State Electrochemistry **15** (2011) 1711-1718.
[4] G. Inzelt: *Mechanism of Charge Transport in Polymer Modified Electrodes*, In: Electroanalytical Chemistry, A Series of Advances, A.J. Bard (ed.), Vol. 18, Marcel Dekker, Inc., New York, USA, 1994. pp. 89-241.
[5] G. Inzelt, *Charge transport in polymer modified electrodes*, Encyclopedia of Electrochemistry, A.J. Bard, M. Stratmann (eds.) Functions and applications of modified electrodes Vol. 10, I. Rubinstein, J. Rusling, M. Fujihara (eds.), Weinheim, Wiley-VCH, 2007. Ch. 9, pp. 651-683.
[6] G. Inzelt, M. Pineri, J.W. Schultze, M.A. Vorotyntsev, *Electrochimica Acta* **45** (2000): 2403-2421.
[7] E. Csahók, E. Vieil, G. Inzelt, *Journal of Electroanalytical Che*mistry **482** (2000) 168-177.
[8] G. Inzelt, E. Csahok,V. Kertész, *Electrochimica Acta* **46** (2001) 3955-3962.
[9] H. Shirakawa, E. J. Louis, A. G. MacDiarmid, C. K. Chiang, A. J. Heeger, *Journal of Chemical Society Chemical Commununications* (1977) 579-580.
[10] C. K. Chiang, C. R, Fischer, Y.W. Park, A. J. Heeger, H. Shirakawa, E. J. Louis S. C. Gau, A. G. MacDiarmid, *Physical Review Letters* **39** (1977) 1098-1101.
[11] C. K. Chiang, M. A. Druy, S. C. Gau, A. J. Heeger, E. J. Louis, A. G. MacDiarmid, Y. W.Park, H. Shirakawa, *Journal of American Chemical Society* **100** (1978) 1013-1015.
[12] H. Shirakawa Angewandte Chemie International Edition **40** (2001) 2574-2580.
[13] A. G. MacDiarmid, *Angewandte Chemie International Edition* **40** (2001) 2581-2590.
[14] A. J. Heeger, *Angewandte Chemie International Edition* **40** (2001) 2591-2611.
[15] H. Letheby *Journal of Chemical Society* **15** (1862) 161-163.

[16] J. Fritzsche, Journal für praktische Chemie, 20 (1840) 453–457.
[17] N. E. Khomutov, S. V. Gorbachev *Zhurnal Fizichekoi Khimii* **24** (1950) 1101-1106.
[18] D. M. Mohilner, R. N. Adams, W. J. Argersinger, *Journal of Electrochemical Society* **84** (1962) 3618-3622.
[19] R. deSurville, M. Josefowicz, L. T. Yu, J. Perichon, R. Buvet, *Electrochimica Acta* **13** (1968) 1451-1458.
[20] A. F. Diaz, J. A. Logan, *Journal of Electroanalytical Che*mistry **111** (1980) 111-114.
[21] G. Inzelt, G.G. Láng: *Electrochemical Impedance Spectroscopy (EIS) for Polymer Characterization* In: Electropolymerization (eds. S. Cosnier and A. Karyakin) Wiley-VCH, Weinheim, Germany, 2010, pp. 51-76.
[22] Electroanalytical Methods, Guide to Experiments and Applications 2nd, revised and extended edition (ed. F. Scholz), Springer-Verlag, Berlin Heidelberg, 2010.
[23] Cs. Visy, In situ combined electrochemical techniques for conducting polymers, Springer, Berlin, Heidelberg, 2017.
[24] G. G. Láng, C. A. Barbero, *Laser techniques for the study of electrode.* In: F. Scholz (ed) *Monographs in electrochemistry*. Springer, Berlin, Heidelberg, 2012.
[25] J. Heinze, B. A. Frontana-Uribe, S. Ludwigs, *Chemical Reviews* **110** (2010) 4724-4771
[26] Electropolymerization (eds. S. Cosnier and A. Karyakin) Wiley-VCH, Weinheim, Germany, 2010.
[27] B. B. Berkes, Á. Nemes, C. E. Moore, F. Szabó, G. Inzelt, *Journal of Solid State Electrochemistry* **17** (2013) 3067–3074.
[28] S. Pruneanu, E. Csahók, V. Kertész, G. Inzelt, *Electrochimica Acta* **43** (1998) 2305-2323.
[29] B. B. Berkes, G. Inzelt, E. Vass, *Electrochimica Acta* **96** (2013) 51-60.
[30] B. B. Berkes, G. Inzelt, *Electrochimica Act*a **122** (2014) 11-15.
[31] B. B. Berkes, A. S. Bandarenka, G. Inzelt, *Journal of Physical Chemistry C – Nanomaterials and Interfaces* **119** (2015) 1996-2003.
[32] G. Inzelt, R.W. Day, J.F. Kinstle, J.Q. Chambers, *Journal of Physical Chemistry* 87 (1983) 4592-4598.
[33] G. Inzelt, G. Horányi, *Journal of Electroanalytical Chemistry*, **230** (1987) 257-265.
[34] B. B. Berkes, S. Vesztergom, G. Inzelt, *Journal of Electroanalytical Che*mistry **719** (2014) 41–46.
[35] G. Inzelt, L. Szabó, J. Q. Chambers, R. W. Day, *Journal of Electroanalytical Chemistry*, **242** (1988) 265-275.
[36] G. Inzelt, Journal of Electroanalytical Chemistry, **279** (1990) 169-178.
[37] G. Inzelt, J. Q. Chambers, J. Bácskai, R. W. Day, *Journal of Electroanalytical Chemistry*, **201** (1986) 301-314.
[38] G. Inzelt, *Electrochimica Acta* **45** (2000) 3865-3876.
[39] J. Bácskai, G. Inzelt, *Journal of Electroanalytical Chemistry* **310** (1991) 379-389
[40] G. Inzelt, J. Bácskai, *Electrochimica Acta* **37** (1992) 647-654.
[41] K. Borsos, G. Inzelt, *Journal of Solid State Electrochemistry* **19** (2015) 2565–2577.
[42] G. Harsányi, M. Réczey, R. Dobay, I. Lepsényi, Zs. Illyefalvi – Vitéz, J. Van den Steen, A. Vervaet, W. Reinert, J. Urbancik, A. Guljajev, Cs. Visy, Gy. Inzelt, I. Bársony, *Sensor Review*, **19** (1999) 128 – 134.
[43] I. Lepcsényi, A. Reichardt, G. Inzelt, G. Harsányi, *Proceeding of 12th European Microelectronics and Packaging Conference*, Harrogate, UK, 1999. pp. 301-305.
[44] C. M. A. Brett, G. Inzelt, V. Kertesz, *Analytica Chimica Acta*, **385** (1999) 119-123.
[45] S. Sopcic, M. Kraljic-Rokovic, Z. Mandic, G. Inzelt, *Journal of Solid State Electrochemistry*, **14** (2010) 2021-2026.

J. Electrochem. Sci. Eng. **8(1)** (2018) 39-47; DOI: http://dx.doi.org/10.5599/jese.445

Open Access : : ISSN 1847-9286

www.jESE-online.org

Original scientific paper

Electrochemical behaviour of electrodeposited Pd and PdNi coatings for the ethanol oxidation reaction in alkaline solution

Jelena D. Lović✉, Vladimir D. Jović[1]

ICTM, Department of Electrochemistry, University of Belgrade, Njegoševa 12, 11000, Belgrade, Serbia

[1]Institute for Multidisciplinary Research, University of Belgrade, Kneza Višeslava 1, 11030, Belgrade, Serbia

Corresponding authors E-mail: ✉jlovic@tmf.bg.ac.rs; Tel.: +381-11-337-0389; Fax: +381-11-337-0389

Received: September 19, 2017; Accepted: October 25, 2017

Abstract

Electrodeposited Pd and PdNi coating samples were tested for ethanol oxidation reaction (EOR) in alkaline solution using cyclic voltammetry (CV), chronoamperometric (CA) and quasi steady-state measurements. All alloy samples showed higher current densities for the EOR than pure Pd coating. The current density increased with increasing the amount of Pd in the PdNi coating and the most active one was found to be Pd0.74Ni0.26. Based on CA measurements a pseudo-steady state is achieved after 1500 s showing that Pd0.74Ni0.26 is more efficient and poisoning more tolerant than other investigated coatings. Upon the end of the current-time transient, the investigated catalysts were subjected to the potential cycling showing the ability to recover activity loss implying the surface composition stability of binary coatings.

Keywords

Palladium; Nickel; Stability

Introduction

Among the different types of fuel cells, direct alcohol fuel cells possess besides high energy densities, low pollutant emissions and low operating temperatures (60–100 °C) [1-3]. Alkaline direct ethanol fuel cells (ADAFCs) is recognized as promising power source because ethanol has higher energy density and lower toxicity compared to methanol [4]. Anode catalysts with high catalytic activities as well as good poison resistances are of great significance to the commercialization of ADAFCs. For alcohol oxidations, Pd-based nanocatalysts are superior to Pt-based catalysts in alkaline media and are widely used as anode catalysts in ADAFCs [1,5].

For the sake of commercialization, the activity and stability of pure Pd needs improvement which could be achieved by combining Pd with other metals or metal oxides. It has been reported that modifications of the Pd nanocatalyst by metals such as Ni [6-8], Au [9,10], Cu [10,11], Ag [10,12], Co [10, 13] effectively improve the catalytic performances of the Pd nanocatalyst toward alcohol oxidations in alkaline media.

Nickel has been used to modify anode catalysts due to its high electrochemical stability in alkaline media and the low cost. Nickel-modified Pd electrodes have been reported as catalysts with excellent performances in ethanol oxidation reaction (EOR) such as the activity, the low overpotentials and the improved poison resistances. Examined parameters of EOR such as onset potential reaction and long-term stability show that among a series of graphene (G)-supported Ni_xPd_{100-x} binary alloyed catalysts, $Ni_{50}Pd_{50}$/G catalyst exhibits 60 mV lower onset potential compare to Ni_0Pd_{100}/G catalysts and current density approximately 8, 4, and 1.7 times superior than that of $Ni_{75}Pd_{25}$, Ni_0Pd_{100}/G, and $Ni_{25}Pd_{75}$/G catalysts, respectively [6]. The mass activity of the $Pd_{83}Ni_{17}$ hollow nanospheres aerogel is 5.6-fold higher than that of the commercial Pd/C catalyst [14] while the mass activity of porous bimetallic PdNi catalyst is 3.5 times higher compared to the commercial Pd/C [15]. It is revealed that the onset potential is ~80 mV lower and the peak current is about 3 times higher for ethanol oxidation using multi-walled carbon nanotubes (MWCNT) catalysts with $Pd_1Ni_{1.5}$ compared to those of Pd/MWCNTs due to the small particle size and high crystallinity of binary catalyst [16] although it can be found that binary $Pd_{3.7}Ni_1$ nanocatalyst with ultra-low loading of metals immobilized on MWCNT exhibits anodic current density over 11 times higher than on the Pd/MWCNT [17]. The electro-catalytic activity of the carbon nanofibers (CNF) supported Pd–Ni nanoparticles prepared by chemical reduction with $NaBH_4$ was examined for EOR show that the onset potential was 200 mV lower and the peak current density 4 times higher compared to that for Pd/C as a result of the uniform distribution of metal nanoparticles on the CNF support while the significant increase in reaction kinetics was achieve by raising the temperature to 60 °C [7]. Negatively shifted onset potential and doubled peak current density in potentiodynamic measurements for core-shell Ni-Pd/C compared to Pd/C was found [18], while high activity and excellent stability during continuously cycling were found for Pd supported on Ni foam [19,20].

It was proposed that the ligand and strain effects contribute the enhanced activity of Pd in the presence of Ni. Namely the insertion of smaller Ni atoms into the Pd crystal lattice causes a contraction of the Pd lattice. This causes a downshift of the Pd d-band center and consequently leads to weaker bonding with adsorbates such as poisoning intermediates in the EOR. Besides, Pd has a higher ionization energy than Ni and because of that Ni atoms become positively charged, facilitating the formation of oxides on Ni [21,22]. Generated OH_{ad} species of Ni participate in the oxidative desorption of intermediates in the EOR enhancing the activity of binary PdNi catalysts.

The electrochemical methods for the preparation of metal alloy nanoparticles are extensively developed topic in materials science. In order to increase the activity and durability physical properties such as composition of the alloys, structure and the size of nanoparticles are carefully selected. Most of the synthesis methods use organic surfactants, capping agents or high temperatures, consequently heating or cleaning treatment are necessary and therefore, the catalytic activity can be affected by undesirable adsorbed species. Nevertheless, among the various methods, electrodeposition is recognized as a simple and versatile method to prepare bimetallic surfaces. Several methods for PdNi alloy electrodeposition can be find in the literature such as: double-potential step electrodeposition technique from the solution containing $NiSO_4$, H_2PdCl_4 and Na_2SO_4 [23]; cathodic deposition from the solution containing $PdCl_2$, H_2SO_4, NH_4Cl and $NiCl_2$ using hydrogen

dynamic bubble template producing three-dimensional hierarchical pores of intercomnected dendrite walls [24]; electrodeposition in the presence of complexing agent, ethylenediamine [25,26]; electrodeposition from a ionic liquid as electrolyte [16,27]; physical vapour deposition which was used to obtain palladium-modified nickel foam material [19].

The aim of this work is to investigate the electrochemical behavior of electrodeposited Pd and PdNi coatings for the EOR in 1 M NaOH at room temperature. An attempt is made to estimate the difference in catalytic activity of binary coatings in comparison with the Pd coating toward EOR, to test the stability of PdNi coatings and their ability to recover activity loss. In addition, kinetic and mass transport properties of the electrodeposited coatings are examined.

Experimental

All experiments were carried out with an VoltaLab PGZ 402 (Radiometer Analytical, Lyon, France) at room temperature in three compartment electrochemical glass cells with Pt wire as the counter electrode and saturated calomel electrode (SCE) as the reference electrode. A mirror-like polished gold rotating disk electrode (d = 5 mm) prepared as described elsewhere [28] served as working electrode. All the solutions used were prepared with high purity UV water (Millipore, 18.2 MΩ cm resistivity) and *p.a.* grade chemicals (Merck). The electrolytes were purged with purified nitrogen prior to each experiment.

Electrodeposition of PdNi coating samples was achieved galvanostatically on the rotating Au disc electrode from the plating bath composed of 0.01 M $PdCl_2$ + 0.6 M $NiCl_2$ + 2 M NH_4Cl while pure Pd was electrodeposited from the bath containing 0.05 M $PdCl_2$ + 2 M NH_4Cl. All the conditions are the same as it was described in [29].

The electrochemically active surface area (ECSA) was estimated from the charge corresponding to the Pd-oxide reduction peak in 1 M NaOH by dividing obtained charge with the charge of 420 μC cm^{-2} (corresponding to the monolayer of Pd-oxide), in accordance with the previous reports [6,8,22]. The presented results are corrected for the ECSA.

Behavior of electrodeposited Pd and PdNi samples during the investigation of the EOR was recorded in the solution containing 1 M C_2H_5OH + 1 M NaOH by using CV and polarization measurements at 1000 rpm. For current density–time responses of EOR the potential was stepped from -800 mV to -400 mV.

Results and discussion

Electrochemical characterization of the electrodeposited samples

The CVs of the investigated binary coatings and pure Pd coating in 1 M NaOH are displayed in Fig. 1. Anodic linear sweep voltammetry (ALSV) analysis and the energy dispersive X-ray spectroscopy (EDS) were used for the determination of the alloy coatings composition giving following compositions: $Pd_{0.74}Ni_{0.26}$, $Pd_{0.50}Ni_{0.50}$ and $Pd_{0.28}Ni_{0.72}$ [29]. The CVs presented in Fig. 1 clearly indicate that the current densities for hydrogen adsorption-absorption/desorption and oxide formation and reduction are higher for PdNi samples than those recorded on the CV for pure Pd coating. Reduction of Pd-oxide on all catalysts creates a well-defined peak, but at different potentials. On PdNi coatings the peak maximum is shifted towards more negative potentials compared to pure Pd coating, which indicates a stronger adsorption of oxide species on the surface of bimetallic coatings due to the presence of Ni [8]. It was shown that the formation of a monolayer of the α-$Ni(OH)_2$ occurred in the potential region between -1000 mV and -700 mV, while at potentials more positive than 200 mV further oxidation of Ni(II) species into NiOOH occurs [30].

Hence, the formation and the reduction of $Ni(OH)_2$, as well as partial formation of the NiOOH increase the anodic current density at potentials more positive than 100 mV as is presented in Fig. 1. Also, these processes occurred simultaneously with the formation and reduction of Pd-oxide.

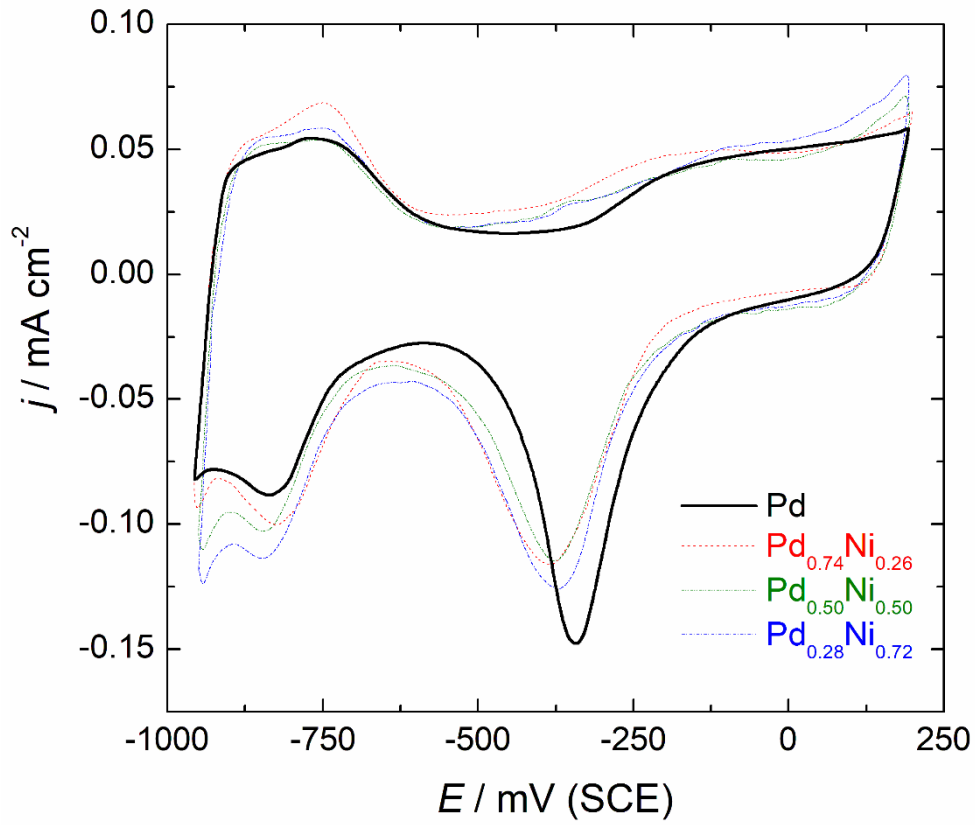

Figure 1. *CVs recorded with the scan rate 50 mV s^{-1}, 1000 rpm on Pd and PdNi coatings in 1 M NaOH.*

The EOR

The activity of the $Pd_{0.74}Ni_{0.26}$, $Pd_{0.50}Ni_{0.50}$, $Pd_{0.28}Ni_{0.72}$ and Pd coatings for the EOR in alkaline medium was investigated by the CV (Fig. 2). Considering electrochemical behavior of pure Pd during the EOR it was suggests that the carbonaceous intermediates can be strongly adsorbed on the Pd surface blocking the activity in the forward scan up to ~ -650 mV [31,32]. Since the Pd begins to adsorb OH^- species in the region of hydrogen adsorption [23], strongly adsorbed carbonaceous species can be oxidized, causing the increase of current density of the forward peak. Surface oxide formation block further adsorption of reactive species leading to decrease of current density of the forward peak. In the backward scan, the reduction of surface oxides enables ethanol adsorption at the free Pd surface, so that EOR current densities in the backward peak ascend. The peak in the backward scan could be assigned to the elimination of carbonaceous species that are not completely oxidized in the forward scan [23].

Among the CVs for the EOR at PdNi coating samples presented in Fig. 2, the current density increased with the increase of Pd content up to 74 at.%. Also, it seems that the small amount of Ni is sufficient to shift the reaction onset potential to more negative values since EOR on $Pd_{0.74}Ni_{0.26}$ starts ~50 mV earlier compared to the other binary coatings and ~100 mV compared to the Pd coating. It was demonstrated based on the ratio of the forward and the backward peak current density that the alloy surfaces were less poisoned than pure Pd coating [29]. Among them the $Pd_{0.74}Ni_{0.26}$ coating is the most poisoning tolerant. The role of Ni in binary coatings can be rationalized in following way: since Ni itself is not active for the EOR at the potentials relevant for

the practical application [33] the presence of Ni in the PdNi alloy enhance the EOR by increasing the presence of OH species at the electrode surface [6,8,17] leading to the shift of onset potential to more negative values and the increase of the current density, as observed in Fig. 2. Also, the presented results reveal better utilization of Pd on the surface of $Pd_{0.74}Ni_{0.26}$ coating due to appropriate surface morphology since more active sites are accessible to the EOR. It can be pointed out that improved catalytic activity of investigated binary coatings can be achieved through the optimization of the Ni content and appropriate surface morphology.

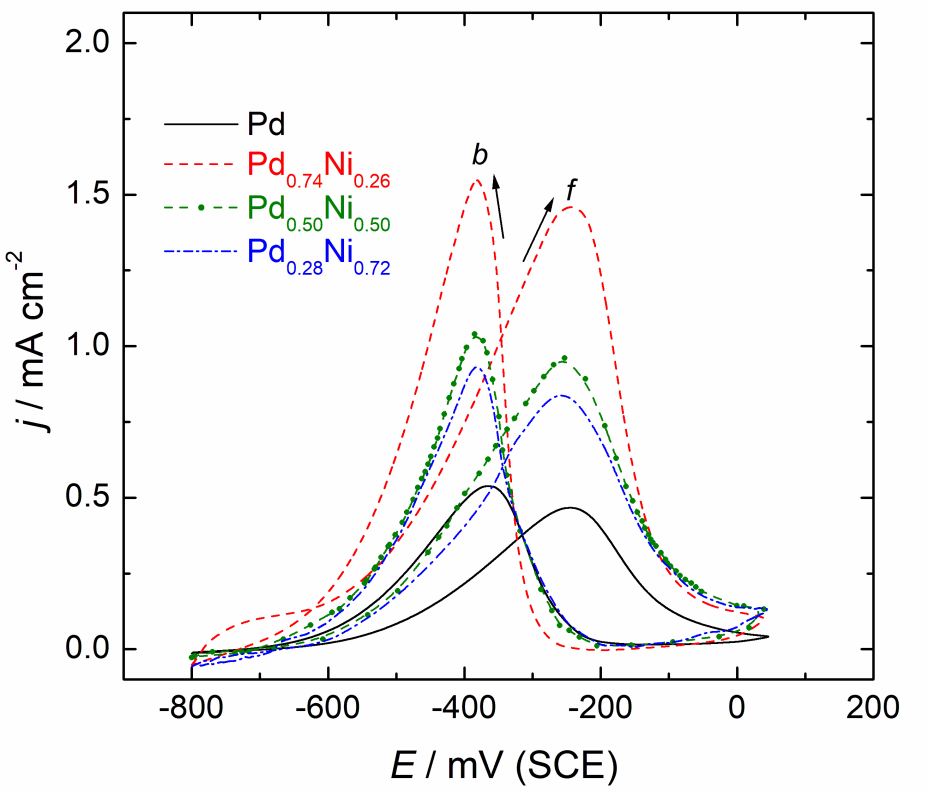

Figure 2. *CVs recorded with the scan rate 50 mV s^{-1}, 1000 rpm on Pd and PdNi coatings in 1 M NaOH + 1 M C_2H_5OH.*

Considering the literature, it can be stated that the best ratio of Pd and Ni for the EOR vary, depending on several factors as was explained in [29] whereby excess Ni decrease the activity for EOR due to the active surface blocking [6,35]. It can be found that carbon supported PdNi catalyst with atomic ratio of 40:60 synthesized by the simultaneous reduction method using $NaBH_4$ as reductant exhibits 2 times higher activity and better stability than does the Pd/C catalyst [34]. Also the optimized carbon supported PdNi catalyst synthesized through a modified solution phase-based nanocapsule method, with atomic ratio of 44:56 represents the promising anode catalyst for alkaline DEFCs giving 180 mV more negative EOR onset potential and the 33 times higher exchange current density than Pd/C [35]. Graphene supported PdNi catalyst prepared by chemical reduction method, with atomic ratio of 50:50 showed the lower onset potential on CV and better long-term stability on amperometric measurements of EOR in a series of investigated binary alloyed Ni_xPd_{100-x}/G catalysts [6].

Chronoamperometric technique is an effective method to evaluate the electrocatalytic activity and stability of catalyst materials. Figure 3 shows the typical current density–time responses of three PdNi coatings and pure Pd coating for the EOR at E = -400 mV. The oxidation current densities rapidly decrease in first ~100 s, likely due to the formation of intermediates and poisoning species

during the EOR. With the time, a pseudo-steady state is achieved. After a polarization of 1500 s, the investigated electrodes reached their steady-state current densities which are shown in the inset of Fig. 3 with respect to Pd content (at %). It can be seen that the current density of the EOR on $Pd_{0.74}Ni_{0.26}$ electrode is higher than those on other electrodes, as found above in the CV measurements.

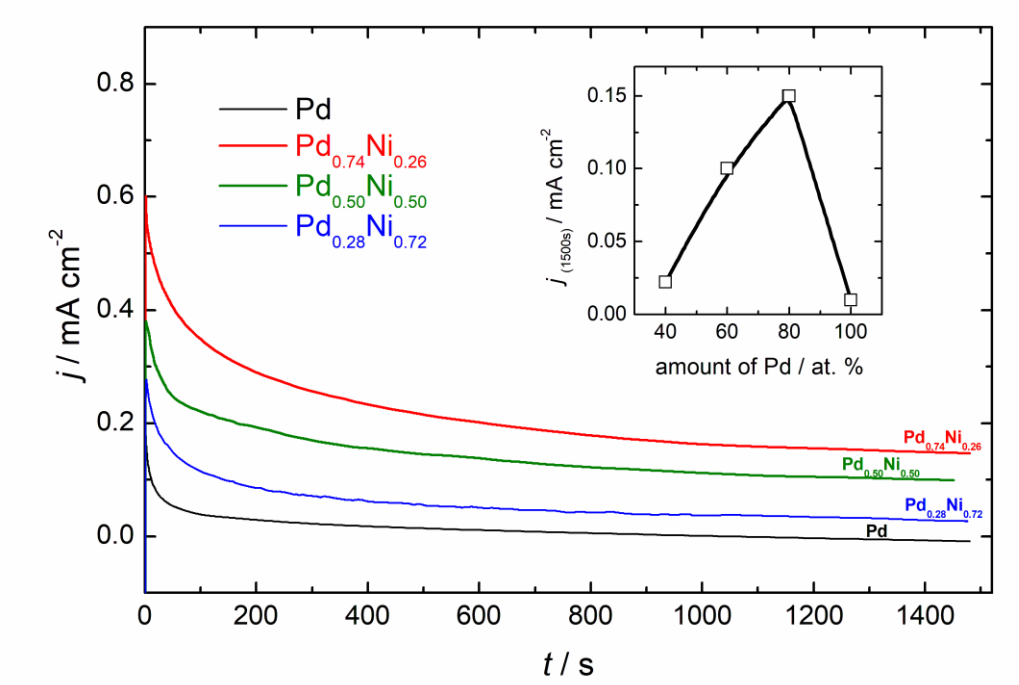

Figure 3. *Current density–time responses recorded on Pd and PdNi coatings in 1 M NaOH + 1 M C_2H_5OH at E = - 400 mV. 1000 rpm. Inset: current densities after 1500 s vs. at % Pd.*

Upon the end of the current-time transient, the investigated catalysts were subjected to the potential cycling. Figure 4 depicts the 1. and 10. cycles of $Pd_{0.74}Ni_{0.26}$ electrode as the representative ones. This PdNi coating shows reduced current densities at the beginning of cycling after CA with further increase of the activity during the cycling. The ability to recover activity loss demonstrates surface composition stability of investigated binary coatings. Hence, PdNi coatings showed enhanced electrocatalytic activity towards EOR which nominates this type of catalyst for possible practical application.

For the purpose of comparing the kinetic and mass transport properties of the investigated electrodes during ethanol oxidation, Tafel polarization analysis and the relation between the peak current density and the scan rate were provided. The Tafel plots are showed in Fig. 5. The slope of ~140 mV dec^{-1} for $Pd_{0.74}Ni_{0.26}$ is obtained for the potentials up to –600 mV, while ~160 mV dec^{-1} for $Pd_{0.50}Ni_{0.50}$, $Pd_{0.28}Ni_{0.72}$ and Pd are Tafel slops also obtained at the beginning of the peak in potential window up to ~ -550 mV. Lower Tafel slope indicate faster EOR charge-transfer kinetics. The results of the Tafel polarization study corroborate the findings of CV. Nearly the same values of Tafel plots were obtained on graphene supported NiPd binary catalysts [6], binary composite films of Pd and Ni on multiwalled carbon nanotubes (MWCNT) [36], carbon supported PdNi nanoparticles [35,37] and rather higher on PdNi nanoparticles supported on sulfonated MWCNT [38].

Figure 6 shows the CVs obtained at $Pd_{0.74}Ni_{0.26}$ catalyst in 1 M NaOH +1.0 M C_2H_5OH solution at different scan rates. The relation between the peak current density obtained from forward CV scan and $v^{0.5}$ of CV is shown in the inset. It can be seen that the oxidation potential and peak current density for ethanol oxidation become larger with the increasing of scan rate.

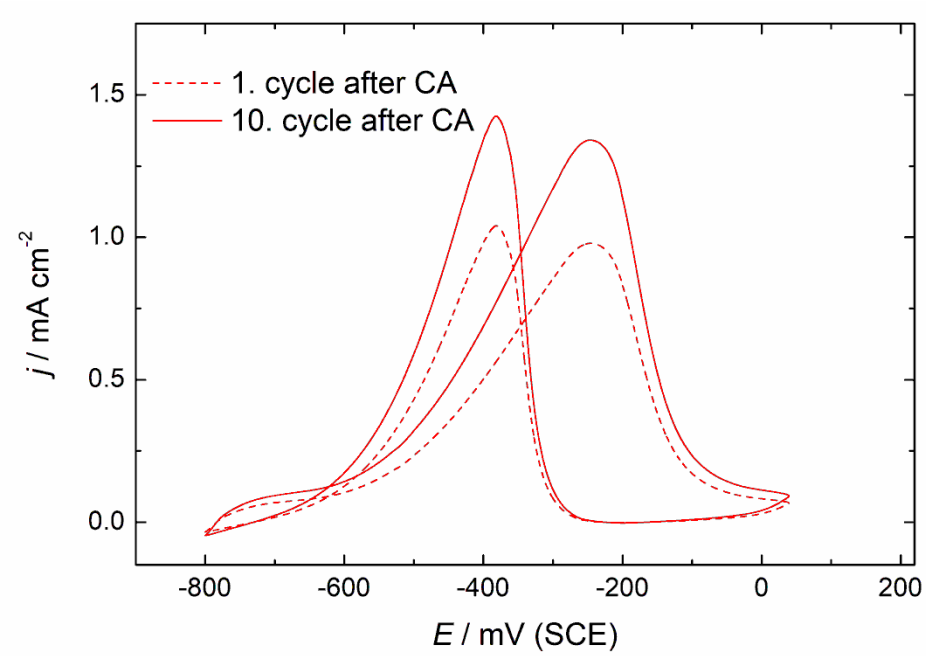

Figure 4. *CVs (1. and 10. cycle) recorded on $Pd_{0.74}Ni_{0.26}$ after CA in 1 M NaOH + 1 M C_2H_5OH. Scan rate 50 mV s^{-1}, RPM = 1000.*

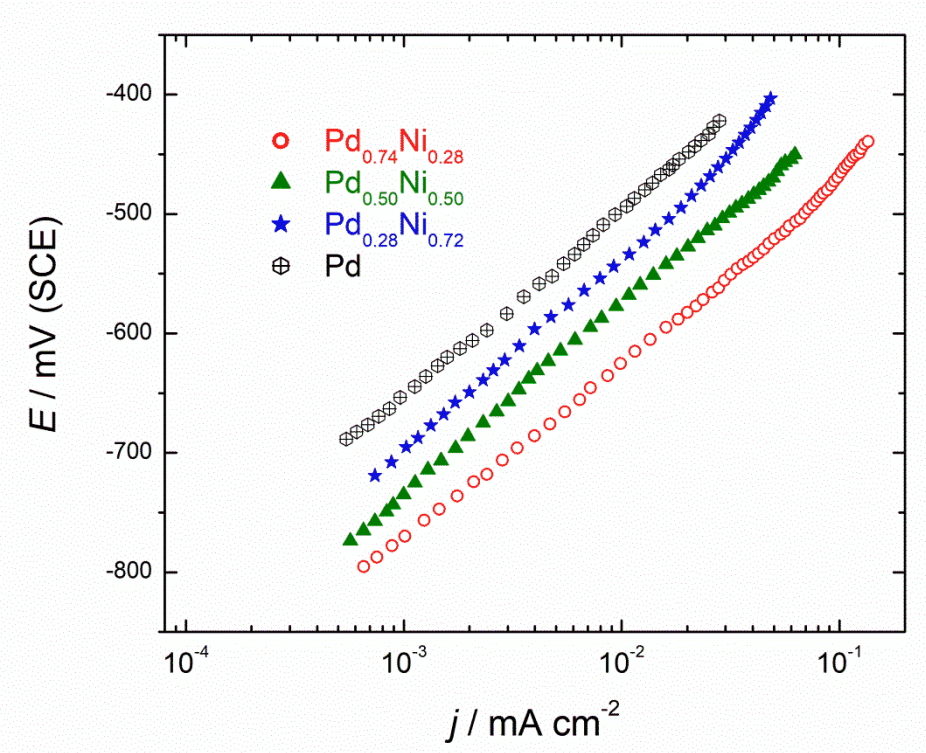

Figure 5. *Tafel responses recorded on Pd and PdNi coatings in 1 M NaOH + 1 M C_2H_5OH. Scan rate 1 mV s^{-1}, RPM = 1000.*

The peak current densities in the forward scan are linearly proportional to the square root of scan rates (Fig. 6a). Close inspection of Fig. 6a depict nonzero intercept of the peak current at zero scan rate suggesting that it not is a pure diffusion controlled process. Nonzero intercept could suggest the involvement of some type of surface interactions in examine reaction. Additionally, the peak potential in the forward scan (E_{pa}), increase with the increase of v, and a linear dependency can be obtained between E_{pa} and ln v, as shown in Fig. 6b. The same dependency was obtained on

pure Pd coating and binary coatings with higher content of Ni indicating that the oxidation of ethanol is an irreversible electrode process [6].

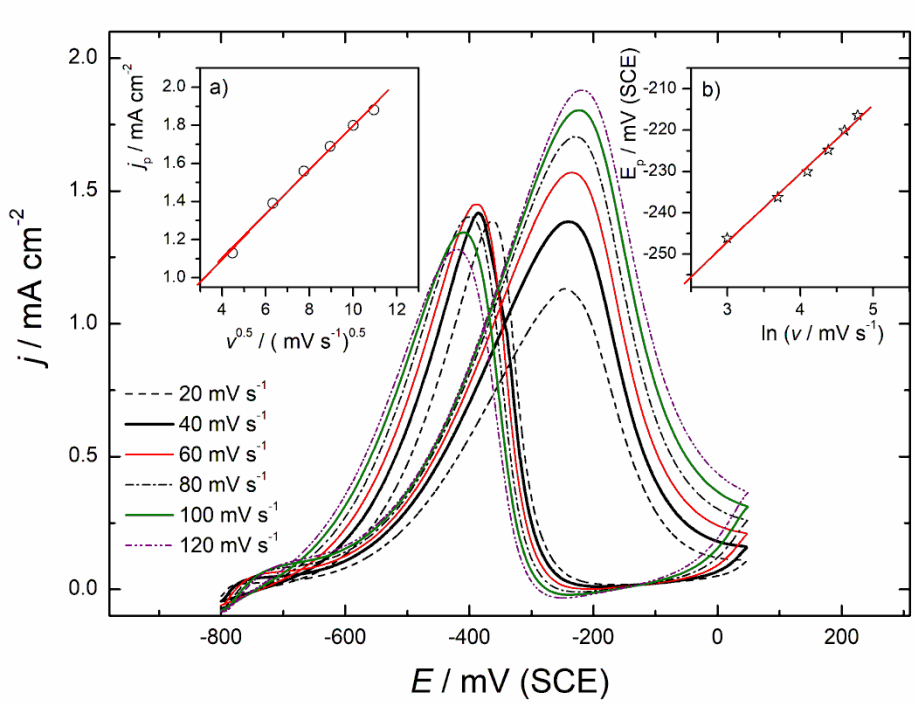

Figure 6. *CVs on $Pd_{0.74}Ni_{0.26}$ coating in 1 M KOH+ 1 M C_2H_5OH at various scan rates. Insets: plots current densities in the forward scan* vs. $v^{0.5}$ *(a) and peak potentials in forward scan* vs. *ln of scan rates (b).*

Conclusions

In summary, the coating samples obtained by simultaneous electrodeposition were tested for the EOR using CV, CA and quasi-steady state measurements and compare to pure Pd coating. The most active one was found to be $Pd_{0.74}Ni_{0.26}$ exhibiting also negatively shifted onset potential for the EOR. Kinetic and mass transport properties reveal lower Tafel slope obtained on $Pd_{0.74}Ni_{0.26}$ indicating faster EOR charge-transfer kinetics while the EOR is not a pure diffusion controlled process. Furthermore, it was shown that EOR is an irreversible electrode process on all examined coatings. It was pointing out that $Pd_{0.74}Ni_{0.26}$ coating is more efficient and the more poisoning tolerant than the other investigated coatings. Also, the ability to recover activity loss confirms the surface composition stability of investigated binary coatings.

Acknowledgements*: This work was financially supported by the Ministry of Education, Science and Technological Development of the Republic of Serbia, Contract No. H-172060.*

References

[1] E. Antolini, E. R. Gonzalez, *Journal of Power Sources* **195** (2010) 3431-3450.
[2] L. F. Dong, R. R. S. Gari, Z. Li, M. M. Craig, S. F. Hou, *Carbon* **48** (2010) 781-787.
[3] A. Brouzgou, A. Podias, P. Tsiakaras, *Journal of Applied Electrochemistry* **43** (2013) 119-136.
[4] S. Song, W. Zhou, Z. Liang, R. Cai, G. Sun, Q. Xin, V. Stergiopoulos, P. Tsiakaras, *Applied Catalysis B: Environmental* **55** (2005) 65-72.
[5] Y. Wang, S. Zou, W-B Cai, *Catalysts* **5** (2015) 1507-1534.
[6] M. S. Ahmed, S. Jeon, *ACS Catalysis* **4** (2014) 1830-1837.
[7] T. Maiyalagan, K. Scott, *Journal of Power Sources* **195** (2010) 5246–5251.
[8] M. D. Obradovic, Z. M. Stancic, U. C. Lacnjevac, V. V. Radmilovic, A. Gavrilovic-Wohlmuthere, V. R. Radmilovic, S. Lj. Gojkovic, *Applied Catalysis B: Environmental* **189** (2016) 110–118.

[9] C. Peng, Y. Hu, M. Liu, Y. Zheng, *Journal of Power Sources* **278** (2015) 69-75.
[10] K. Persson, A. Ersson, K. Jansson, N. Iverlund, S. Järås, *Journal of Catalysis* **231** (2005) 139-150.
[11] P. Mukherjee, P. Sarathi, K. Mandal, D. Bhattacharjee, S. Dasgupta, S. Kumar, *Electrochimica Acta* **154** (2015) 447–455.
[12] S. Fu, C. Zhu, D. Du, Y. Lin, *ACS Applied Materials and Interfaces* **7** (2015) 13842−13848.
[13] F.I. Pires, H.M. Villullas, *International Journal of Hydrogen Energy*, **37** (2012) 17052-17059.
[14] B. Cai, D. Wen, W. Liu, A-K. Herrmann, A. Benad, A. Eychmîller, *Angewandte Chemie* **54** (2015) 13101-13105.
[15] Y. Feng, D. Bin, B. Yan, Y. Du, T. Majima, W. Zhou, *Journal of Colloid and Interface Science* **493** (2017) 190-197.
[16] K. Ding, H. Yang, Y. Cao, C. Zheng, S. B. Rapole, Z. Guo, *Materials Chemistry and Physics **142** (2013) 403-411.*
[17] Q. Yi, Q. Chen, *Electrochimica Acta* **182** (2015) 96-103.
[18] M. Zhang, Z. Yan, J. Xie, *Electrochimica Acta* **77** (2012) 237-243.
[19] T. Mikolajczyk, M. Turemko, B. Pierozynski, *Journal of Electroanalytical Chemistry* **735** (2014) 32-35.
[20] W. Wang, Y. Yang, Y. Liu, Z. Zhang, W. Dong, Z. Lei, *Journal of Power Sources* **273** (2015) 631-637.
[21] B. Hammer, J.K. Nørskov, *Advances in Catalysis* **45** (2000) 71-129.
[22] A. Dutta, J. Datta, *Journal of Materials Chemistry A* **2** (2014) 3237-3250.
[23] C. Qiu, R. Shang, Y. Xie, Y. Bu, C. Li, H. Ma, *Materials Chemistry and Physics* **120** (2010) 323-330.
[24] R. Li, H. Mao, J. Zhang, T. Huang, A. Yu, *Journal of Power Sources* **241** (2013) 660-667.
[25] K. Kumar, H. Haridoss, S.K. Seshadri, *Surface and Coatings Technology* **202** (2008) 1764-1770.
[26] Q. Yi, F. Niu, L. Sun, *Fuel* **111** (2013) 88-95.
[27] H. Y. Huang, P. Y. Chen, *Talanta* **83** (2010) 379-385.
[28] J. Mirković, J. Lović, M. Avramov Ivić, D. Mijin, *Electrochimica Acta* **137** (2014) 705-713.
[29] J. D. Lović, V. D. Jović, *Journal of Solid State Electrochemistry* **21** (2017) 2433-2441.
[30] M. Grden, K. Klimek, A. Czerwinski, *Journal of Solid State Electrochemistry* **8** (2004) 390–397.
[31] L. P. R. Moraes, B. R. Matos, C. Radtke, E. I. Santiago, F. C. Fonseca, S. C. Amico, C. F. Malfatti, *International Journal of Hydrogen Energy* **41** (2016) 6457-6458.
[32] Z. Liu, X. Zhang, L. Hong, *Electrochemistry Communications* **11** (2009) 925-928.
[33] T. G. Nikiforova, O. A. Datskevich, V. V. Maleev, *Russian Journal of Applied Chemistry* **85** (2012) 1871-1878.
[34] S. Y. Shen, T. S. Zhao, J. B. Xu, Y. S. Li, *Journal of Power Sources* **195** (2010) 1001-1006.
[35] Z. Zhang, L. Xin, K. Sun, W. Li, *International Journal of Hydrogen Energy* **36** (2011) 12686-12697.
[36] R. N. Singh, A. Singh Anindita, *Carbon* **47** (2009) 271-278.
[37] A. Dutta, J. Datta, *Journal of Physical Chemistry* C **116** (2012) 25677−25688.
[38] T. Ramulifhoa, K. I. Ozoemenaa, R. M. Modibedia, C. J. Jafta, M. K. Mathe, *Electrochimica Acta* **59** (2012) 310-320.

J. Electrochem. Sci. Eng. **8(1)** (2018) 49-71; DOI: http://dx.doi.org/10.5599/jese.480

Open Access : : ISSN 1847-9286

www.jESE-online.org

Original scientific paper

In-depth component distribution in electrodeposited alloys and multilayers

László Péter[1,✉], Kálmán Vad[2], Attila Csik[2], Rocío Muñíz[3], Lara Lobo[3], Rosario Pereiro[3], Sašo Šturm[4], Kristina Žužek Rožman[4], György Molnár[5], Katalin Németh[1], Katalin Neuróhr[1], Krisztina Boros[1], Lajos Pogány[1], Imre Bakonyi[1]

[1]*Wigner Research Centre for Physics, Hungarian Academy of Sciences, Konkoly-Thege út 29-33, 1121 Budapest, Hungary*

[2]*Institute of Nuclear Research of the Hungarian Academy of Sciences, Bem tér 18/c, 4026 Debrecen, Hungary*

[3]*Department of Physical and Analytical Chemistry, University of Oviedo, Julián Clavería 8, 33006 Oviedo, Spain*

[4]*Jožef Stefan Institute, Jamova 39, 1000 Ljubljana, Slovenia*

[5]*Institute of Technical Physics and Materials Science, Centre for Energy Research, Hungarian Academy of Sciences, Konkoly-Thege út 29-33, 1121 Budapest, Hungary*

Corresponding authors E-mail: ✉peter.laszlo@wigner.mta.hu; Tel.: +36-1-392-2222, ext 3614; Fax: +36-1-392-2768

Received: November 30, 2017; Accepted: January 8, 2018

Abstract

It is shown in this overview that modern composition depth profiling methods like secondary neutral mass spectroscopy (SNMS) and glow-discharge – time-of-flight mass spectrometry (GD-ToFMS) can be used to gain highly specific composition depth profile information on electrodeposited alloys. In some cases, cross-sectional transmission electron microscopy was also used for gaining complementary information; nevertheless, the basic component distribution derived with each method exhibited the same basic features. When applying the reverse sputtering direction to SNMS analysis, the near-substrate composition evolution can be revealed with unprecedented precision. Results are presented for several specific cases of electrodeposited alloys and mulitlayers. It is shown that upon d.c. plating from an unstirred solution, the preferentially deposited metal accumulates in the near-substrate zone, and the steady-state alloy composition sets in at about 150-200 nm deposit thickness only. If there is more than one preferentially deposited metal in the alloy, the accumulation zones of these metals occur in the order of the deposition preference. This accumulation zone can be eliminated by well-controlled hydrodynamic conditions (like the application of rotating disc electrodes) or by pulse

plating where the systematic decrease in the duty cycle provides a gradual transition from a graded to a uniform composition depth profile. The application of composition depth profile measurements enabled detecting the coincidence in the occurrence of some components in the deposits down to the impurity level. This was exemplified by the GD-ToFMS measurements of Ni-Cu/Cu multilayers where all detected impurities accumulated in the Cu layer. The wealth of information obtained by these methods provides a much more detailed picture than the results normally obtained with bulk analysis through conventional integral depth profiling and help in the elucidation of the side reactions taking place during the plating processes.

Keywords
Alloy formation; near-substrate composition modulation; hydrodynamic conditions; component distribution correlations

Introduction

Electrodeposited metal coatings have been widely used for the corrosion protection as well as for the improvement of the appearance of the coated objects for more than a century. For both above mentioned purposes, the mean composition of the coating, the even lateral component distribution within the coating and the quality of the final surface (*e.g.,* roughness and passivity) are the crucial parameters.

Nowadays, electroplating is much more than a workhorse of the coating industry. Electrodeposition has found its role in the preparation of various nanostructures [1-9], whose functionality strongly depends on, e.g., the component distribution of the electroplated material also at the nanometer scale. Inhomogeneities can influence various physical and chemical parameters such as adhesion of the coating, strain (that impacts hardness and yield strength), electrical resistivity, saturation magnetization, magnetostriction and hence the coercive field, band gap (of semiconductors), catalytic properties etc. Therefore, the compliance of the component distribution of a coating to a predefined pattern is a prerequisite for achieving the desired functionality.

In parallel to the emergence of electrochemical nanotechnologies, local composition analysis methods working at the nanoscale as well as the composition depth profile methods have undergone a significant development. Concerning techniques that can be used for planar surfaces, most of the *non-destructive composition depth profiling methods* (such as X-ray and neutron reflectometry, ellipsometry and angle-resolved X-ray photoelectron spectroscopy /ARXPS/) are sensitive to a narrow range beneath the sample surface only (typically at most a few tens of nanometers). Rutheford backscattering spectroscopy is capable of detecting the in-depth component distribution at a larger depth, nevertheless the depth resolution is limited. The common disadvantages of these methods (except for ARXPS) are that they require a preliminary assumption on the component/phase distribution that makes the model boundary conditions, a large number of input parameters necessary for the evaluation of the measurements and the lack of direct chemical information.

The family of the *destructive composition depth profile analysis methods* is also quite complex, as presented in Figure 1. All of the methods shown in Figure 1 yield direct composition information, a few of them (Auger/XPS techniques) being also sensitive to the oxidation state of the elements. Although the destructive nature of these methods leads to at least a partial consumption of the samples, all can be used without a preliminary assumption on either the sample structure or composition.

Historically, the spontaneous variation of the alloy composition during d.c. plating was detected as the change of the average composition as a function of the thickness [10-14]. Although this procedure is well indicative of a composition change, it is an integral method, which also means that its sensitivity to either local effects or subtle changes is very little. In contrast to integral methods, methods based on a local analysis exhibit a much higher sensitivity. This is true regardless of whether the information obtained either from the deposit itself (like in transmission electron microscopy /TEM/ energy dispersive X-ray spectroscopy /EDXS/) or from the composition of the sputtered material (with secondary neutral mass spectrometry /SNMS/ and with glow discharge – time-of-flight mass spectrometry /GD-ToFMS/). This is particularly important or even indispensable when a multilayer is deposited because a bulk analysis cannot reveal practically any detail of the component distribution.

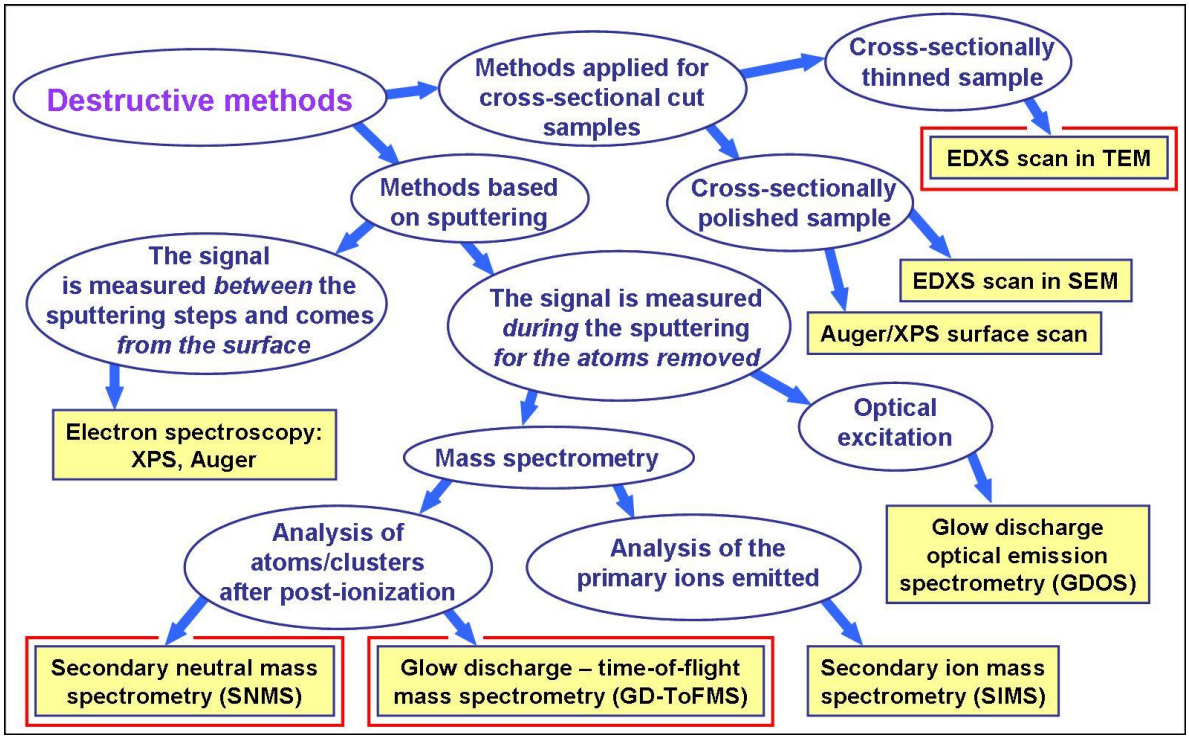

Figure 1. *Organization chart of destructive composition depth profile analysis methods. Methods used in the studies to be described later are labeled with a red square. Key to acronyms not resolved in the figure: EDXS: energy-dispersive X-ray spectroscopy; TEM: transmission electron microscopy; SEM: scanning electron microscopy; XPS: X-ray photoelectron spectroscopy*

The goal of this study was twofold: (i) to establish general trends that serve as guidelines concerning the alloy composition change in the growth direction during the plating process; and (ii) to analyze the component distribution in two-pulse-plated multilayers, including major components and impurities. It was our intention to use the most advanced composition depth profiling methods and also to confront their results with each other for obtaining a detailed picture on the phenomena studied and, also, for comparing the peculiarities of some specific methods.

Experimental

Materials and chemicals

Plating baths were made of analytical grade chemicals. Purified water with 18 MΩcm resistivity (ELGA Purelab R7) was used in each case for the preparation of the solutions. When the solution to

be used contained an oxidation-sensitive component (like Fe^{2+}), the solution was freshly prepared every day. A new portion of bath was used in every experiment. A sacrificial anode was typically a sheet or a wire spiral made of the most noble metallic component to be deposited in order to avoid a spontaneous cementation process. Since the sample studies were obtained with a large variety of baths, the solution components will be given in the sections where a specific group of deposit is reported.

Substrate

Samples were deposited onto Si wafers that were pre-coated by evaporation. The Si(100) wafers with approximately 3 nm root-mean-square roughness were cleaned but the native oxide layer was not removed. The evaporated coating consisted of a 5-nm chromium adhesion layer and a 20-nm copper conducting layer.

Electrodeposition apparatus

The majority of the electrodeposition experiments were carried out in a 50-ml volume Plexigrass® cell [15] which is shown in Figure 2a. The cathode was fixed in an upward-facing position to the bottom of the cell with a recess. In this cell, the solution was stagnant, and the even current distribution was provided by the recess and the parallel anode/cathode arrangement. The surface area was nominally 8 mm x 20 mm that might be a bit lower due to the compression of the gasket between the body of the cell and the cathode. The actual surface area of the deposit was measured after the removal of the cathode.

A few experiments were also performed with a home-built rotating disc electrode (Figure 2b). In these experiments, a 1-inch diameter pre-coated silicon wafer was fixed to a rotating PTFE cylinder of the same diameter. The electrical connection to the metallic coating of the wafer was provided with two clamps which also served to hold the wafer at the bottom surface of the electrode holder. The stainless-steel clamps were electrically sealed on the sides, hence minimizing the current passing elsewhere than through the wafer coating. The rotation rate of this electrode was less than 350 rpm. The counter electrode was a metal spiral at the bottom of the cell whose material was chosen according to the same principle as for the other cell.

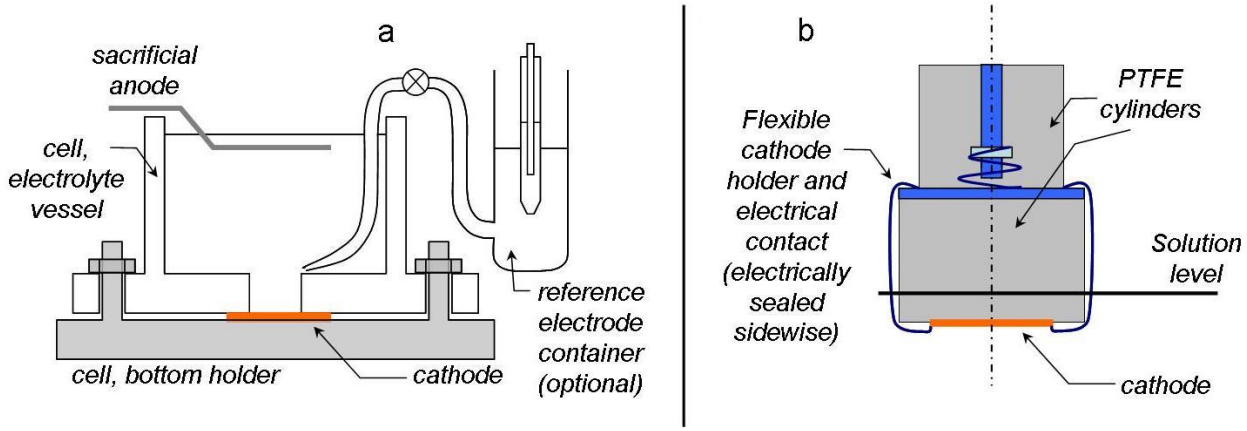

***Figure 2. a** - Structure of the cell for experiments with a stagnant solution (after Ref. 15).*
***b** - Construction of the rotating disc electrode for experiments with controlled hydrodynamics.*

The majority of the d.c.-plated samples were prepared with galvanostatic control; therefore, a reference electrode was only seldom used for checking the cathode potential variation during the deposition. Multilayered samples were deposited in a mixed G/P deposition mode [16] where the

less and more noble metal layers were produced during the constant-current (G) and the constant-potential (P) pulse, respectively. The more noble metal (*e.g.* Cu) was deposited with the limiting-current conditions, while the ratio of currents during the G and P pulses was used for the estimation of the deposit composition prepared during the G pulse (*e.g.* Ni_xCu_y). As power source for the sample preparation, three potentiostat/galvanostat units were used, all of them capable of operating without a pause between the pulses even during the G/P pulse sequence (Electroflex EF453, IviumStat, Ivium CompactStat).

Sample preparation for in-depth composition analysis

For SNMS depth profile analysis, samples were peeled off from the substrate. In order to carry out this process and to obtain a self-supporting sample with a sufficient mechanical strength, the deposition of the sample of interest was followed by the electrodeposition of at least one additional layer. After the deposition of the layer of interest onto the Si/Cr/Cu substrate, the solution was changed without disassembling the cell, and a Ni plating bath was used to obtain a Ni layer of at least 3 micrometer thickness. In some cases, especially when the deposit of interest was rich in Ni, a zinc interlayer was also deposited before the sample was finally covered with the nickel supporting layer. This made it possible to find the boundary of the layer of interest easily. After the coating process, the back side of the Si wafer was scratched and then broken by bending it, the sample being always at the concave side where it could not be torn apart. Then, the sample was gently separated from the Si wafer. The separation took place at the weakest interface, which was the Si/Cr boundary in the case of Si/Cr/Cu substrates. Further details of the process can be found elsewhere [17-20]. This procedure led to samples where the sputtering could be started from the substrate side of the sample (reverse sputtering direction), and the initial roughness at the beginning of the sputtering process was essentially the same as that of the Si wafer prior to the coating process.

For the GD-ToFMS study [21], the sample remained on the Si substrate and the deposit could be analyzed as it was obtained after the electrodeposition procedure. In this case, the sputtering direction was the conventional one; i.e., it started at the surface where the deposit formation finished. As the sample is deposited onto a Si substrate and it is used for sealing the discharge chamber, the reverse sputtering arrangement could not be applied with this method.

TEM specimens were initially prepared from a pair of delaminated electrodeposited films, which were glued together and inserted between Si wafer dummies. Discs with 3 mm diameter were cut from the central area of these bulk specimens, mechanically ground to a final thickness of 20 μm and ion-milled using 4-keV Ar^+ to achieve thin, electron-transmissive areas located in the film regions. Then, the TEM specimens were further ion-milled at a low energy of 500 eV and an incident angle of 6° for 30 minutes to remove all contamination.

Analysis instruments

SNMS depth profile analysis of the samples was performed with an INA-X type instrument (SPECS GmbH, Berlin, Germany) in direct bombardment mode by using Ar^+ ions with a fairly low energy for sputtering (typically with $E[Ar^+]$= 350 eV). The erosion area was confined to a circle of 2 to 3 mm diameter by means of Ta masks. The lateral homogeneity of the ion bombardment was checked by profilometric analysis of the craters sputtered.

A pulsed radiofrequency GD-ToFMS instrument (Horiba Scientific, France) was also used for depth profiling of some samples. The ion source was a copper-based 4 mm diameter anode with a 20 mm long flow tube. The sample was placed horizontally and rf power was supplied through the back of the sample. A quadrupole filter was placed just after the extraction cone, allowing

attenuation of the signal of up to four ion types of different masses in order to reduce the overload of the detector. ToFMS extraction frequency was set to 30 KHz, which made it possible to obtain mass spectra in every 33 µs. Data acquisition periods of 0.58 s were averaged for obtaining one data point in the depth profile. After the initial argon flush period, at 160 Pa pressure and with 30 W of power, 1 ms pulse width and 25 % duty cycle were selected for sample analysis.

For both sputtering-based analysis methods, the transformation of the *intensity vs. time* function to the *mole fraction vs. depth* function was carried out with a standard multi-matrix calibration procedure. The sputtering rate of the samples was measured with the help of a profilometer.

The TEM investigation was performed by a JEOL JEM-ARM200F instrument, using the cold field emission source, equipped with an EDXS system (Centurio 100 mm^2, JEOL). The probe size for scanning TEM (STEM) imaging was set to 0.1 nm, with a current of 20 pA and a convergence semi-angle of 24 mrad. STEM images were acquired in a so-called bright-field (BF) and a high-angle annular dark-field (HAADF) mode, respectively. The EDXS spectrum images were recorded with a lateral probe size of 0.2 nm, under continuous scanning mode with a pixel dwell time of 25 microseconds and by using probe currents of 250 pA.

Results and discussion

Composition depth profile of d.c.-plated Ni-Cd alloys obtained from a stagnant solution

During the study of the formation of binary alloys, first the composition depth profile of electroplated Ni-Cd alloys is analyzed where Cd is a minority component of the alloy. Nickel alloys have the advantage in such investigations that Ni exhibits a relatively small exchange current density, which makes its deposition quite hindered. This prevents nickel from developing dendrites in a wide range of current density. As opposed to metals having a high exchange current density (like Cu, Ag or Bi), the increment of the surface roughness of Ni with increasing deposit thickness is slow. The limited roughening, together with the favorable mechanical properties of nickel, makes it an ideal major component for depth profiling studies of alloy formation.

Figure 3 summarizes the composition depth profile information obtained for various Ni-Cd alloys. Samples were obtained from a Watts-type bath (0.85 mol dm^3 $NiSO_4$, 0.15 mol dm^{-3} $NiCl_2$, 0.4 mol dm^{-3} H_3BO_3; pH 2.5) doped with the $CdSO_4$ (3–30 mmol dm^{-3}) [19]. The current density that was used for the deposition of these samples (-19.5 mA cm^{-2}) was much above the limiting current density of the Cd deposition from a Ni-free solution for all Cd^{2+} concentrations used. This means that the Cd deposition can be regarded as a diffusion-limited deposition process where the Ni deposition absorbs the current that cannot be covered by the transport of the Cd^{2+} ions.

Figure 3(a) shows the near-substrate quantitative composition depth profile of the main components. Cr and Cu signals come from the substrate layers that were detached from the Si wafer. The good resolution of these layers indicates that the sample detachment from the substrate did not cause any significant damage to the sample. The decay of the Cu mole fraction to the half of its maximum is approximately at the depth that is the sum of the nominal thickness of the Cr and Cu layers (5 nm + 20 nm, respectively). It can be well seen that the mole fraction of Cd is about four times larger in the near-substrate zone than in the bulk of the sample.

The Cd accumulation is due to its preferred deposition, while the Cd concentration decay is explained with the depletion of the solution layer near the cathode surface with respect to the fast-reacting Cd^{2+} ions. The decay of the mole fraction of the component with high relative deposition preference is the consequence of the interplay of the large reaction rate and the depletion of the bath with respect to this component in the unstirred solution.

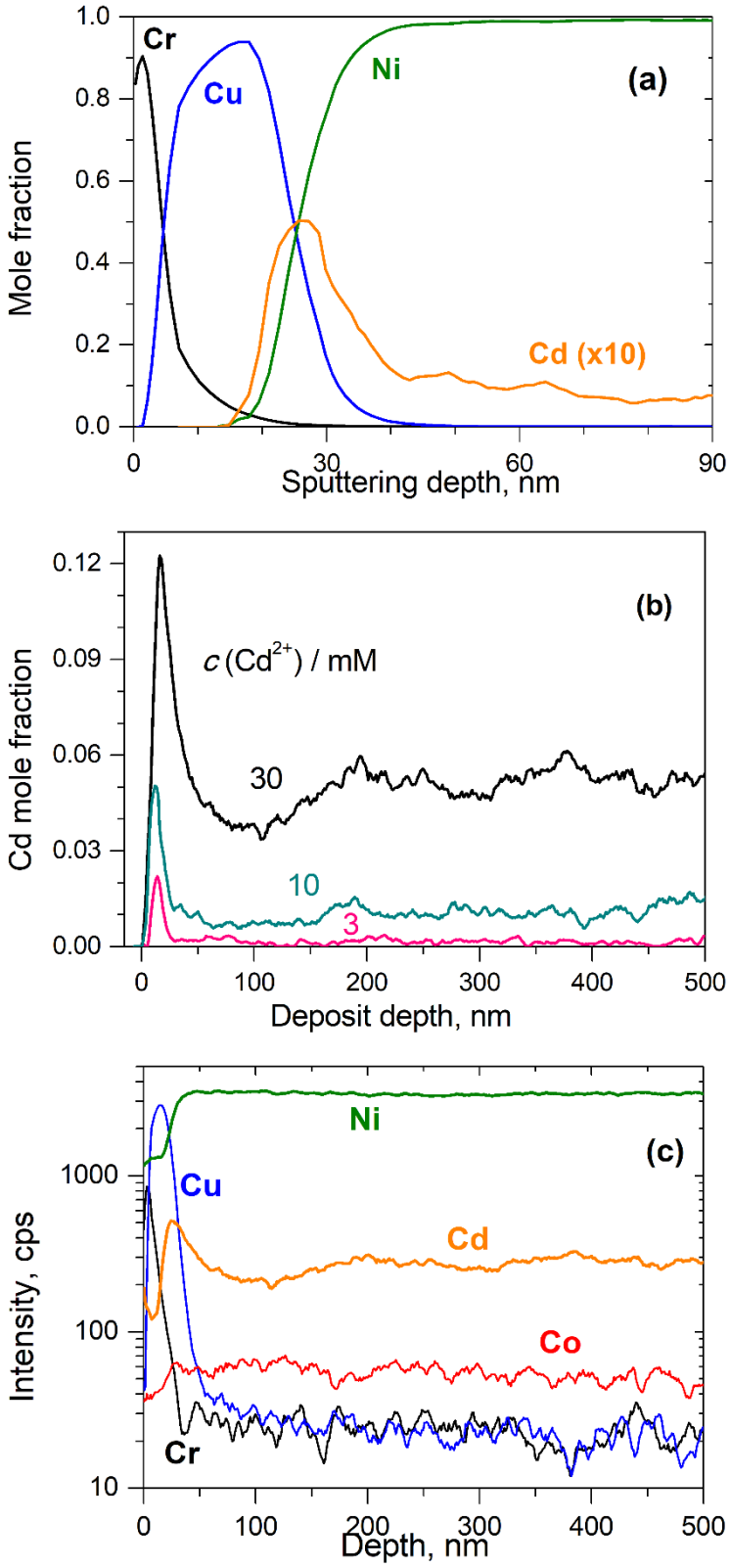

Figure 3. (a) *Reverse SNMS composition depth profile of a Si/Cr/Cu//Ni-Cd sample;* c(Cd^{2+}) = 10 mmol dm^{-3}. ***(b)*** *Comparison of the Cd mole fractions from the reverse depth profile measurements of alloys obtained with different* Cd^{2+} *concentrations. The depth scale is corrected for the substrate thickness.* ***(c)*** *Raw SNMS measurement data indicating the reverse depth profile with the signal intensities of all elements detected. In this experiments, the* Cd^{2+} *ion concentration was* c(Cd^{2+}) = 30 mmol dm^{-3}.

Figure 3(b) indicates that the trend of the accumulation of the metal with higher deposition preference near the substrate is the same for a wide range of the concentration of its precursor

cation. However, some quantitative differences of the depth profile functions can also be observed. The relative accumulation of Cd near the substrate (calculated as the ratio of the peak mole fraction and the mean mole fraction in the bulk) depends on the concentration. The smaller the Cd^{2+}concentration, the larger its relative accumulation, varying from 14 to 2.4 as $c(Cd^{2+})$ increases from 3 to 30 mmol dm^{-3}. At the same time, the decay depth of the concentration maximum increases with the Cd concentration (from 35 nm to about 110 nm as $c(Cd^{2+})$ increases by an order of magnitude from 3 to 30 mmol dm^{-3}).

The display of the data on a logarithmic intensity scale makes it possible to present the composition depth profile of all important components in a single plot, as shown in Figure 3(c). The fast decay of the signal of the substrate components, Cr and Cu, to their background level is an indication of (i) the low surface roughness of samples peeled off from the Si substrate; (ii) the lack of the redeposition of these components; and (iii) the complete removal of the products from the chamber after the sputtering of the corresponding layers finished. It can also be seen that Co appears with the occurrence of the Ni-rich layer. This is because Co is a very common impurity in Ni compounds and is deposited preferentially besides Ni. Therefore, a small concentration of Co in the precursor materials manifests itself as a Co signal in the SNMS measurement. It is worthwhile noting that the Co intensity increases to its steady-state value in the same depth range in the near-substrate zone where the Ni signal grows to its plateau value.

Although it is very tempting to treat the formation of dilute alloys merely by the mass transport effect of the precursor ions, the data for the Ni-Cd system also show that the phenomenon is by far not that simple. For instance, it can be seen from the quantitative analysis that the Cd mole fraction is not linearly proportional to the Cd^{2+} concentration (see Figure 3(b)), although the mass transport-based contemplation would rationalize this view. Besides the mass transport, various other factors that are difficult to treat simultaneously should be taken into account; i.e., the change in the deposition efficiency due to the alloy formation because of the impact of the alloying element on the hydrogen evolution overvoltage, structural effects during alloy formation etc. [22-24]. An earlier study showed that Co as a minor component beside Ni accumulates in the near-substrate zone in the same manner as Cd does [19]. However, due to the formation of various structurally incoherent phases (with the most likely composition of CdNi and Cd_5Ni [23,25-27]), the Ni-Cd system is not suitable for a depth profiling study in a wide concentration range.

Comparison of d.c. plating and pulse plating: Ni-Fe alloys obtained from a stagnant solution

The Ni-Fe system enables studying the composition change during codeposition in a wide concentration range because the structural incoherency does not prevent the formation of a compact deposit. Iron is codeposited with nickel with the so-called anomalous codeposition mode [28-33], which means a high deposition preference of Fe^{2+} ions. Therefore, the baths that can be used for the deposition of Ni-Fe alloys are usually fairly dilute for Fe^{2+} as compared to Ni^{2+}. In the present study, the following solution concentrations were applied [20]: 0.55 mol dm^{-3} $NiSO_4$, 0.005-0.1 mol dm^{-3} $FeSO_4$, 0.3 mol dm^{-3} Na_2SO_4 (supporting electrolyte), 0.1 mol dm^{-3} H_3BO_3 (buffering agent), 0.2 g dm^{-3} saccharin (stress reliever) and 0.03 g dm^3 sodium dodecylsulfate (wetting agent).

Typical reverse composition depth profile curves obtained for Ni-Fe alloys are shown in Figure 4, for both galvanostatic and potentiostatic deposition modes. It is obvious from the measurements presented in Figure 4 that the enrichment of the preferentially deposited metal (here, Fe) in the near-substrate zone is not the consequence of the choice of the regulated electrical parameter, but

it is a general feature of the Fe-Ni codeposition. This statement is well in accord with the reason of the enrichment as described above; i.e., it is related to the solution depletion, whichever deposition mode leads to the consumption of the precursor ions. It is also to be noted that the change in the deposition potential during the galvanostatic deposition or the change in the current density during the potentiostatic deposition is insignificant and cannot be related to the composition change.

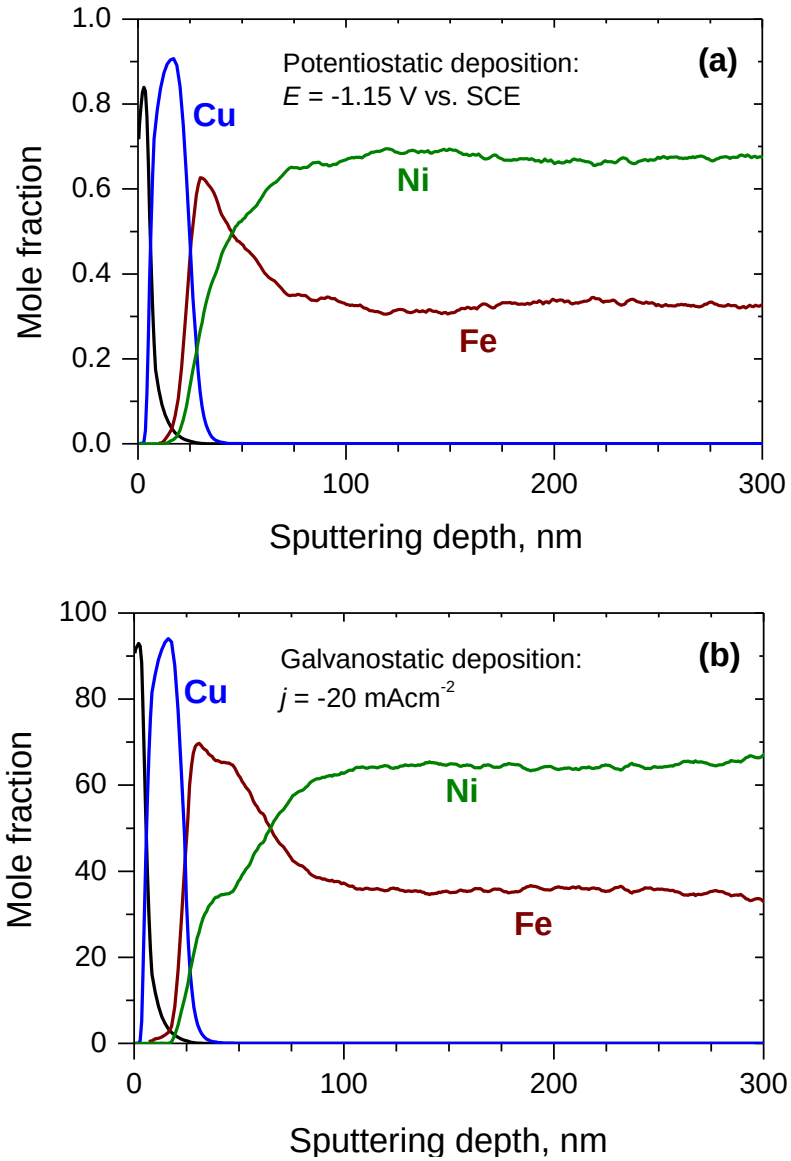

Figure 4. *Reverse SNMS composition depth profile of two Si/Cr/Cu//Ni-Fe samples; c(Fe^{2+}) = 45 mmol dm^{-3} for both specimens.* ***(a)*** *potentiostatic deposition,* ***(b)*** *galvanostatic deposition. In both graphs, the unlabeled black line refers to Cr.*

When pulse plating is applied, the composition depth profile function is nearly flat [20]. The small near-substrate composition transient can be minimized by decreasing the duty cycle. This provides that all circumstances, especially the electrolyte concentrations in the close vicinity of the substrate, recover to the same value as in the bulk solution by the start of the next deposition pulse. Therefore, the material deposited during each current pulse will be identical in composition. The lower the concentration of the Fe^{2+} ions in the solution, the smaller the duty cycle has to be in order to achieve the flat composition depth profile [20]. This is well understood since the smaller the composition of the ions of the preferentially deposited metal, the more the deposition approaches the diffusion-limited character (where the surface concentration of the reacting ions becomes zero). For the same

reason, the higher the on-time current density, the smaller the duty cycle has to be in order to achieve a flat composition depth profile. Although the above trends are well established, no quantitative description is available at the time being for anticipating the necessary duty cycle range for suppressing the initial composition change below a particular predefined limit. Figure 5 presents the summary of the data obtained for a number of pulse-plated samples.

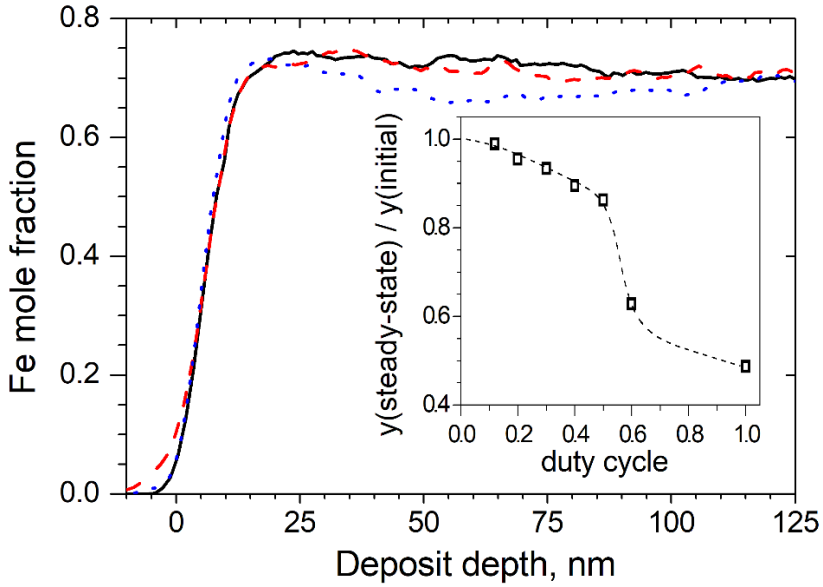

Figure 5. *Reverse SNMS composition depth profile of three pulse-plated Si/Cr/Cu//Ni-Fe samples. Deposition conditions: c(Fe^{2+}) = 45 mmol dm^{-3}, t_{ON}=0.1 s, t_{OFF} = 0.4 s; j_{ON} = -26.7, -20 and -13.3 mA cm^{-2} for the solid black, dashed red and dotted blue curves, respectively. Data were corrected for the substrate thickness and Fe mole fractions are only displayed for the sake of simplicity.* ***Inset:*** *Dependence of the ratio of steady-state and initial Fe mole fractions on the duty cycle for j_{ON} = -13.3 mA cm^{-2} (other deposition conditions are the same as for the main graph).*

Composition depth profile of d.c.-plated ternary Ni-Co-Fe alloys obtained from a stagnant solution

For binary alloys, it was clear that the metal with high deposition preference accumulates near the substrate. For a ternary alloy, an order of deposition preference can be deducted from the composition data of d.c. deposits. For iron-group metal alloys, this deposition preference is as follows: Fe>Co>Ni [34-36]. It is an open question how the order of the deposition preferences affects the composition evolution in the near-substrate zone. In this study, the solution contained 0.2 mol dm^{-3} $NiSO_4$, 0.075 mol dm^{-3} $CoSO_4$, 0.025 mol dm^{-3} $FeSO_4$, 0.4 mol dm^{-3} H_3BO_3, 0.03 g dm^{-3} sodium dodecylsulfate and 0.2 g dm^{-3} saccharin, while the pH was set to 2.8 with sulfuric acid. The order of the concentration of the metal sulfates is the opposite as the deposition preference. This provides that the mole fractions in the deposit have comparable orders of magnitude. When sodium citrate was also added to the bath, its concentration was 0.2 mol dm^{-3}, and the pH of the bath was 5.5 (which required no adjustment). Some composition depth profile data for the near-substrate zone of electrodeposited Ni-Co-Fe system are also available elsewhere [18,37], but these data are in contradiction to the long-range *composition vs. thickness* functions published in some other studies (e.g, Fig 5 of Ref. [38]).

Figure 6 presents the comparison of the reverse SNMS depth profile of two samples, deposited from a bath either without (Figure 6(a)) or with (Figure 6(b)) sodium citrate as complexing agent. In both measurements, the layer structure of the components originating from the substrate can be well seen, so much that the Cu mole fraction during the sputtering of the Cu layer achieves 1. This

indicates that the preparation of the samples led to undamaged specimens with intact Cr and Cu layers remaining on the deposit upon the removal from the Si wafer. Otherwise, the signals of the substrate layers and the deposit would smear out, strongly diminishing the apparent sharpness of the interfaces. The successful sample preparation also means that all differences found in the spectra are an inherent feature of the deposits and cannot be attributed to artefacts.

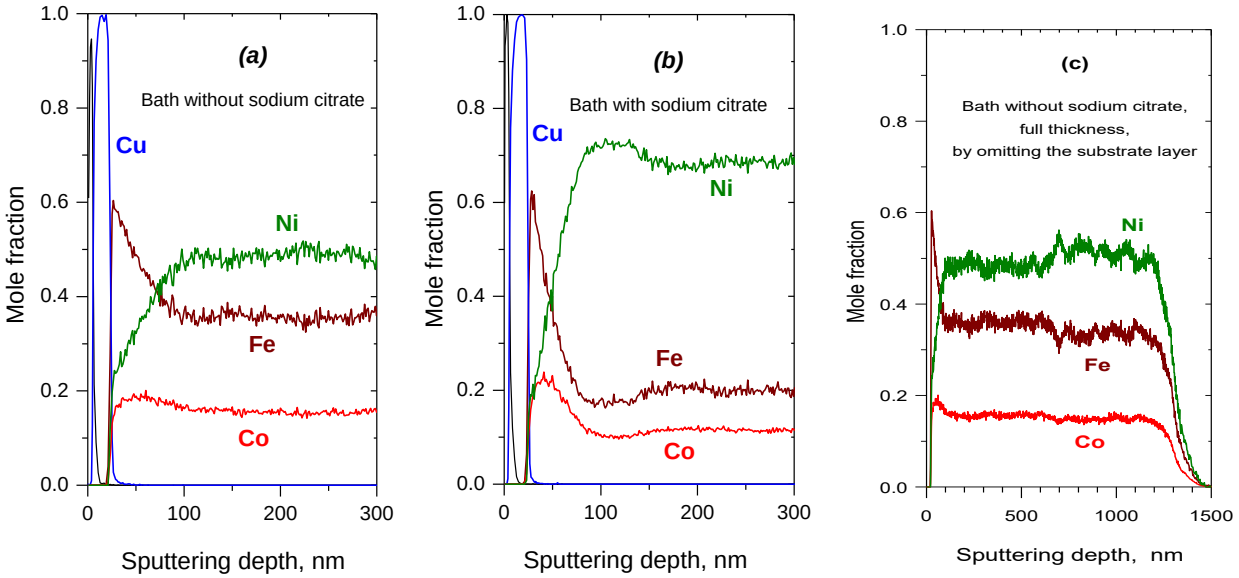

Figure 6. *Reverse SNMS composition depth profile of two d.c.-plated Si/Cr/Cu//Ni-Co-Fe samples with a current density j = -12 mA cm^{-2}. (a) No sodium citrate, pH 2.8; (b) c(Na_3Cit) = 0.2 mol dm^{-3}, pH 5.5. (c) Same profile as for (a) at the full depth scale.*

The scheme of the composition change is the same in the spectra of both d.c.-plated Ni-Co-Fe deposits. Namely, the deposition starts with an iron-rich material with an Fe mole fraction of about 0.6, and the Fe mole fraction starts to decay immediately. The sharpness of the Fe peak at the substrate/deposit boundary is determined by the experimental transient during the SNMS measurement. The signal corresponding to Co also exhibits a maximum, but the rise of the Co mole fraction is far less fast as that of the Fe, and the Co mole fraction maximum follows the Fe maximum delayed by about 20-30 nm. Then, the Co mole fraction also decreases, and the steady-state composition is achieved after some 150 nm deposit thickness.

The data presented above (like several others, see [18,19]) indicate that the components of the electrodeposited alloys accumulate sequentially in the order of their deposition preference. The deposition rate of Fe is high at the beginning, which manifests itself by a large Fe mole fraction in the near-substrate zone of the deposit. Since the Fe^{2+} concentration in the bath is small, the depletion of the solution in the cathode vicinity leads to a decrease in the deposition rate, and the Fe mole fraction declines. As the deposition rate of Fe decreases, Co starts replacing it, but the combination of deposition preference and depletion results in a Co mole fraction maximum, too. The achievement of the steady-state is related to a stabilization of the depletion (composition profile of the precursor ions) in the solution that determines then the transport rate of the ions toward the substrate.

The quantitative comparison of the samples deposited from citrate-free and citrate-containing solutions supports the view that the spontaneous initial composition change is related to the transport processes in the solution. The citrate ions form a complex with the majority of the metal cations, and the reason of its application to Ni-Co-Fe baths lies in the beneficial impact on the bath stability and the resulting phase structure and magnetic properties of the deposits [39,40]. The

sodium citrate concentration is 2/3 of the total metal ion concentration in the present study. Even under these conditions, the diffusion of the complexed precursor ions can be assumed to be slower than that of the non-complexed ones. Hence, the decay rate of the mole fractions of the preferentially deposited metals (dy/dx where x is the thickness and y is the mole fraction) is larger if the transport rate is smaller. This can be well seen in the comparison of the profiles of the two alloys in Figure 6. It is to be noted that the pH also differs for the two baths used in the above comparison. It is also known [41-43] that the mole fraction of Fe and Co in Ni-Co-Fe deposits decrases with the increase in pH if pH >2.8. However, we can exclude that the effect of the pH is dominant in the composition change observed since the initial Fe mole fraction is nearly the same. If the pH had a major impact on the composition, the near-substrate mole fractions should also change significantly, which was not observed.

As Figure 6(c) indicates, the composition depth profile can be uneven also after the decay of the initial transient. It can be easily observed that the composition variations are not a consequence of the random experimental errors since they are well correlated with each other. The changes in the mole fraction of Fe and Co exhibit the same direction, while the mole fraction of Ni always shows a countermotion. Further interesting details can be revealed from the interrelation of the mole fractions of the components of the samples if they are displayed as a function of each other. The mole fraction of Fe was selected as the independent variable and all other mole fractions were plotted as a function of y(Fe). This can be seen in Figure 7 for two samples deposited from the same bath with different current densities.

If the sample is deposited with a large enough current density (-24 mA cm^{-2}, see Figure 7), the Co mole fraction is linearly proportional to the iron mole fraction: y(Co) = $k y$(Fe), and $k \approx 1/3$. The value of the proportionality factor k can be compared to the $c(Co^{2+})/c(Fe^{2+})$ ratio, which was 3. If both components were deposited at the diffusion limited rate, the concentration ratio should be close to the k factor since the transport coefficient of the Me^{2+} ions with nearly the same size and weight must be very close to each other. Therefore, we can conclude that at least the Co deposition does not take place at the diffusion-limited rate. There must be, however, a governing factor in the codeposition kinetics which ensures this proportionality. At -24 mA cm^{-2}, the extrapolation to zero Fe^{2+} concentration leads to the result that the Co mole fractions should be zero. This is clearly impossible since, in the absence of Fe^{2+}, the anomalous codeposition should lead to a relatively Co-rich deposit. These data indicate indirectly that the anomalous codeposition involves the inhibition of the deposition of some metals of lower deposition preference, as it was also indicated by the measurements of Podlaha *et al.* [30,36]. As the current density decreases (see data corresponding to -10.6 mA cm^{-2} in Figure 7), the mole fraction of both Fe and Co increases. At the same time, the relationship between the mole fractions of the components remains linear, but the functional form is different: $y(Co) = y(Co)_0 + k' y(Fe)$; *i.e.,* the extrapolation to zero Fe^{2+} concentration does not result in zero Co content, and $k' < k$. This indicates that at a relatively low current density, the anomalous codeposition preference between Co and Ni can also manifest itself, and the dependence of the Co content on the Fe content becomes weaker. Since Ni is the metal of the weakest deposition preference but with the highest precursor ion concentration, its deposition can be regarded as the reaction that takes the "leftover" current not used by either Fe or Co deposition. Hence, the countermotion of the Ni mole fraction with both the Fe and Co mole fractions is the consequence of the deposition preference and the concentration ratios.

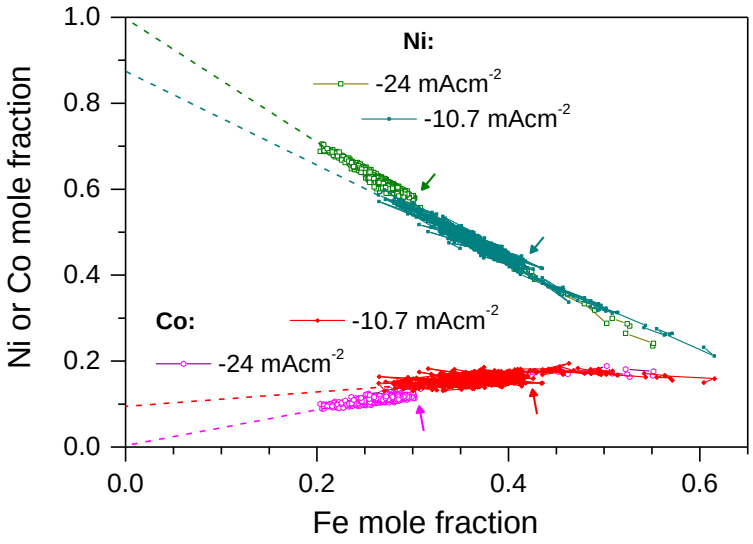

Figure 7. *Interrelation of the mole fractions of two d.c.-plated Si/Cr/Cu//Ni-Co-Fe samples obtained with two different current densities as indicated next to the datasets. The solution composition was the same as for Figure 5(a) and the depth profiles were taken from SNMS measurements. Dashed lines are a guide for the eye only and show the extrapolation of the trend of the corresponding experimental data. The small arrows next to the datasets indicate where the initial composition change decayed (data with larger Fe mole fractions in the same dataset belong to the initial transient).*

It is to be solved yet what can cause a simultaneous increase/decrease in the Fe and Co concentrations in one particular sample in a wide range of current density. One can conclude that this behaviour is the result of the random fluctuation in the mass transport in the solution. If the surface concentration of the two preferentially deposited components, Fe and Co, cannot change simultaneously, the strong correlation between their mole fractions could not occur. It also has to be noted that this fluctuation must extend over the entire substrate surface area, otherwise the sputtering method carried out on spots of 2-3 mm diameter would not be able to reveal it. This problem is also worthwhile to be studied with a direct imaging method that reveals also the lateral composition map of the samples.

TEM analysis of d.c.-plated Ni-Co-Fe alloys obtained from a stagnant solution

The difference in the SNMS composition profile of the d.c.-plated and pulse-plated alloys indicate that the initial composition change observed for the d.c.-plated sample cannot be an instrumental artefact. Nevertheless, it seemed to be worthwhile cross-investigating the results with a direct imaging method. This is why TEM was applied for Ni-Co-Fe samples deposited with analogous conditions than those studied with SNMS reverse depth profiling. In former reports describing a TEM study of Ni-Co-Fe samples [39,41,44-46], the near-substrate composition gradient shownin the previous chapter was not mentioned.

The composition change in the near-substrate zone was observed also with TEM and the features of the initial transition zone proved to be identical to those detected by SNMS. As it is shown in Figure 8, the TEM EDXS results show consecutive maxima in the signal intensities of the components in the order of their deposition preference. The initial transition range was about 200 nm thick, which is only a bit larger than the thickness of these zones as established from SNMS measurements.

The TEM investigation could also confirm that spontaneous long-range composition oscillation can occur during the deposition of Ni-Co-Fe samples from stagnant solutions. The spontaneous composition oscillation beyond the near-substrate zone ranged to a wider interval of the mole

fraction of the components if the current density was larger. At -20 mA cm^{-2} current density, the spontaneous composition oscillation is obvious from the elemental maps (see Figure 9(a)).

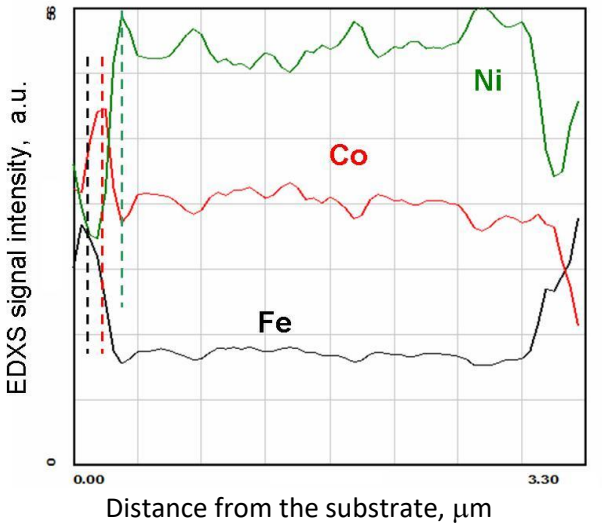

Figure 8. *TEM EDXS study of a d.c.-plated Ni-Co-Fe sample. The dashed lines correspond to the maximum of the signal intensity of the corresponding component in the near-substrate zone.*

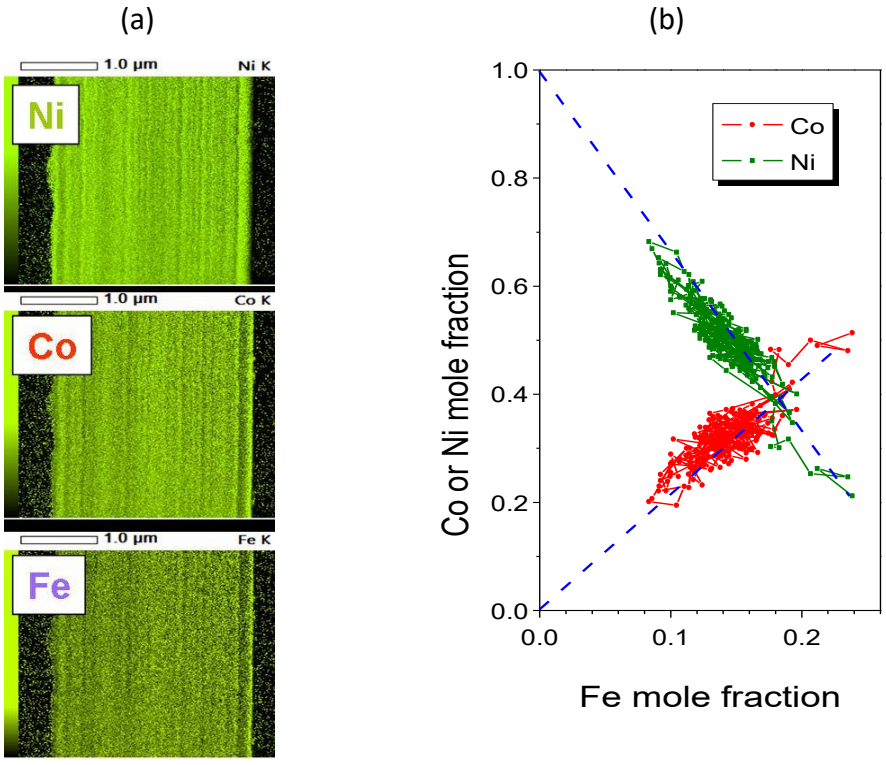

Figure 9*. **(a)** TEM EDXS elemental maps obtained for a d.c.-plated Ni-Co-Fe sample. The substrate is on the right dark edge of the images. **(b)** Mutual dependence of the mole fraction of the components of the same sample as calculated from the line scan perpendicular to the substrate.*

The elemental maps exhibit a complementary nature: light parts of the image show that the Ni intensity always corresponds to dark parts of both the Fe and Co maps and vice versa. This indicates that there is a positive correlation between the mole fractions of Co and Fe, while the Ni mole fraction has a negative correlation with that of the other components. By determining the mole fractions from a line scan performed perpendicular to the substrate, the mole fractions can be plotted in the same manner as in Figure 7 and the result can be seen in Figure 9(b). The similarity of

the character of the two figures is striking, which eliminates all doubts concerning the occurrence of any possible artefact in the SNMS measurements revealing spontaneous random concentration oscillations.

However, there is a peculiar difference between the SNMS and the TEM composition depth profiles. In both measurements, the *y*(Co) = *ky*(Fe) relationship holds, but the *k* parameter is very different (1/3 as derived from the SNMS measurements while nearly 2 from the TEM measurements). This is not yet understood and may rely in the difference in the quantification procedures of the two methods.

It has to be admitted that the preparation of a sample for TEM studies is by far more cumbersome than simply inserting the same sample to the analytical instrument that performs the sputtering and the subsequent analysis.

Nevertheless, the TEM elemental maps have also some advantage as compared to sputtering-based concentration depth profile measurements. Namely, if the undulation of the concentration fluctuation fronts becomes comparable to the thickness of the zones with identical concentration, the sputtering-based measurements will show the mean composition only. The reason of this averaging is that the sputtering front can sample various zones at the same time due to the undulation of the zones with varying composition. The TEM elemental maps can, however, yield fairly complex data: on the one hand, the concentration values as a function of the location and, on the other hand, the apparent roughness of the composition undulation fronts. Therefore, the methods used provide information content of rather complementary nature.

Composition depth profile of Ni-Co-Fe alloys plated under controlled hydrodynamics

For controlling the convection, a rotating disc electrode system was used for the deposition of the samples. The key features of the setup were described in the Experimental and are shown in Figure 2b. The solution in this study contained the following components: 0.2 mol dm^{-3} $NiSO_4$, 0.075 mol dm^{-3} $CoSO_4$, 0.025 mol dm^{-3} $FeSO_4$, 0.4 mol dm^{-3} H_3BO_3, 0.28 mol dm^{-3} NH_4Cl and 0.2 g dm^{-3} saccharin, while the pH was set to 2.8 with sulfuric acid. The ratio of the metal ions was the same as for the Ni-Co-Fe baths mentioned before. The current density was -20 mA cm^{-2} and the electrode rotation was 70-210 rpm.

First, a sample was deposited onto a Si/Cr/Cu wafer in order to check the lateral homogeneity of the deposit. The analysis was performed with EDXS on 200 μm x 200 μm spots along the radius of the wafer. The result is shown in Figure 10. The composition was fairly stable along the radius and the deviations of the mole fractions of the components from their average values were uncorrelated with each other. This supports the view that the deviations should be attributed to random errors and no systematic trend can be established.

The composition analysis indicates that the electrode rotation had a significant impact on the composition. Samples prepared from a stagnant solution of nearly the same composition contained 50-70 at.% Ni, 15-10 at.% Co and 45-25 at.% Fe [18] (the molar percentages are listed above in such an order that their sequence for a given element indicates the composition change upon increasing current density). In contrast, the deposit obtained from a well-stirred solution was rich in cobalt. This corresponds very well to the deposition preference and to the suppression of the role of the transport of the precursor ions.

Several samples were prepared with various current densities and electrode rotation frequencies for reverse depth profile analysis. A typical result of the SNMS measurements is presented in Figure 11.

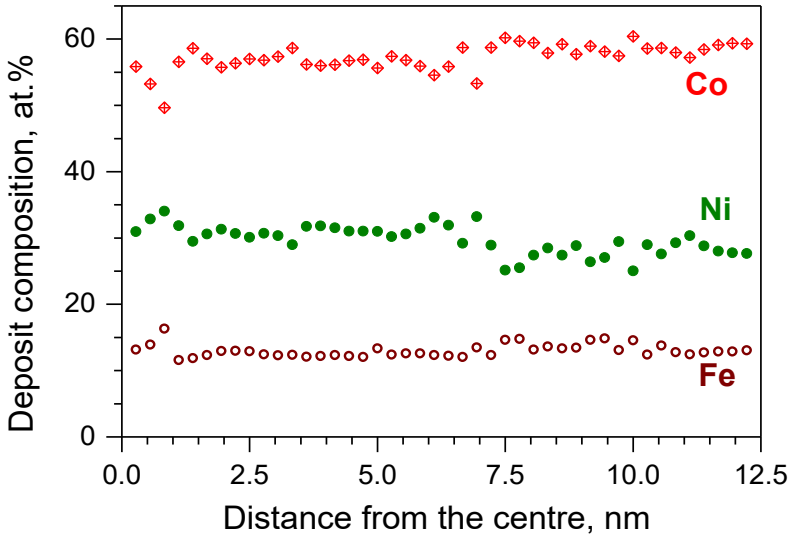

Figure 10. *Result of the EDXS analysis of a Ni-Co-Fe deposit obtained by galvanostatic deposition on a rotating disc electrode (210 rpm).*

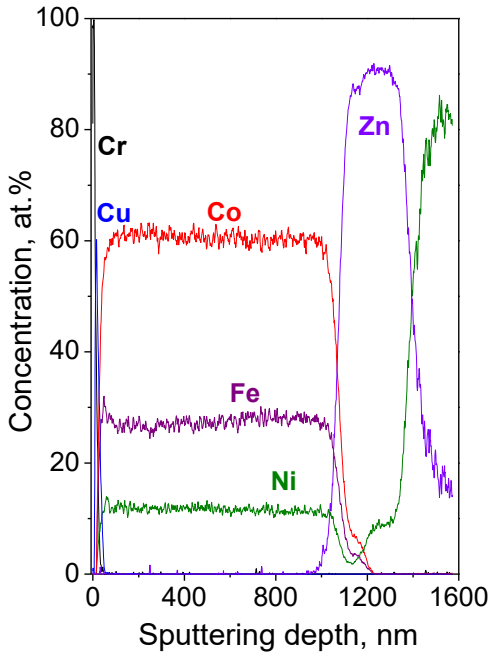

Figure 11. *Reverse SNMS composition depth profile curves of a Ni-Co-Fe deposit obtained by galvanostatic deposition on rotating disc electrode after removing the Si wafer substrate. The graph shows the complete structure with the substrate layers (Cr and Cu), the Ni-Co-Fe deposit, the Zn interlayer and the Ni covering layer (support).*

An essentially even composition profile was obtained for each sample, and the composition fluctuation often observed in samples obtained from a stagnant solution was never detected. The apparent composition fluctuation was well within the usual error of the SNMS measurement and, hence, it is unrelated to the features of the samples. The variation of the mean composition with current density was an order of magnitude smaller than in a stagnant solution. The variation of the electrode rotation rate in the 70-350 rpm range did not have a significant impact on the composition.

The composition change in the near-substrate zone was also small as compared to d.c.-plated samples obtained from stagnant solutions. Although the mole fraction of iron was always slightly larger in the near-substrate region than in the bulk, the change in the Fe concentration in the near-substrate zone was at most 6 at.% (c.f. 20-35 at.% change in samples obtained from stagnant

solutions). This mole fraction decay was compensated almost equally by a mole fraction increment of Co and Ni. The deposit thickness range in which this composition change took place shrunk in the stirred solution as compared to the stagnant one. While a 150-200 nm thick transition zone was observed for stagnant solutions, the transition zone thickness was less than 40 nm for samples deposited onto rotating discs.

Although the lack of a visible composition fluctuation in a set of samples cannot be taken as an absolute evidence for the complete elimination of the composition fluctuations, the full analysis of the composition profiles strongly underpins that the controlled hydrodynamics of the solution stabilizes the deposit composition and prevents the formation of a thick initial transition zone with large composition changes. Hence, the role of the mass transport in the occurrence of uneven composition of the alloy deposits is strongly evidenced with the latter experiments.

Composition depth profile of Ni-Cu/Cu multilayers

$[Ni\text{-}Cu/Cu]_N$ multilayers were deposited with the so-called G/P method [16] from an acetate/citrate bath [21,47]. By using this protocol, the alloy layer was obtained with a galvanostatic pulse, whose amplitude was suitable for the regulation of the composition of the Ni-Cu layer. The Cu partial current density (j_{Cu}) was measured and then assumed to be constant also during the high-current pulse (Ni-Cu layer). Hence, the nominal layer composition was calculated as follows: $y_{Cu} = j_{Cu}/j_{TOTAL}$ and $y_{Ni} = 1 - y_{Cu}$. The nickel mole fraction in the layers was set to 0.9, 0.75 and 0.4, and the corresponding layers will be denoted henceforth as high (H), medium (M) or low (L) Ni-content layers, respectively. The Cu layers were deposited with a potentiostatic pulse controlling the layer thickness with the real-time current integration during deposition. The Cu deposition potential was chosen so that Ni could neither deposit nor dissolve. Further details of the sample preparation as well as the evaluation method of the GD-ToFMS spectra were published elsewhere [21]. Since the low-pressure chamber of the GD device and the ambient-pressure environment is separated by the sample itself during the measurement, the foil preparation for the reverse sputtering method could not be used here, and hence, the analysis was performed with the conventional sputtering direction for deposits still on their Si/Cr/Cu substrate (i.e., from the solution side toward the substrate).

Figure 12 shows a representative qualitative depth profile measurement for a multilayer with the L-M-H order of the Ni layers (as counted in the order of their deposition). The profile well reveals the layered structure of the sample, and the relative peak intensities of the Ni signals also indicate the sequence of the Ni layers with various composition. The layer structure as estimated from the signal of different isotopes of the same element is identical.

The curves shown in Figure 12 all exhibit a long decay period after the sputtering of the corresponding layer finished. This is an inherent feature of the GD-ToFMS method. The long decay of the signals of each isotope explains why the Ni signal cannot decrease to zero when the Cu layer is sputtered and why the multilayer components are observed when the sputtering front reached the substrate. Besides the features of the sputtering method itself, the long decay time of the signals can also be explained with the sputtering direction. Since the conventional sputtering direction could only be used here, the sputtering started at a surface which exhibits a significant roughness. The resulting sputtering intensities are obtained as a convolution of the sputtering front to the layered structure, which leads to a widening of the wave corresponding to a particular isotope. Therefore, the present measurements are not suitable for the direct comparison of the accuracy of the sputtering-based analysis methods themselves (SNMS and GD-ToFMS), but are highly influenced by the sputtering direction, too.

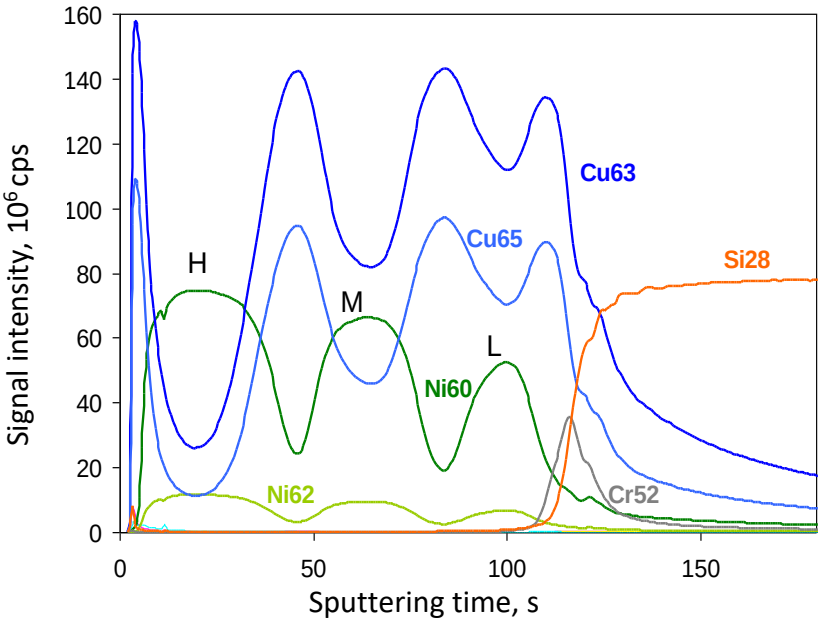

Figure 12. *GD-ToFMS composition depth profile curve of a Si/Cr/Cu//[Ni-Cu/Cu]$_3$ multilayer. Thickness of the Ni-Cu and intermediate Cu layers: 80 nm, thickness of the top Cu layer: 40 nm. The order of the Ni-Cu layers follows the sequence of their deposition: L-M-H (from right to left in the graph). Numbers next to the chemical symbols refer to the atomic weight of the isotope measured.*

An important advantage of the mass spectrometric analysis of the samples is that the major components and the impurities can be detected at the same time. Figure 13 shows the spectra of the same multilayer as in Figure 12 by indicating the signal intensities of different components. Figure 13 clearly shows that metallic impurities that are less noble than Cu are codeposited with Ni. The signal intensity of Co and Fe shows the same variation at large scale as that of Ni. Both Co and Fe show an anomalous codeposition beside Ni, but they cannot be deposited at the potential where Cu is deposited. Therefore, these elements accompany nickel.

It is worthwhile drawing attention to some subtle details of Figure 13. If the variation of the Co and Fe signals is scrutinized within one particular Ni-rich layer, it can be seen that both of them decrease as the deposition proceeds. Since both Fe and Co are preferentially deposited with Ni and their ions are present in a small concentration, the bath is depleted with respect to their ions as the deposition of a particular Ni-rich layer proceeds.

Therefore, the codeposition rate of Fe and Co is expected to decrease as the Ni-rich layer grows. Here, we can see the same phenomenon as the one discussed for Ni-Cd and Ni-Fe alloys in the previous sections. The accumulation of the preferentially deposited metals in the early phase of the deposition of the Ni layer is so obvious that it can be detected also in the conventional sputtering direction, even though the resolution of the measurement in this sputtering mode is smaller than for the reverse sputtering mode. If we compare the Co and Fe signal intensities in the subsequent Ni layers, we can see a decrease. This is related to the current density applied during the deposition of each Ni layer. Since the Co^{2+} and Fe^{2+} ions are present in the bath in small concentrations only, their deposition beside Ni becomes diffusion limited. The larger the total current density, the larger the ratio of Ni deposition rate as compared to that of the impurities. Hence, the Fe and Co concentration in Ni is expected to decrease as the current density increases. This can be well seen in the data of Figure 13.

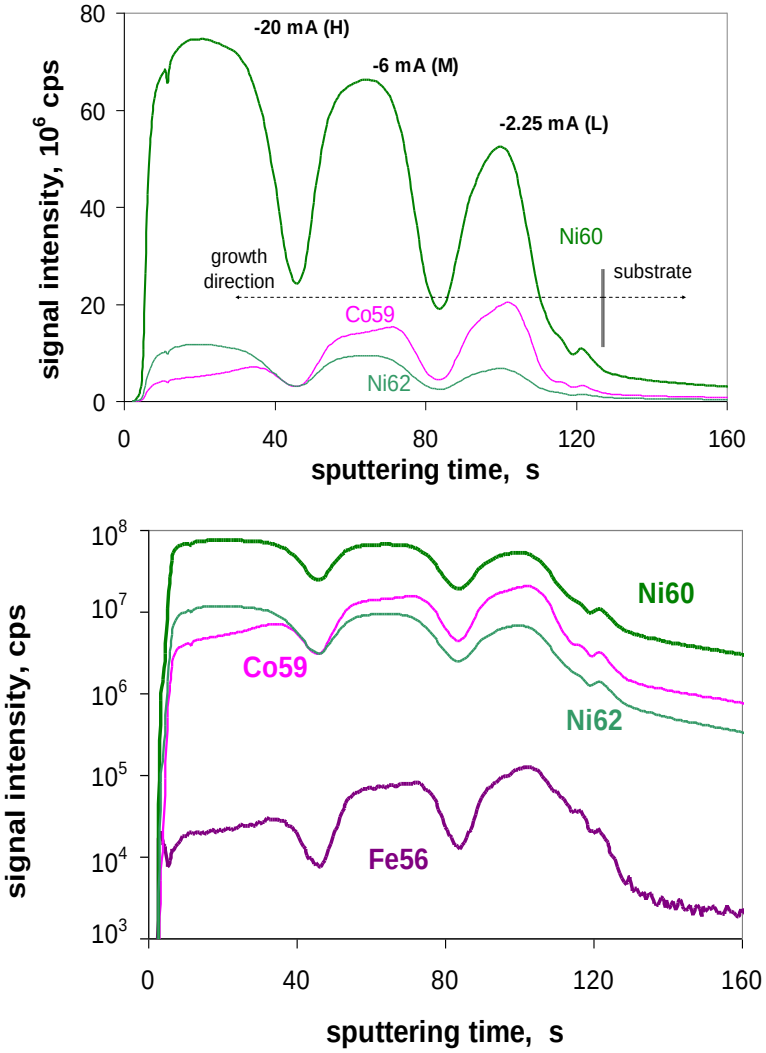

Figure 13. *GD-ToFMS composition depth profile curve of a Si/Cr/Cu//[Ni-Cu/Cu]$_3$ multilayer by showing major and minor metallic components. Top: linear intensity scale, bottom: logarithmic intensity scale. The sample is identical to that depicted in Figure 12.*

The GD-ToFMS method was particularly suitable to detect non-metallic minority components, too. Figure 14 shows the component depth profile of a finer multilayer structure with 40 nm thick layers. As the data show, the signal intensity of the minor components (C, Na and Cl) follow the same oscillation pattern as the multilayer and their intensity maxima coincide with those of Cu.

The composition depth profile spectra shown in Figure 14 are not sufficient alone to determine what causes the correlation between the intensity change of some components. The most likely reasons can be (i) the preferred codeposition of the impurities with Cu rather than Ni, (ii) the adsorption and co-adsorption of the components of the solution on Cu followed by their embedding by the growing layer, and (iii) the formation of cavities in Cu with a higher probability than in Ni. The codeposition theory seems to be rather unlikely since Na cannot be deposited at all at the potential where Cu is deposited, and chloride ions do not react at the cathode either. The adsorption of the citrate ions on copper is possible. Since the citric acid has several carboxilate groups and at the pH of the solution the protons can be dissociated, attachment of the Na^+ ions by Coulombic interaction is well possible. If the detachment of the citrate ion (or its fragment) cannot take place before it is embedded by the growing Cu layer, all elements whose atoms are either present in the citrate ion itself or may accompany it can appear in the depth profile spectra. However, the simultaneous

occurrence of Cl still requires another explanation. The cavity formation in the Cu layer can explain the occurrence of all elements of the solution. However, in this case, sulfur should also be present in the cavities due to the relatively high sulfate ion concentration of the bath. In contrast with the expectation, the sulfur signal was around the background level throughout the measurement and did not exhibit a simultaneous oscillation with the rest of the solution components. This hints at the possibility that the cavity formation theory is to be abandoned, and the preferential occurrence of the impurities in the Cu layer is to be explained with some specific chemical interaction between the growing Cu surface and the solution components.

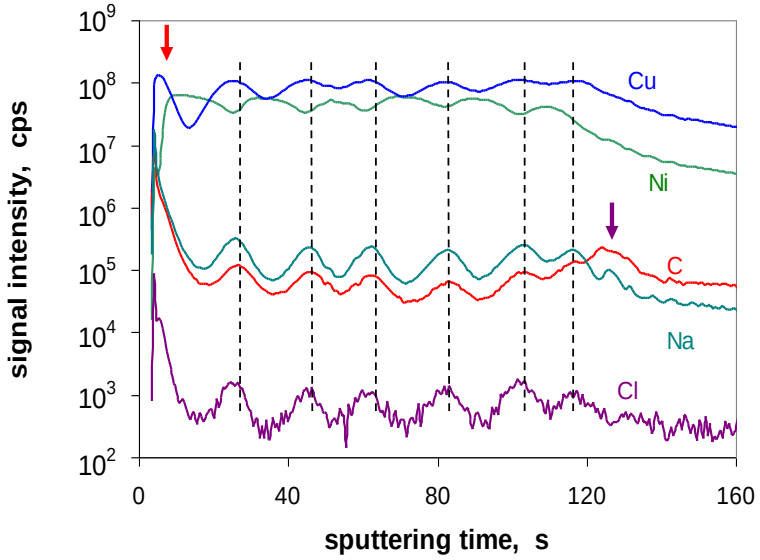

Figure 14. *GD-ToFMS composition depth profile curve of a Si/Cr/Cu//[Ni-Cu/Cu]$_6$ multilayer. Thickness of the Ni-Cu and intermediate Cu layers: 40 nm, thickness of the top Cu layer: 20 nm. The order of the Ni-Cu layers follows the sequence of their deposition: H-M-L-H-M-L (from right to left in the graph). Dashed lines are drawn to the maxima of the Cu intensity and serve as a guide for the eye only. The two arrows indicate the initial surface of the substrate (right) and the final surface of the deposit (left).*

The quantitative analysis of the spectra shown in Figure 14 is shown in Figure 15. The quantitative analysis clearly shows the difference between the Ni and total iron-group metal content of the Ni-rich layers as a function of the Ni concentration. The lower the Ni concentration of the Ni-rich layer (i.e., the lower the current density), the larger the contribution of Co and Fe to the total iron-group metal content of the Ni-rich layers. The carbon concentration of the deposit is rather significant, ranging to 2 at.% in the Cu layers. It is important to note that the carbon content of a deposit practically always remains hidden regardless of the nature of the major metallic constituents if the analysis is made with EDXS in an electron microscope (in both SEM and TEM) since the carbon signal is typically attributed to surface impurities only. However, in the present measurement, the low intensity of the carbon signal during the sputtering of the Ni layer indicates that the vacuum system is clean. The surface impurity occurs only at the beginning of the sputtering process and it decays fast. The oscillation of the carbon signal after the sputtering of the Ni-rich layer just beneath the top Cu layer must be attributed to the feature of the bulk of the sample.

The bottom graph in Figure 15 shows the interrelation of the C and Cu content of the multilayer sample. As the carbon signal decays shortly after the start of the sputtering due to the removal of the surface impurities, the function travels nearly the same trajectory forth and back as the sputtering front reaches a Cu and a Ni-rich layer. This indicates that the incorporation of the carbon-containing impurity takes place in parallel with the deposition of Cu and it is likely caused by a specific chemical interaction.

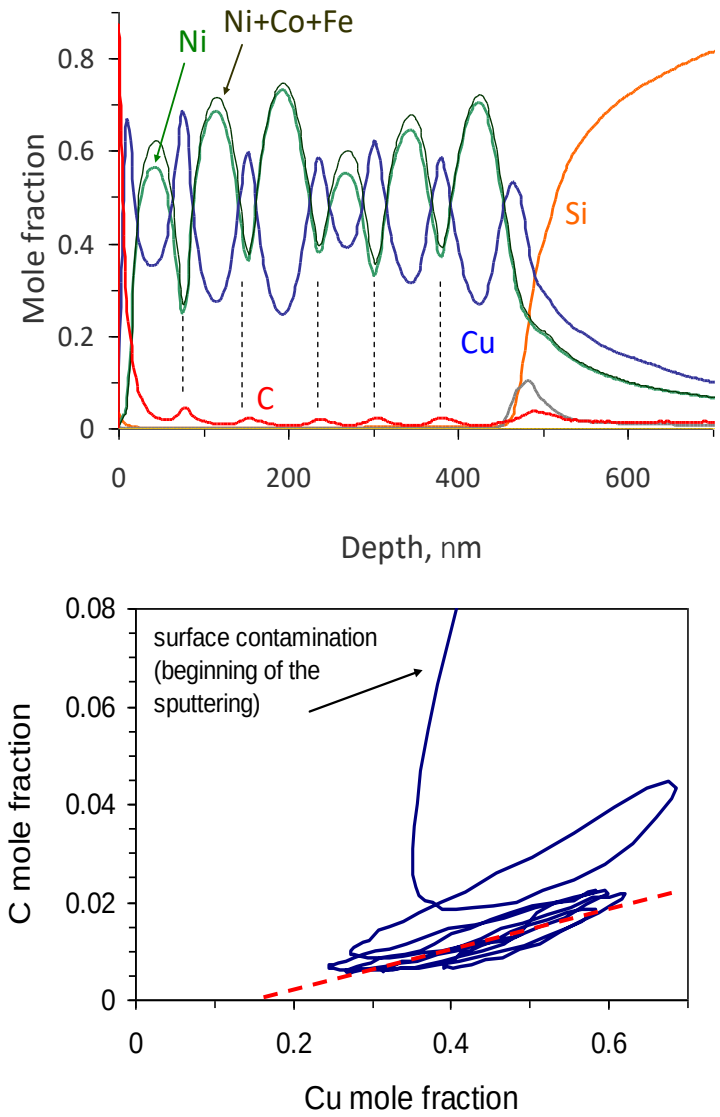

Figure 15. *GD-ToFMS composition depth profile curve of a Si/Cr/Cu//[Ni-Cu/Cu]$_6$ multilayer (same sample as for Figure 14). Top: quantitative depth profile; bottom: interrelation of the C and Cu content of the deposit. Dashed lines serve a guide for the eye only.*

Conclusions

It was shown that modern composition depth profiling methods like SNMS and GD-ToFMS can be used to gain highly specific composition depth profile information on electrodeposited alloys. With the reverse sputtering direction, the near-substrate composition evolution can be revealed with unprecedented precision. It was shown that upon d.c. plating from unstirred solution, the preferentially deposited metal accumulates in the near-substrate zone, and the steady-state alloy composition sets in at about 150-200 nm deposit thickness only. If there is more than one preferentially deposited metal in the alloy, the accumulation zones of these metals occur in the order of the deposition preference. This accumulation zone can be eliminated by various means. Well-controlled hydrodynamic conditions (like the application of rotating disc electrodes) lead to a significant reduction of both the component accumulation and the thickness of the transition period. Pulse plating has a similar impact where the systematic decrease in the duty cycle provides a gradual transition from a graded to a uniform composition depth profile. These observations can be very useful where attachment of a deposit to the substrate is highly impacted by the composition

of the adjacent deposit layer. Also, when the uniformity of the composition plays a role in the deposit properties (like the even composition for the coercive force of a magnetic metal), the proper choice of the deposition conditions can also be crucial.

The comparison of the sputtering-based and TEM EDXS composition depth profile data demonstrated the complementary nature of such studies. The very systematic composition variation as shown up in the SNMS measurements performed over several mm^2 surface area provides a clear evidence for that the samples are laterally homogeneous. However, the undulation of the concentration fluctuation fronts distorts the sputtering-based analysis, while they are visible in the cross-sectional TEM analysis.

The application of composition depth profile measurements makes it possible to detect the coincidence in the occurrence of some components in the deposits down to the impurity level. This was exemplified by the GD-ToFMS measurements of Ni-Cu/Cu multilayers where all detected impurities accumulated in the Cu layer. The wealth of information obtained by these methods provides a much more detailed picture than the results normally obtained with bulk analysis and help in the elucidation of the side reactions taking place during the plating processes.

***Acknowledgements**: L. Péter acknowledges the support of the Hungarian Scientific Research Fund (grants #K-75008 and #K-104696) and the grant funded by Santander Bank for the temporary recruitment of teaching staff to the University of Oviedo (Oct-Nov 2016). SNMS measurements were carried out in the framework of the TÁMOP 4.2.2.A-11/1/KONV- 2012-0036 project.*

References

[1] G. Hodes (ed.), Electrochemistry *of Nanomaterials,* Wiley-VCH, Weinheim, 2001
[2] T. Watanabe, Nano-Plating. Microstructure Control Theory of Plated Film and Data base of Plated Film Microstructure. Elsevier, Amsterdam, 2004
[3] Y. Lin Y, H. S. Nalwa (eds), *Handbook of Electrochemical Nanotechnology*, American Scientific Publishers, Valencia, CA, USA, 2009
[4] T. Osaka, M. Datta, Y. Shacham-Diamand (eds), *Electrochemical Nanotechnologies*, Springer, New York, 2010
[5] D. Wei (ed), *Electrochemical Nanofabrication*, Pan Stanford Publishing, Singapore, 2012
[6] Aliofkhazraei M (ed), Modern Electrochemical Methods in Nano, Surface and Corrosion Science, InTech, Rijeka, Croatia, 2014
[7] M.V. Mirkin, S. Amenia, *Nanoelectrochemistry*, CRC Press, Boca Raton, Florida, USA, 2015
[8] M. Aliofkhazraei, A.S.H. Makhlouf (eds), Handbook of Nanoelectrochemistry. Springer International Publishing, Cham, Switzerland, 2016
[9] F. Nasirpouri, *Electrodeposition of Nanostructured Materials*, Springer International Publishing, Cham, Switzerland, 2017
[10] G. H. Cockett, E. S. Spencer-Timms, *Journal of the Electrochemical Society* **108** (1961) 906-908
[11] W. D. Doyle, *Journal of Applied Physics* **38** (1967) 1441-1142
[12] R. Girard, *Journal of Applied Physics* **38** (1967) 1423-1430
[13] E. Beltowska-Lehman, A. Riesekampf, *Thin Solid Films* **71** (1980) 129-132
[14] J. Gong, S. Riemer, A. Morrone, V. Venkatasamy, M. Kautzky, I. Tabakovic, *Journal of the Electrochemical Society* **159** (2012) D447-D454
[15] L. Péter, J. Pádár, E. Tóth-Kádár, Á. Cziráki, P. Sóki, L. Pogány, I. Bakonyi, *Electrochimica Acta* **52** (2007) 3813-3821
[16] V. Weihnacht, L. Péter, J. Tóth, J. Pádár, Z. Kerner, C.M. Schneider, I. Bakonyi, *Journal of The Electrochemical Society* **150** (2003) C507-C515
[17] A. Bartók, A. Csik, K. Vad, G. Molnár, E. Tóth-Kádár, L. Péter, *Journal of the Electrochemical Society* **156** (2009) D253-D260
[18] L. Péter, A. Csik, K. Vad, E. Tóth-Kádár, Á. Pekker, G. Molnár, *Electrochimica Acta* **55** (2010) 4734-4741

[19] K. Neuróhr, A. Csik, K. Vad, A. Bartók, G. Molnár, L. Péter, *Journal of Solid State Electrochemistry* **15** (2011) 2523-2544
[20] K. Neuróhr, A. Csik, K. Vad, G. Molnár, I. Bakonyi, L. Péter, *Electrochimica Acta* **103** (2013) 179-187
[21] R. Muñiz, L. Lobo, K. Németh, L. Péter, R. Pereiro, *Spectrochimica Acta Part B* **135** (2017) 34-41
[22] S. S. Abd El Rehim, S. M. Abe-El Wahaab, O. M. Abdella, *Surface Technology* **21** (1984) 245-253
[23] V. D. Jović, N. Tošić, *Journal of Electroanalytical Chemistry* **441** (1998) 69-76
[24] A. C. Hegde,V. R. Rao, *Journal for Electrochemistry and Plating Technology*, May 2014, paper 3300 (available at https://www.jept.de/?p=3300; DOI: 10.12850/ISSN2196-0267.JEPT3300
[25] H. J. Goldschmidt, M. J. Walker, *Journal of Applied Crystallography* **2** (1969) 273-281
[26] F. A. Shunk, P. Nash, *Journal of Phase Equilibra* **8** (1987) 122-124
[27] P. P. Jana, S. Lidin, *CrystEngComm* **15** (2013) 745-753.
[28] A. Brenner, *Electrodeposition of Alloys,* Academic Press, New York, 1963, Chapter 5., pp. 75-78,
[29] H. Li, F. Ebrahimi, *Materials Science and Engineering* A **347** (2003) 93-101
[30] N. Zech, E.J. Podlaha, D. Landolt, *Journal of the Electrochemical Society* **146** (1999) 2886-2891
[31] N. Zech, E.J. Podlaha, D. Landolt, *Journal of the Electrochemical Society* **146** (1999) 2892-2900
[32] K. Sasaki, J.B. Talbot, *Journal of the Electrochemical Society* **142** (1995) 775-782
[33] J. Vaes, J. Fransaer, J.P. Celis, *Journal of the Electrochemical Society* **149** (2002) C567-C572
[34] Y. Zhuang, E. J. Podlaha, *Journal of the Electrochemical Society* **147** (2000) 2231-2236
[35] Y. Zhuang, E. J. Podlaha, *Journal of the Electrochemical Society* **150** (2003) C219-C224
[36] Y. Zhuang, E. J. Podlaha, *Journal of the Electrochemical Society* **150** (2003) C225-C233
[37] A. Csik, K. Vad , E. Tóth-Kádár, L. Péter, *Electrochemistry Communications* **11** (2009) 1289-1291
[38] X. Liu, G. Zangari, L. Shen*, Journal of Applied Phisics* **87** (2000) 5410-5412
[39] Y. Zhang, D. G. Ivey, *Chemistry of Materials* **16** (2004) 1189-1194
[40] Y. Zhang, D. G. Ivey, *Materials Science and Engineering* B **140** (2007) 15-22
[41] X. Liu, G. Zangari, M. Shamsuzzoha, *Journal of the Electrochemical Society* 150 (2003) C159-C168
[42] F.E. Atalay, H. Kaya, S. Atalay, *Physica B* **371** (2006) 327-331
[43] Y. Yang, International Journal of Electrochemical Science **10** (2015) 5164-5175
[44] T. Nakanishi, M. Ozaki, H. S. Nam, T. Yokoshima, T. Osaka, *Journal of the Electrochemical Society* **148** (2001) C627-C631
[45] M. Saito, N. Ishiwata, K. Ohashi, *Journal of the Electrochemical Society* **149** (2002) C642-C647
[46] I. Tabakovich, V. Inturi, S. Riemer, *Journal of the Electrochemical Society* **149** (2002) C18-C22
[47] R. Caballero-Flores, V. Franco, A. Conde, L. F. Kiss, L. Péter, I. Bakonyi, *Journal of Nanoscience and Nanotechnology* **12** (2012) 7432-7436

J. Electrochem. Sci. Eng. **8(1)** (2018) 73-85; DOI: http://dx.doi.org/10.5599/jese.475

Open Access : : ISSN 1847-9286

www.jESE-online.org

Original scientific paper

DFT calculations and electrochemical studies on azulene ligands for heavy metal ions detection using chemically modified electrodes

Amalia Stefaniu[1], Maria-Daniela Pop[2], Georgiana-Luiza Arnold[2], Liviu Birzan[3], Lucia Pintilie[1], Elena Diacu[4], Eleonora-Mihaela Ungureanu[2,✉]

[1]*National Institute of Chemical - Pharmaceutical Research and Development - Bucharest, 112 Vitan Av., 031299, Bucharest, Romania*
[2]*Department of Inorganic Chemistry, Physical Chemistry and Electrochemistry, University "Politehnica" of Bucharest, Gh. Polizu 1-7, 011061, Bucharest, Romania*
[3]*Romanian Academy, Institute of Organic Chemistry "C. D. Nenitzescu", Spl. Independentei, 202B, 060023-Bucharest, 35 P.O. Box 108, Romania*
[4]*Department of Analytical Chemistry and Environmental Engineering, University "Politehnica" of Bucharest, Gh. Polizu 1-7, 011061, Bucharest, Romania*

Corresponding author E-mail: ✉eleonoramihaelaungureanu@gmail.com

Received: November 18, 2017; Revised: January 13, 2017; Accepted: January 14, 2017

Abstract

A computational study on three related derivatives of 5-[(azulen-1-yl)methylene]-2-thioxoimidazolidin-4-one was conducted using density functional theory by calculating a series of molecular descriptors and properties of their optimized geometries (electrostatic and local ionization potentials, molecular frontier orbitals, etc.). Thermodynamic properties (zero-point energy, enthalpy, constant volume heat capacity, entropy and Gibbs energy) for these derivatives have been calculated and related to ligands electrochemical behavior. Reduction and oxidation potentials have been correlated to their calculated energy levels for LUMO and HOMO orbitals. Chemically modified electrodes based on these derivatives have been tested in view of heavy metal ions recognition, and their detection limits have been correlated to the calculated values of electron affinity.

Keywords

5-[(azulen-1-yl)methylene]-2-thioxoimidazolidin-4-one derivatives; quantum mechanical calculations; electrochemical behavior; modified electrodes; heavy metal ions

Introduction

Azulenes have a push-pull structure, with a five-member cyclic moiety (electron-rich) connected to a seven-member cyclic moiety (electron-poor). Azulene derivatives undergo irreversible

electrooxidations and irreversible or quasi-reversible reductions when polarized at anodic or cathodic potentials, respectively [1]. Due to their low oxidation potential, they can lead to modified electrodes which could be used to build new electrochemical sensors. The sensors based on azulene derivatives are the basis of most recent methods for determination of heavy metals from water samples [2]. This method leads to comparable results to the best-known methods known to date, such as those based on iron oxide/graphene composite [3], bismuth nanoparticle-porous carbon paste [4], etc.

The azulenes investigated in this study are derivatives of 5-[(azulen-1-yl)methylene]-2-thioxo-imidazolidin-4-one (L1), shown in Fig. 1, which have in their structure complexing imidazolidine group, specific for the recognition of heavy metal ions [5]. One of these ligands, L2, has been investigated in molecular recognition for building complexing chemically modified electrodes for heavy metals, and lead to promising results for the heterogeneous recognition of Pb(II) and Cu(II) ions [6]. Similar azulenes with the thiourea moieties as complexing monomers have led to modified electrodes with good complexing abilities for heavy metals, with very good responses for Cd(II) and Pb(II) ions [7].

The present work reports on the investigation of L1 - L3 compounds ability to coordinate heavy metals. Chemically modified electrodes have been prepared from these ligands under similar conditions and used for heterogeneous recognition. Their detection limits for some heavy metal ions (Hg, Pb, Cd, Cu) have been evaluated in order to be correlated to their molecular structural descriptors. Density functional theory (DFT) investigations on these azulenes derivatives have been performed to reveal some global reactivity parameters derived from frontier molecular orbitals energy diagram, to be linked with their ability to complex heavy metals, for electrochemistry applications. Predicted structural characteristics are optimized, compared and correlated in terms of NMR chemical shifts, aiming to determine the structure thermodynamically favored by synthesis [5]. Then, their computed parameters are obtained and analyzed in connection with some complexing and redox properties determined by electrochemistry. Our interest concerns the use of L1 – L3 as ligands in heterogeneous recognition of heavy metals (Fig. 1). The main parts of their structure are illustrated with different colors in Fig. 1. They are the seven-member azulene ring (I), the five-member azulene ring (II) and the imidazolidine ring (III).

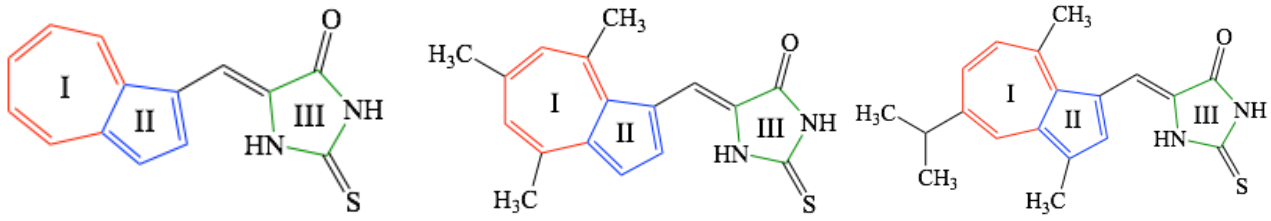

Figure 1. *2D structure of investigated compounds*

Experimental

Acetonitrile (CH_3CN) and tetrabutylammonium perchlorate (TBAP) from Fluka were used as received for the solvent and supporting electrolyte. The azulene derivatives were synthesized according to the previous described method [5].

The electrochemical characterizations were carried out using a PGSTAT 12 AUTOLAB potentiostat connected to a three-electrode cell. The working electrode was a glassy carbon disk (3 mm diameter). The active surface was polished before each determination with diamond paste (1 µm) and cleaned with acetonitrile. $Ag/AgNO_3$ (10 mM) in 0.1 M TBAP, CH_3CN was used as reference

electrode and a platinum wire was used as auxiliary electrode. The electrochemical experiments were performed by cyclic voltammetry (CV), differential pulse voltammetry (DPV) and rotating disk electrode (RDE). CV curves were recorded from 0.1 V/s to 1.0 V/s (for different scan rate). DPV curves were recorded at 0.01 V/s with a pulse height of 0.025 V and a step time of 0.2 s. RDE curves were recorded at 0.01 V/s, for various rotation rates of the disk (between 100 and 2000 rpm). The potential was referred to the potential of the ferrocene/ferrocenium redox couple (Fc/Fc^+) which in our experimental conditions was +0.07 V. The preparation of the modified electrodes has been done by controlled potential electrolysis in millimolar solutions of each ligand, in acetonitrile solutions containing TBAP (0.1 M) as supporting electrolyte. All electrochemical experiments were performed at 25 °C under argon atmosphere.

The experiments for heavy metals ions detection were carried out in a three-electrode cell (transfer cell). The working electrode was a glassy carbon disk (diameter of 3 mm) electrode modified with each ligand, the reference electrode was Ag/AgCl, 3 M KCl, and the auxiliary electrode was a platinum wire. 0.1 M buffer acetate (pH 5.5) was used as supporting electrolyte. The recognition experiments were performed at 25 °C and under argon atmosphere. The buffer acetate solution was prepared from 0.2 M acetic acid and 0.2 M sodium acetate solutions. Metal cation solutions were purchased from Sigma Aldrich and Fluka: mercury (II) acetate - Sigma Aldrich, cadmium nitrate tetrahydrate - Sigma Aldrich, copper (II) acetate monohydrate - Fluka, lead (II) nitrate - Sigma Aldrich. Heavy metals solutions with concentrations of 10^{-4} and 10^{-6} mol/L, were prepared by successive dilutions from 10^{-2} M stock solutions of mercury (Hg), cadmium (Cd), copper (Cu) and lead (Pb).

The procedure to modify the glassy carbon electrodes consisted in electropolymerization of each ligand in millimolar solutions in 0.1 M TBAP, CH_3CN, followed by cleaning in acetonitrile, equilibration of the modified electrode in 0.1 M acetate buffer at pH 5.5, between -0.9 V and + 0.6 V *vs.* Ag/AgCl, over oxidation in 0.1 M acetate buffer at pH 5.5 between -0.2 V to + 1.2 V.

The accumulation of heavy metal ions has been performed in the assay solutions containing heavy metal ions in different concentrations (starting from 10^{-10} to 10^{-4}) for 20 minutes under magnetic stirring. This step has been followed by the stripping of the accumulated metal ions, after a reduction at -1.2 V for 120 s, in CV or DPV anodic scans with a scan rate of 0.01 V/s. The stripping currents for Cd, Pb, Cu, and Hg currents have been evaluated for each concentration.

Computational procedure details

The calculations were carried out using Spartan 14 software Wavefunction, Inc. Irvine CA USA [8] on Intel(R) Core i5 at 3. 2 Ghz CPU PC. First, the 3D CPK models of the studied compounds were generated. Then, a systematic conformational search and analysis was achieved to establish the more stable conformers of each of the three derivatives of 5-[(azulen-1-yl) methylene]-2-thioxoimidazolidin-4-one, presenting the energy minima. The most stable conformer (lowest energy) was established using MMFF (Molecular Mechanics Force Field for organic molecules developed by Merck Pharmaceuticals) model by refining the geometry for each studied compound. For these refined structures, a series of calculations of molecular properties and topological descriptors has been carried out using [9], software algorithm hybrid B3LYP model (the Becke's three parameter hybrid exchange functional with the Lee-Yang-Parr correlation functional) [9-11] and polarization basis set 6-31G* [8,12] in vacuum, for equilibrium geometry at ground state.

Results and discussion

Quantum mechanical calculations

The atomic numbering scheme given by the Spartan 14 software for structures under study is shown at the beginning of the Table 1. The parameters (bond lengths and dihedral angles) of the compounds L1-L3 have been obtained for the optimized geometries. They are listed in Tables 1-2. The molecular structures comprise two coplanar cycles (I and II) and the cycle III, which can be rotated around C14-C13 bond, showing a small deviation from co-planarity given by the small values of the dihedrals (H7, C14, C13, C12) and (C3, C14, C13, N2). L3 conformer configuration presents also the torsion angles of 119.04° (C18, C15, C7, C4) and 61.03° (C16, C15, C7, C9).

Table 1. *Structure labels and predicted bond lengths (Å) for L1 - L3 compounds.*

L1		***L2***	***L3***
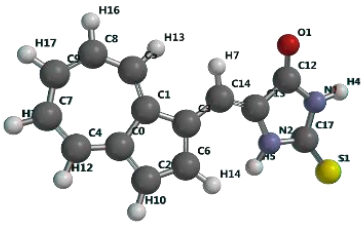		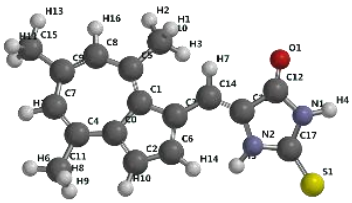	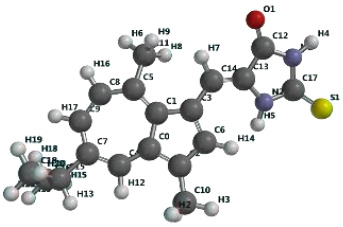
Cycle of 7 atoms (I)			
C5-C1	1.391	1.406	1.408
C5-C8	1.399	1.410	1.409
C8-C9	1.397	1.394	1.395
C9-C7	1.398	1.404	1.398
C7-C4	1.397	1.393	1.400
C4-C0	1.392	1.411	1.391
C0-C1	1.487	1.495	1.496
Substituents (methyl and isopropyl) of cycle I			
-		C5-C10: 1.520	C5-C11: 1.519
-		C9-C15: 1.518	C7-C15: 1.531
-		C4-C11: 1.518	C15-C18: 1.540
-		-	C15-C16: 1.541
Cycle of 5 atoms (II)			
C1-C3	1.429	1.441	1.431
C3-C6	1.424	1.416	1.426
C6-C2	1.391	1.389	1.385
C2-C0	1.411	1.409	1.424
Substituents of cycle II			
-	-		C10 1.502
Chain between cycle II and cycle III			
C3-C14	1.434	1.444	1.441
C14-C13	1.357	1.357	1.358
Cycle III			
C13-N2	1.399	1.400	1.400
N2-C17	1.371	1.369	1.369
C17-N1	1.381	1.382	1.382
N1-C12	1.401	1.401	1.401
C12-C13	1.484	1.483	1.483
Functional groups (C=O and C=S) of cycle III			
C12-O1	1.217	1.217	1.218
C17-S1	1.657	1.658	1.659

Table 2. *Predicted dihedral angles values for L1 - L3 compounds.*

L1	*L2*	*L3*
H13, C5, C1, C3): 0.28°	(C10, C5, C1, C3): 2.20°	C11, C5, C1, C3): 0.85°
(H7, C14, C3, C1): 13.76°	(H7, C14, C3, C1): 26.71°	(H7, C14, C3, C1): 24.08°
(H7, C14, C13, C12): 2.79°	(H7, C14, C13, C12): 1.82°	(H7, C14, C13, C12): 2.29°
(O1, C12, C13, C14): 0.69°	(O1, C12, C13, C14): 1.75°	(O1, C12, C13, C14): 1.51°
(O1, C12, N1, H4): -0.50°	(O1, C12, N1, H4): -0.61°	(O1, C12, N1, H4): -0.65°
(H4, N1, C17, S1): -0.96°	(O1, C12, N1, H4): -0.66°	(H4, N1, C17, S1): -0.76°
(C6, C3, C14, C13): 15.25°	(C6, C3, C14, C13): 28.93°	(C6, C3, C14, C13): 25.79°
(H14, C6, C3, C14): 2.46°	(H14, C6, C3, C14): 0.86°	(H14, C6, C3, C14): 1.49°
(H5, N2, C13, C14): 9.80°	(H5, N2, C13, C14): 7.69°	(H5, N2, C13, C14): 8.79°
(C3, C14, C13, N2): 2.95°	(C3, C14, C13, N2): 5.77°	(C3, C14, C13, N2): 5.61°
(S1, C17, N1, H4): -0.96°	(S1, C17, N1, H4): -0.66°	(S1, C17, N1, H4): -0.76°
(H5, N2, C17, S1): -8.32°	(H5, N2, C17, S1): -7.77°	(H5, N2, C17, S1): -8.38°
	(C11, C4, C0, C2): -0.82°	(C10, C2, C6, H14): -3.39°
	(C11, C4, C7, H15): 0.93°	(C10, C2, C0, C4): -0.13°
	(C15, C9, C8, H16): -1.75°	(C11, C5, C1, C3): 0.85°
	(C15, C9, C7, H15): 0.74°	(C11, C5, C8, H16): 0.69°
	(C10, C5, C8, H16): -1.53°	(C15, C7, C9, H17): -0.21°
	(C10, C5, C1, C3): 2.20°	(C15, C7, C4, H12): 0.96°

In Table 3 are given the results of quantum chemical calculations for a) valuable predicted molecular properties and b) descriptors for L1 – L3 compounds, which provide information to conduct quantitative structure-property relationships (QSPR) for Z isomers.

From Table 3 it can be observed that area and volume for investigated compounds increase in the order: L1< L2 < L3, as expected, correlated with the molecular weight and presence of methyl and isopropyl substituents. The ovality index shows the same trend, suggesting the deviation of molecules from the spherical shape, considering the minimum surface for the spherical shape. This parameter is related to molecular surface area and van der Waals volume and increases with the linearity of the structures in the same order as above-mentioned descriptors (area, volume). The polarizability increases in the order: L1 < L2 < L3, showing increased induction (polarization) interactions, resulting from an ion or a dipole inducing a temporary dipole in an adjacent molecule.

Table 3. *Predicted molecular properties and descriptors for L1-L3 compounds (Z isomers).*

Compound	**L1**	**L2**	**L3**
a) Molecular properties			
Formula	$C_{14}H_{10}N_2OS$	$C_{17}H_{16}N_2OS$	$C_{19}H_{20}N_2OS$
Energy, a.u.	-1122.4149	- 1240.3606	- 1318.9892
Energy (aq), a.u.	- 1122.4367	-1240.3835	- 1319.0106
Solvatation energy, kJ/mol	- 57.22	- 60.24	- 56.12
Dipole moment, Debye	5.86	8.24	8.26
b) QSPR descriptors from CPK model			
Area, $Å^2$	262.59	315.36	354.76
Volume, $Å^3$	247.94	301.04	338.02
Polar surface area, $Å^2$	36.350	37.106	37.037
Ovality	1.38	1.45	1.51
log *P*	0.34	0.87	1.62
HBD Count	2	2	2
HBA Count	4	4	4
Polarizability, 10^{-30} m^3	60.80	65.11	68.15

The same tendency for the dipole moment was observed, as expected. Hydrogen bond donor (HBD) and acceptor (HBA) counts have the same values for all structures under study, due to the

presence of the same thioxoimidazolidine cycle III, containing the same donors (nitrogen) and acceptors (sulphur and oxygen). The octanol-water partition coefficient (log *P*) and polar surface area (PSA) are also evaluated and listed in Table 3. Log *P* values are positive, showing their good affinity for hydrophobic phases, and increase in the order: L1 < L2 < L3. L1 had also the smallest PSA (polar surface area) value reinforcing the trend of log *P*; PSA values for L2 and L3 are quite similar.

HOMO – LUMO analysis

The molecular frontier orbitals (the highest occupied molecular orbital – HOMO and the lowest unoccupied molecular orbital – LUMO) energies of the studied compounds (in Z form) have been calculated (Table 4) and their density distributions are given in the bottom (HOMO) and in the top (LUMO) of Fig. 2, respectively. Analysis of Fig. 2 shows the distribution of HOMO orbitals for all studied compounds is delocalized as follows: over atoms C7 and C8 from cycle I, over bonds C1-C3 and C0-C2 from cycle II, over C13-C14 bond (between cycle II and cycle III) and over heteroatoms N2, O1 and S1 form cycle III. For all compounds, LUMO orbitals (Fig. 2) are entirely delocalized over cycle I and cycle II, while for L2 structure, they are distributed supplementary over functional groups C=O (O1), C=S (S1) and C12-C13 bond from cycle III. The other occupied orbitals energy levels are listed in Table 5, and they can be related with UV Vis allowed transitions.

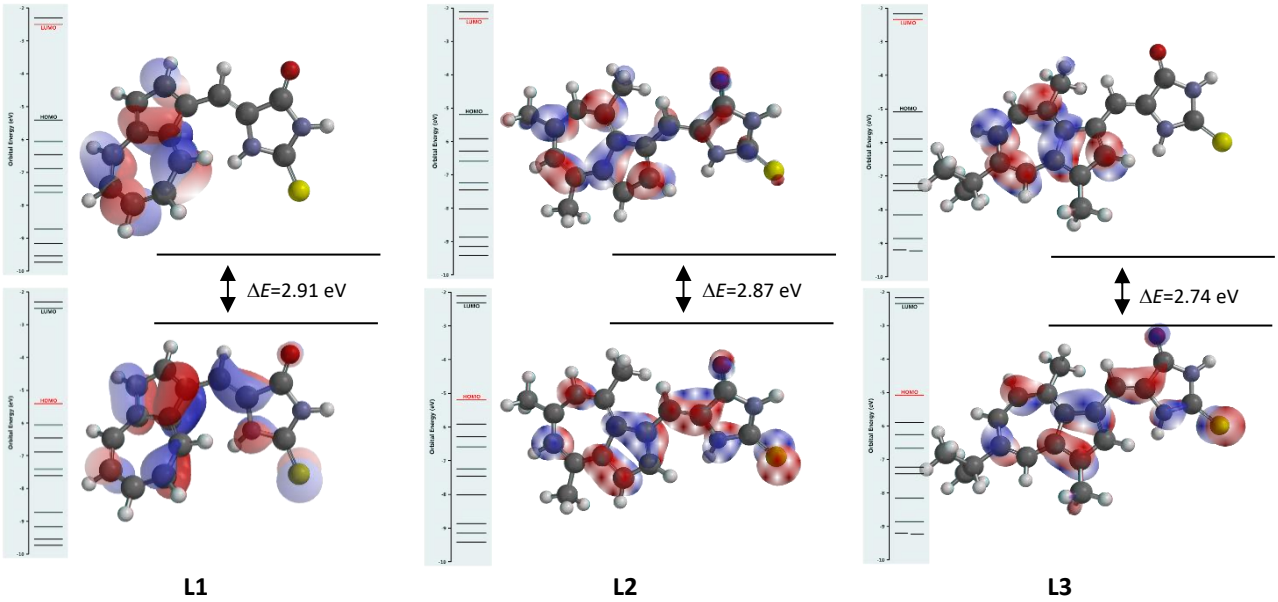

Figure 2. *HOMO (down) and LUMO (up) molecular frontier orbitals and their energy gap for L1 - L3.*

HOMO and LUMO energies from Table 4 have been examined in order to find the tendency of each ligand to donate electrons (to empty molecular orbitals with low energy of convenient molecules), or to accept electrons, respectively. The resulting band gap ΔE (E_{HOMO} - E_{LUMO}) can be used to provide useful information on the chemical reactivity and kinetic stability of each ligand [13,14]. The band gap between the HOMO and LUMO orbitals energy has been found to increase in the order: L3 < L2 < L1 (Table 4). Consequently, according the obtained values for ΔE, L1 presents the lowest reactivity, followed by L2 and L3 (the most reactive). Starting from HOMO and LUMO energy diagram (Fig. 2), other related descriptors have been calculated: ionization potential (I), electron affinity (A), electronegativity (χ), chemical hardness (η), global softness (σ) [15,16], chemical potential (μ), global electrophilicity index (ω), and also ionization potential (defined as I = - E_{HOMO}) and electron affinity (defined as A = - E_{LUMO}), by applying Koopmans' theorem [17,18]. Derived calculated quantum chemical parameters for the most stable conformer (Z) of each studied compound are listed in Table 4.

The parameters from Table 4 are important global chemical reactivity descriptors of the studied molecules in terms of their reactivity and site selectivity. L1 has the highest ionization potential and electron affinity, which reflects his superior capability to interact with heavy metal cations and to accept one electron from a donor. In terms of chemical hardness, large ΔE signifies hard molecules and small ΔE refers to soft molecules. In this context, L1 presents the hardest structure. The values obtained for the electrophilicity index (ω) are not in the same order. It indicates an unexpected global electrophilic nature of these molecules, as measure of energy lowering due to maximal electron flow between donor and acceptor [19].

Table 4. *Calculated quantum chemical* parameters of the studied compounds

Parameter\Ligand	L1	L2	L3
E_{HOMO} / eV	-5.41	- 5.19	- 5.08
E_{LUMO} / eV	-2.50	- 2.32	-2.34
ΔE (E_{HOMO}-E_{LUMO}) / eV	2.91	2.87	2.74
I = - E_{HOMO} / eV	**5.41**	**5.19**	**5.08**
A = - E_{LUMO} / eV	**2.50**	2.32	2.34
χ = ((I + A)/2) / eV	3.95	3.76	3.71
η = ((I - A)/2) / eV	1.45	1.44	1.37
σ = I / η	0.68	0.70	0.73
μ = (E_{HOMO}+E_{LUMO})/2	**-3.95**	**-3.75**	**-3.71**
ω = μ^2 / 2 η	5.37	4.91	5.02

Table 5. *Predicted molecular orbital values (eV) for L1 - L3*

Orbital Ligand	L1	L2	L3
HOMO	-5.4	-5.2	-5.1
HOMO{-1}	-6.1	-5.9	-5.9
HOMO{-2}	-6.5	-6.3	-6.3
HOMO{-3}	-6.9	-6.6	-6.7
HOMO{-4}	-7.4	-7.2	-7.2
HOMO{-5}	-7.6	-7.5	-7.4
HOMO{-6}	-8.7	-8.0	-8.2
HOMO{-7}	-9.2	-8.9	-8.9
HOMO{-8}	-9.5	-9.1	-9.2
HOMO{-9}	-9.7	-9.4	-9.2
LUMO	-2.5	-5.2	-2.3
LUMO{+1}	-2.3	-5.9	-2.2

Molecular electrostatic potential and local ionization potential

Molecular electrostatic potential (MEP) is a valuable descriptor for overall molecular charge distribution and for the way of electrophilic addition assessment [20,21]. Graphical quantities resulted from quantum chemical calculations for MEP and local ionization potential (LIP) are given in Fig. 3. These diagrams provide a visual representation of the chemically active site and comparative reactivity of atoms.

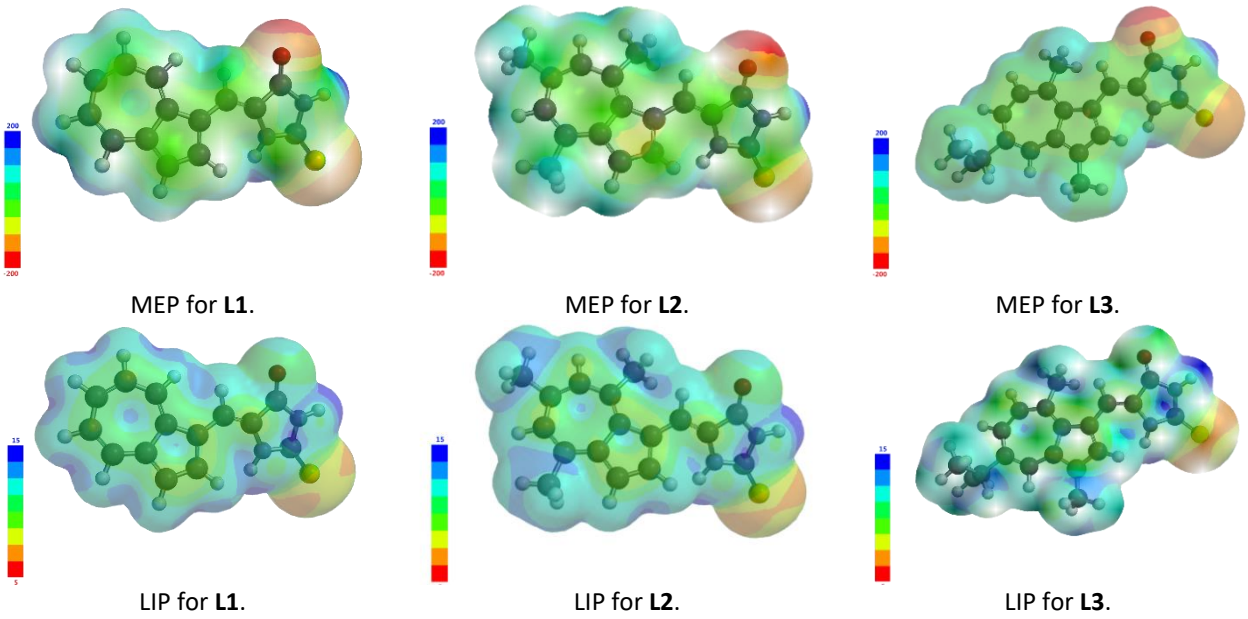

MEP for **L1**. MEP for **L2**. MEP for **L3**.

LIP for **L1**. LIP for **L2**. LIP for **L3**.

Figure 3*. Predicted molecular electrostatic potential (MEP) and local ionization potential (LIP) maps for L1-L3*

In MEP graphical representation from Fig. 3, the red surface (π system) indicates a negative potential, suggesting that this region is attracted to a positive charge; the blue surface (σ system) indicates a positive potential, thus, this region is attracted to negative charges. Potential increases in the order: red < orange < yellow < green < blue. For all the studied compounds, the negative area is mainly localized over the oxygen (red region) and less on sulphur atoms (orange region). The maximum negative values (over sulphur oxygen) have been read and they vary as follow: -203 kJ/mol to -154 kJ/mol (for L1); -168 kJ/mol to -151 kJ/mol (for L2); -171 kJ/mol to -153 kJ/mol (for L3). The maximum positive regions (blue) are localized on the –NH groups from cycle III, assigned to atoms H4 and H5, respectively, and vary between 154 and 204 kJ/mol for all studied structures. For our further applications (complexation of heavy metals) the most interesting are orange and red regions (negative potential), which are most likely to be involved in the complexation event.

Regarding LIP maps from Fig. 3, the red regions suggest areas where electrophilic attack could happen, thus, atoms from which electron removal (ionization) is easy. By convention, in blue color are illustrated the regions where ionization is relatively difficult to occur. Orange regions (the more susceptible to ionization) present close values between 6.9 and 7.02 eV for all studied compounds, so the results of the complexation event for similarly modified electrodes should be quite similar.

Thermodynamic properties

Thermodynamic properties such as zero-point vibrational energy, enthalpy, constant volume heat capacity, entropy and Gibbs energy have been calculated with DFT method for equilibrium geometry at ground state for *Z* and *E* conformers, over a temperature range between 273.15 and 373.15 K. Except for the zero-point energy (*ZPE*), all depend on temperature. Their calculated values are listed in Tables 6 for 298.15 K. The values of enthalpy, constant volume heat capacity (C_v), entropy (*S*) and Free Gibbs energy (*G*), increase with temperature, in agreement with the enhancement of the molecular vibrational intensities as the temperature rises [22]. Obtained thermodynamic functions are given in Table 7 and they are useful to estimate directions of further chemical reactions, by computing those to other thermodynamic functions and relationships.

Table 6*. Predicted thermodynamic properties at 298.15 K for Z and E isomers of L1 –L3*

Parameter\Ligand		L1	L2	L3
ZPE / kJ mol^{-1}	*Z*	554.47	775.17	924.20
	E	554.41	774.98	925.53
ΔH / a.u.	*Z*	-1122.1904	-1240.0481	-1318.6177
	E	-1122.1918	-1240.0423	-1318.6127
C_v / J mol^{-1}	*Z*	182.76	228.52	256.73
	E	182.11	228.27	256.17
S / J mol^{-1}	*Z*	457.89	525.36	563.88
	E	459.87	525.55	563.54
G / a.u.	*Z*	-1122.2424	-1240.1078	-1318.6818
	E	-1122.2441	-1240.1025	-1318.6767

The dependence between calculated thermodynamic properties (enthalpy, constant volume heat capacity, entropy and Gibbs energy) and temperature were fitted by quadratic equations and the correlation fitting factors (R^2) vary between 0.9951 and 1. The obtained values for R^2 show very good correlation of thermodynamic parameters and their fitting equations (Table 7).

The observed predicted and experimental values for chemical shifts from ^{13}C and ^{1}H NMR given in the Supporting Information, show good correlation for *Z* conformer of all compounds. It leads to the assumption that *Z* conformers are formed by synthesis, as assumed from the experimental procedure [5].

***Table 7**. Fitted thermodynamic parameters for L1 –L3*

Function\ Ligand	L1	L2	L3
ΔH / a.u.	$10^{-7}\cdot T^2+7\cdot10^{-5}\cdot T-1122.2$ (R^2 = 0.9994)	$9\cdot10^{-8}\cdot T^2+10^{-4}\cdot T-1240.1$ (R^2 = 0.9956)	$2\cdot10^{-7}\cdot T^2+2\cdot10^{-5}\cdot T-1318.6$ (R^2 = 1.0000)
C_v / J mol^{-1}	$-6\cdot10^{-4}\cdot T^2+0.5889\cdot T+168.45$ (R^2 = 1)	$-5\cdot10^{4}\cdot T^2+0.6806\cdot T+211.89$ (R^2 = 1)	$9\cdot10^{-6}\cdot T^2+0.7177\cdot T+238.51$ (R^2 = 0.9955)
S / J mol^{-1}	$67\cdot10^{-4}\cdot T^2-3.6019\cdot T+937.43$ (R^2 = 0.9890)	$-10^{4}\cdot T^2+0.9517\cdot T+274.33$ (R^2 = 1)	$-10^{4}\cdot T^2+0.9081\cdot T+303.81$ (R^2 = 1)
G / a.u.	$3\cdot10^{-8}\cdot T^2-10^{-4}\cdot T-1122.2$ (R^2 = 0.9978)	$-9\cdot10^{-8}\cdot T^2-2\cdot10^{-4}\cdot T-1240.1$ (R^2 = 0.9988)	$-2\cdot10^{-7}\cdot T^2-2\cdot10^{-4}\cdot T-1318.7$ (R^2 = 0.9951)

*All thermodynamic calculations were performed in gas phase.

Electrochemical characterization of compounds

The electrochemical characterization of L1 - L3 compounds has been performed and the redox potentials were evaluated from the electrochemical curves of L1 - L3 azulene derivatives recorded on glassy carbon electrode by: cyclic voltammetry (CV), differential pulse voltammetry (DPV), and rotating disk electrode voltammetry (RDE) in 0.1 M TBAP, CH_3CN. Selected anodic and cathodic CV, DPV, and RDE curves recorded in millimolar solutions (0 – 2 mM) of L1 - L3 in 0.1M TBAP in CH_3CN have been shown in Figs. 4-6.

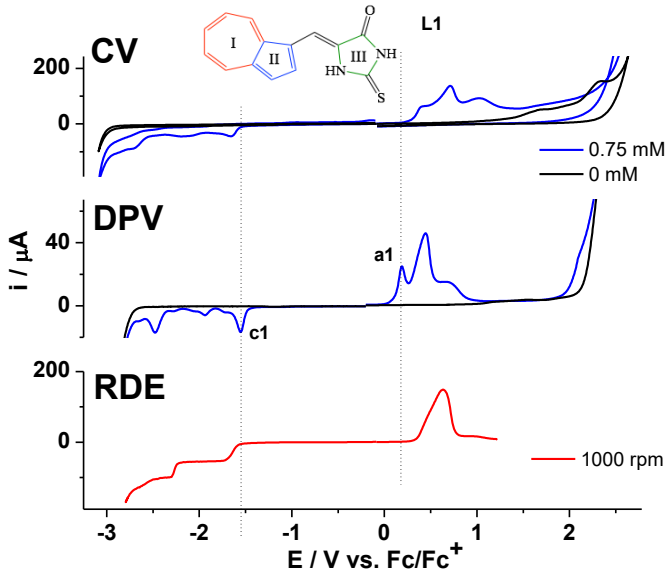

***Figure 4.** CV, DPV, RDE (1000 rpm) curves for **L1** (0.75 mM) in 0.1 M TBAP, CH_3CN.*

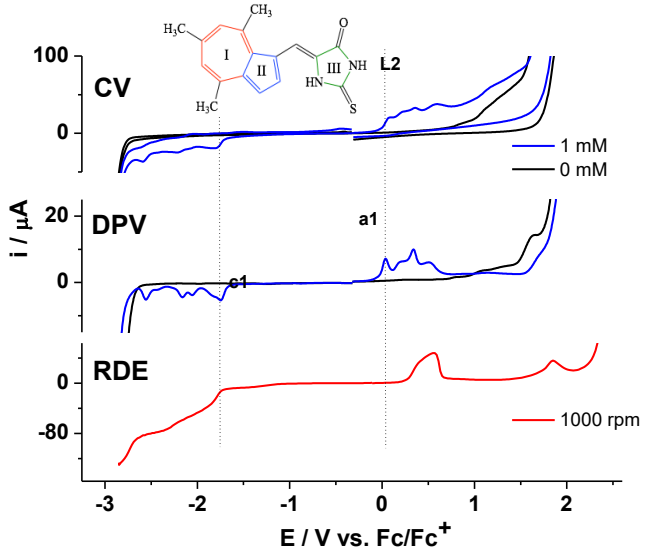

***Figure 5.** CV, DPV, RDE (1000 rpm) curves for **L2** (1 mM) in 0.1 M TBAP, CH_3CN.*

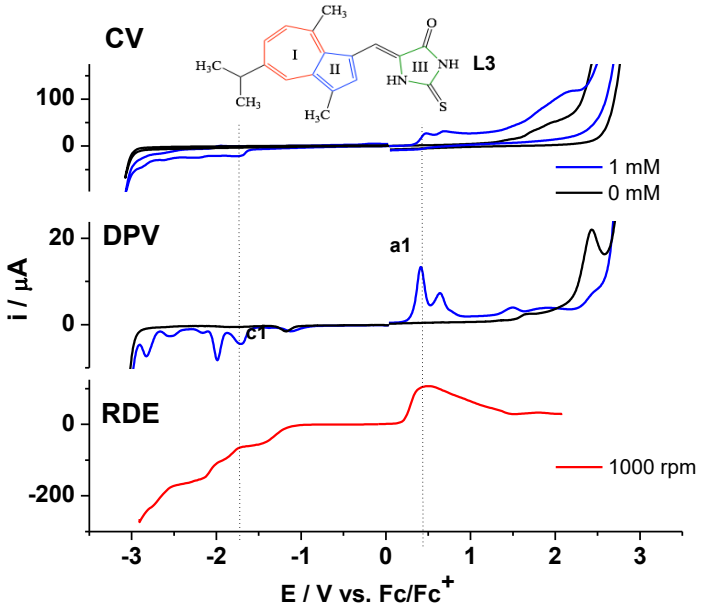

Figure 6. *CV, DPV, RDE (1000 rpm) curves for* ***L3*** *(1 mM) in 0.1 M TBAP, CH_3CN.*

When comparing the curves obtained for these compounds, the following conclusions connected to the electrochemical behavior of L1, L2 and L3 can be drawn:

- Their oxidation potentials for the first oxidation peak (in V) are, respectively, 0.347, 0.297, and 0.266, being ranged in the order: **L3 < L2 < L1**, in correlation with HOMO energies (Table 4). This fact is in concordance with the presence of the electron releasing alkyl groups on azulene moiety in case of L3 and L2. The presence of larger and bulky substituents conducts to an easier oxidation of the ligand.
- Their reduction potentials for the first reduction peak (in V) are, respectively, -1.598, -1.760, and -1.772, being ranged in the order: **L3** < **L2** < **L1**, in correlation with LUMO energies (Table 4). The small differences between the calculated LUMO values and the experimental values of the reduction potentials could be explained by a strong interaction of the ligand with the solvent, which is neglected in quantum calculus. These values also are also connected to the presence of alkyl groups on the azulene structure.
- All the electrochemical processes in Figs. 4-6 are irreversible. While the vinylazulene moiety is more prone to oxidation, the vinylhydantoin part is more likely to be reduced.
- All compounds seem to accumulate on the electrode surface (leading to polymer films) at more positive potentials then the first anodic peak (denoted **a1** on each DPV curve), in agreement with the sharp decrease of the oxidation currents in RDE and DPV curves after reaching this potential.

Electrochemical recognition using modified electrodes

The compounds L1 - L3 were used to prepare modified electrodes by electrochemical polymerization in similar conditions, as mentioned in the experimental part.

The recognition experiments performed with L1, L2, and L3 modified electrodes lead to evaluate the detection limits for Pb(II), Cd(II), Cu(II) and Hg(II) ions. In Fig. 7a are given the stripping curves obtained using poly **L1** modified electrodes for the recognition of different concentrations of Pb(II), Cd(II), Cu(II) and Hg(II) ions, while in Fig. 7b are given the dependences of the stripping peak currents on concentration for the metal ions, as resulted from Fig. 7a, for the most efficient recognition events that has been found with this modified electrode for Cd(II) and Pb(II).

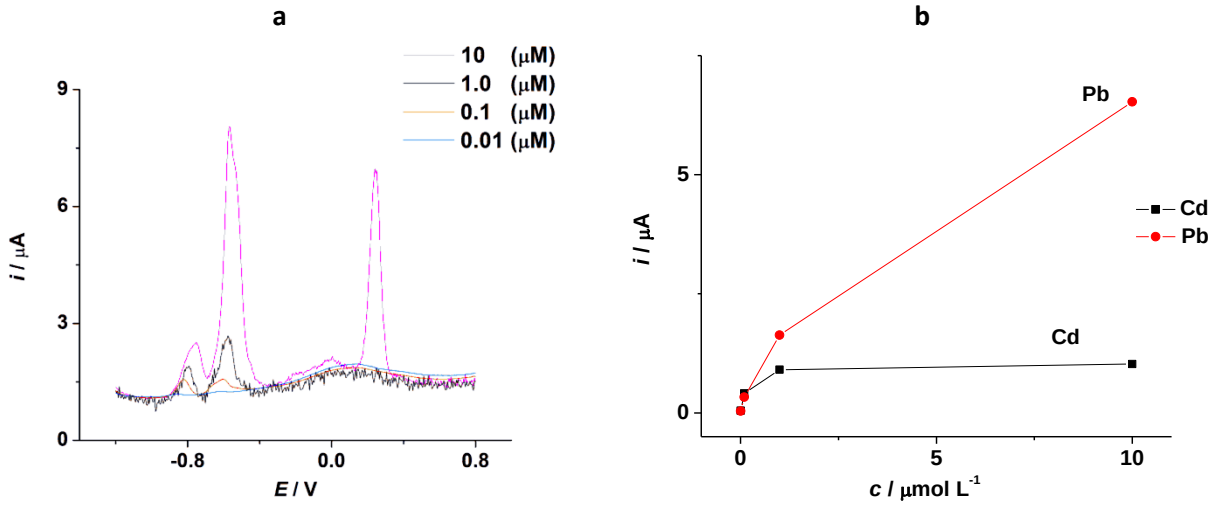

Figure 7. *Stripping curves (a) using L1 modified electrodes for different concentrations of Cd(II), Pb(II), Cu(II) and Hg(II) ions and the corresponding calibration curves (b) for Cd(II) and Pb(II) ions.*

Similar curves have been obtained for the modified electrodes prepared with L2 and L3 ligands, in similar conditions. The detection limits have been estimated for the electrodes modified with L1, L2 and L3 (Table 8). These values show that the best ligand is L1, as by using this ligand, the lowest limits for all tested heavy metals have been obtained.

Table 8. *Estimated detection limits of investigated heavy metal ions for L1 –L3.*

Heavy metal ion / Ligand	L1	L2	L3
Pb(II)	10^{-8}	10^{-6}	10^{-6}
Cd(II)	10^{-8}	10^{-6}	10^{-6}
Cu(II)	10^{-5}	10^{-4}	10^{-4}
Hg(II)	10^{-5}	10^{-4}	10^{-4}

A correlation between ligand molecular descriptors and the obtained detection limits is evident. The best behavior of **L1** can be explained by the fact that **L1** presents the smallest values for HOMO and LUMO energies, and consequently, the highest ionization potential (5.41 eV) and the highest capability to accept electrons (electron affinity, *A* = 2.50 eV) among the three studied structures (Table 4). Also, judging by the molecular electrostatic potential, **L1** structure shows the most negative potential over the oxygen atom, with the most negative value of -203 kJ/mol, so it is the most capable to attract positive heavy metal ions charges, as previously discussed for Fig. 3.

The close values of detection limits for **L2** and **L3** are explained by the similar effect of substituents in **L2** and **L3**, seen in their close values of electron affinity (Table 4). Consequently, their complexing capacity is similar, fact which is in a good agreement with the detection limits obtained for heavy metal ions using these ligands.

Conclusions

Chemical reactivity descriptors were predicted from the DFT calculations. From molecular frontier orbitals energy level diagrams and gaps, it can be concluded that among all studied structures, **L1** is the most stable compound. The oxidation potentials were found to be ranged in accordance with calculated HOMO energies trend, while the variation of reduction potentials *versus* LUMO energies were perturbed by the occurrence of steric effects.

Thermodynamic analysis reveals that all thermodynamic calculated parameters, except the zero-point energy (ZPE), are increasing with temperature. The chosen fitting equations for thermo-

dynamic properties are in a good agreement with calculated data. The NMR experimental and theoretical results supporting each other, being consistently supplemented by computed molecular descriptors and thermodynamic properties. The obtained characteristics are in a good agreement with the detection limits obtained for heavy metals using modified electrodes obtained from these ligands. The corresponding detection limits evaluated for Pb, Cd, Cu and Hg are of about 10^{-8} for Pb and Cd with **L1** and of about 10^{-5} for Cu and Hg. These limits are larger for **L2** and **L3**, which are very close due to the similarity of their structures. They are of about 10^{-6} M for Pb and Cd, and 10^{-4} M for Cu and Hg.

This study contributes to the prediction of specific structures able to coordinate heavy metal ions in view of recognition.

Acknowledgements*: The authors from "Politehnica" University of Bucharest are grateful for the financial support from: Executive Unit for Financing Education Higher, Research Development and Innovation (UEFISCDI) project ID PN-II-RU-TE-2014-4-0594 contract no. 10/2015, PN-II-PT-PCCA-2013-4-2151 contract no. 236/2014 and Romania–China bilateral project 68BM/2016 (CH 41.16.04); the authors from National Institute for Chemical - Pharmaceutical Research and Development – Bucharest, Romania, gratefully acknowledge financial support from project POC ID P_40_406, SMIS 105542.*

References

[1] E. M. Ungureanu, A. C. Razus, L. Birzan, M.S. Cretu, G.O. Buica, *Electrochimica Acta* **53** (2008) 7089-7099.
[2] G. O Buica, E. M. Ungureanu, L. Birzan, A. C. Razus, L. R. Mandoc (Popescu), *Journal of Electroanalytical Chemistry* **693** (2013) 67-72.
[3] S. Lee, J. Oh, D. Kim, Y. Piao, *Talanta*, **160** (2016) 528-536.
[4] P. Niu, C. Fernández-Sánchez, M. Gich, C. Ayora, A. Roig, *Electrochimica Acta* **165** (2015) 155-161.
[5] L. Birzan, M. Cristea, C. C. Draghici, V. Tecuceanu, M. Maganu, A. M. Hanganu, A. C. Razus, G. O. Buica, E. M. Ungureanu, *Dyes and Pigments* **131** (2016) 246-255.
[6] G. L. Arnold, I. G. Lazar, M. D. Pop, G. O. Buica, E. M. Ungureanu, L. Birzan, *UPB Scientific Bulletin, Series B: Chemistry and Materials Science* **79** (2017) 89-100.
[7] G. O. Buica, L. Birzan, V. Tecuceanu, A. C. Razus, G. L. Arnold, E. M. Ungureanu, *Electroanalysis* **29** (2017) 93-102.
[8] Y. Shao, L. F. Molnar, Y. Jung, J. Kussmann, C. Ochsenfeld, S. T. Brown, A. T. B. Gilbert, L. V. Slipchenko, S. V. Levchenko, D. P. O'Neill, R. A. DiStasio Jr., R. C. Lochan, T. Wang, G. J. O. Beran, N. A. Besley, J. M. Herbert, C. Y. Lin, T. Van Voorhis, S. H. Chien, A. Sodt, R. P. Steele, V. A. Rassolov, P. E. Maslen, P. P. Korambath, R. D. Adamson, B. Austin, J. Baker, E. F. C. Byrd, H. Dachsel, R. J. Doerksen, A. Dreuw, B. D. Dunietz, D. Dutoi, T. R., Furlani, S. R. Gwaltney, A. Heyden, S. Hirata, C.-P. Hsu, G. Kedziora, R. Z. Khalliulin, P. Klunzinger, A. M. Lee, M. S. Lee, W. Z. Liang, I. Lotan, N.Nair, B. Peters, E. I. Proynov, P. A. Pieniazek, Y. M. Rhee, J. Ritchie, E. Rosta, C. D. Sherrill, A. C. Simmonett, J. E. Subotnik, H. L. Woodcock III, W. Zhang, A. T. Bell, A. K. Chakraborty, D. M. Chipman, F. J. Keil, A. Warshel, W. J. Hehre, H. F. Schaefer, J. Kong, A. I. Krylov, P. M. W. Gill, M. Head-Gordon, *Physical Chemistry Chemical Physics* **8** (2006) 3172-3191.
[9] R. G. Parr, W. Yang, *Density Functional Theory of Atoms and Molecules*, vol. 16. Oxford: Oxford University Press, Oxford, 1989.
[10] C. Lee, W. Yang, R. G. Parr, *Physical Review B* **37** (1988) 785-789.
[11] A. D. Becke, *Journal of Chemical Physics* **98** (1993) 5648-5652.
[12] W. J. Hehre, *A Guide to Molecular Mechanics and Quantum Chemical Calculations*, Wavefunction, Inc. Irvine, CA, 2003.
[13] M. J. Alam, S. Ahmad, *Spectrochimica Acta, Part A: Molecular and Biomolecular Spectroscopy* **96** (2012) 992-1004.
[14] P. Demir, F. Akman, *Journal of Molecular Structure* **1134** (2017) 404-415.

[15] A. Zarrouk, H. Zarrok, R. Salghi, B. Hammouti, S. S. Al-Dey ab, R. Touzani, M. Bouachrine, I. Warad, T. B. Hadda, *International Journal of Electrochemical Science* **7** (2012) 6353-6364.
[16] H. Wang, X. Wang, H. Wang, L. Wang, A. Liu, *Journal of Molecular Modeling* **13(1)** (2007) 147-153.
[17] V.S. Sastri, J. R. Perumareddi, *Corrosion Science* **53** (1997) 617-622.
[18] R. Yankova, S. Genieva, N. Halachev, G. Dimitrova, *Journal of Molecular Structure* **1106** (2016) 82-88.
[19] R. G. Parr, L. Szentpaly, S. Liu, *Journal of the American Chemical Society* **121(9)** (1999) 1922-1924.
[20] M. Hagar, S. M. Soliman, F. Ibid, El S. H. El Ashry, *Journal of Molecular Structure* **1108** (2016) 667-679.
[21] P. Rajesh, S. Gunasekaran, T. Gnanasambandan, S. Seshadri, *Spectrochimica Acta, Part A: Molecular and Biomolecular Spectroscopy* **153** (2016) 496-504.
[22] K. Chandrasekaran, R. T. Kuma, *Spectrochimica Acta, Part A: Molecular and Biomolecular Spectroscopy* **150** (2015) 974-991.

J. Electrochem. Sci. Eng. **8(1)** (2018) 87-100; DOI: http://dx.doi.org/10.5599/jese.487

Open Access : : ISSN 1847-9286

www.jESE-online.org

Original scientific paper

Insights into electrochemical dealloying of Cu out of Au-doped Pt-alloy nanoparticles at the sub-nano-scale

Matija Gatalo[1,2], Primož Jovanovič[1], Francisco Ruiz-Zepeda[1], Andraž Pavlišič[3], Ana Robba[1,2], Marjan Bele[1], Goran Dražić[1], Miran Gaberšček[1,2], Nejc Hodnik[3,✉]

[1]*Department of Materials Chemistry, National Institute of Chemistry, Hajdrihova 19, SI-1000 Ljubljana, Slovenia*
[2]*Faculty of Chemistry and Chemical Technology, University of Ljubljana, Vecna pot 113, SI-1000 Ljubljana, Slovenia*
[3]*Department of Catalysis and Chemical Reaction Engineering, National Institute of Chemistry, Hajdrihova 19, SI-1000, Ljubljana, Slovenia*

Corresponding authors E-mail: ✉ nejc.hodnik@ki.si; Tel.: +386 1 4760 212

Received: December 6, 2017; Revised: December 30, 2017; Accepted: January 8, 2018

Abstract

Pt alloy nanoparticles present the most probable candidate to be used as the cathode cathodic oxygen reduction reaction electrocatalyst for achieving commercialization targets of the low-temperature fuel cells. It is therefore very important to understand its activation and degradation processes. Besides the ones known from the pure Pt electrocatalysts, the dealloying phenomena possess a great threat since the leached less-noble metal can interact with the polymer membrane or even poison the electrocatalyst. In this study, we present a solution, supported by in-depth advance electrochemical characterization, on how to suppress the removal of Cu from the Pt alloy nanoparticles.

Keywords

Electrocatalysis; EFC-ICP-MS; IL-TEM; Pt alloy; ORR

Introduction

The motivation of scientist, in general, is to improve the life quality of people. Still our development and ability to live without a shortage of food, clean water, energy, etc. are dependent on raw materials resources and economics. However, on the other hand, it is limited by the pollution and negative climate changes. Since it has been already recognized that the pollution caused by humankind indeed affects the environment, it is now time to shift the balance towards the sustainable technologies and renewable energy. In the energy sector, this means replacement of fossil fuels by electricity coming from the sun and wind. Since this energy sources are intermittent,

the current grand challenge is to store this clean energy to match the consumption demand. This is achieved by energy conversion like batteries, flow batteries, pump hydro, compressed air, flywheels, etc. or conversion to hydrogen via electrolyzers. Hydrogen can then be elegantly converted back to electricity via proton exchange membrane fuel cells (PEM FC) with only by-products being water and heat [1-3]. This is very useful in the transportation and stationary sector.

In order to increase the PEM FC efficiency, Pt, as cathodic oxygen reduction reaction (ORR), is alloyed with less noble 3D metals like Co, Ni and Cu [1,4-12]. Initial performances of Pt-alloys are already surpassing the US Department of Energy targets [1]. However, their stability is still under debate and is the topic of many current and future studies [13-20]. Three issues are foreseen for Pt-alloys: (i) loss of initially superior ORR activity [13], (ii) formation of unstable porous nanoparticles [9,15] and (iii) poisoning of the PEM FC by the leached less noble metal cations [12,21-23]. It is known that leached metals can cause the increase of the resistance of the polymer membrane and the lowering of the performance of the anode electrocatalysts due to the poisoning of the Pt surface [12,23].

In this study, we have examined the effect of Au doping on dealloying of Cu out of highly active $PtCu_3$ alloy nanoparticles supported on high surface area carbon (hereinafter referred to as Au-doped $PtCu_3$/C). Although this effect is already known in the literature [6,14,24-26], we provide additional insight into this very effective less noble metal removal suppression tactic. We utilize state-of-the-art advanced electrochemical techniques like thin film rotating disc electrode (TF-RDE), electrochemical flow cell coupled to inductively coupled plasma to mass spectroscopy (EFC-ICP-MS) and identical location (scanning) transmission electron microscopy (IL-(S)TEM).

Experimental

Synthesis:

The starting material $PtCu_3$/C – intermetallic partially ordered (ordered shell, disordered core) $PtCu_3$ nanoparticles that are tightly embedded (anchored) into modified carbon support were prepared via a modified sol-gel synthesis using a gelatin precursor [5,14,17,27,28]. Briefly, the synthesis consists of two vital steps, the first being annealing of a non-noble metal precursor (*e.g.*, a Cu precursor) together with gelatine and carbon black to obtain embedded nanoparticles in a porous carbon matrix. In the second part, the Cu from the composite is partly galvanically replaced by a Pt precursor and annealed for the second time. The starting material was prepared in a 5 g batch.

From the starting material, we have then prepared two completely comparable materials which differ only in the small amount of noble metal addition (Au or Pt). In both cases, 100 mg of the starting material was dispersed in 500 mL of 5 mM KCl and purged with Ar for 1 hour while stirring in order to remove the oxygen from the suspension. Afterwards, while continuously purging the starting material suspension with Ar, 500 mL of 40 µM solution of Au or Pt metal salt solution ($HAuCl_4$ or K_2PtCl_4. Approximately 4 mg of Au or Pt) was added drop-wise in a timeframe of 2 hours in order to galvanically displace superficial Cu atoms found at selected spots of the nanoparticles surface. Both noble metal decorated materials were then filtrated, re-dispersed in 0.1 M KOH, filtrated again and re-dispersed 3 additional times in hot Mili-Q water followed by filtration. After the last filtration, the materials were dried overnight at 50 °C.

Both noble metal decorated materials were then placed together in the same furnace and subjected to an additional thermal annealing step at 500 °C for 3 hours in a CO-containing atmosphere (two separate batches of annealing). Prior to thermal annealing in CO, the samples were first purged with Ar overnight to ensure an oxygen-free atmosphere. Furthermore, the

samples were first heated to only 120 °C for 1 hour in order to remove any residual moisture from both samples before moving to 500 °C. Two materials were obtained – (i) Au-doped $PtCu_3$/C and (ii) Pt-doped $PtCu_3$/C.

XRD

The powder X-ray diffraction (XRD) measurements of all samples were carried out on a Siemens D5000 diffractometer with Cu Kα1 radiation (λ = 1.5406 Å) in the 2θ range from 10° to 60° with the 0.04° step per 1 s. Samples were prepared on zero-background Si holder.

Electrochemical evaluation via Thin Film Rotating Disc Electrode (TF-RDE):

Electrochemical measurements were conducted in a two-compartment electrochemical cell in a 0.1 M $HClO_4$ (Merck, Suprapur, 70 %) electrolyte with a conventional three-electrode system controlled by a potentiostat (Compact stat, Ivium technologies). Ag/AgCl was used as a reference and a Pt wire as a counter electrode. The working electrode was a glassy carbon disk embedded in Teflon (Pine Instruments) with a geometric surface area of 0.196 cm^2. Prior to any experiment, the two-compartment electrochemical cell was boiled in 18 MΩ cm^{-1} Mili-Q water for 1 hour, and the electrode was polished to mirror finish with Al_2O_3 paste (particle size 0.05 μm, Buehler) on a polishing cloth (Buehler). After polishing, the electrodes were rinsed and sonicated in 18 MΩ cm^{-1} Mili-Q water for 5 minutes. 20 μL of 1 mg mL^{-1} water-based well-dispersed catalysts ink was pipetted on the glassy carbon electrode completely covering it and dried under ambient conditions. Such preparation resulted in the loading of approximately 25 μg_{Pt} cm^{-2} and was found to be optimal for obtaining high specific activities at 0.9 V_{RHE}. After drying, the electrode was mounted on the rotator (Pine Instruments). The electrode was placed in Ar saturated electrolyte under potential control at 0.05 V_{RHE}. All electrocatalysts were electrochemically activated for 200 cycles between 0.05 and 1.35 V_{RHE} with a scan rate of 300 mV s^{-1}. Degradation measurements were performed after electrochemical activation, each time with a fresh thin film of the electrocatalyst material. The materials were degraded for 10 000 cycles between 0.4 and 1.x V_{RHE} (x = 0, 2, 4) and for 50 000 cycles between 0.4 – 1.0 V_{RHE}. After electrochemical activation and after degradation we exchanged the electrolyte and measured both CO stripping and ORR polarization curve. ORR polarization curves were measured in an oxygen saturated electrolyte with rotation at 1600 RPM in the same potential window with a scan rate of 20 mV s^{-1}. After subtraction of background current due to capacitive currents, kinetic parameters were calculated at 0.9 V_{RHE}. Ohmic resistance of the electrolyte was determined and compensated for as reported in [29] Electrochemical surface area (ESA) was determined by integrating the charge in CO stripping experiments as described in [30]. All potentials are given against the reversible hydrogen electrode (RHE), which was measured before the start of the experiment and at the end. At the end of each experiment, the thin film on the RDE was dispersed in 0.5 mL of isopropanol with the help of an ultrasound bath and later deposited on a TEM grid for ex-situ TEM analysis or wiped from the RDE with a carbon conductive adhesive tapes for SEM-EDX analysis.

Scanning Electron Microscopy: Energy Dispersion X-ray spectrometry (SEM-EDX):

Ex-situ SEM-EDX analysis was carried out with SUPRA 35 VP (Carl Zeiss) that is equipped with Energy Dispersion X-ray Spectrometer Inca 400 (Oxford Instruments). The operational voltage was set to 20 kV, the distance between the gun and the sample was set to 8.5 mm for optimal signal acquisition and areas for SEM-EDX analysis were selected under magnification of 20 000. For statistical relevance, 3 different areas were measured for each sample.

Transmission Electron Microscopy (TEM):

Transmission Electron Microscopy was carried out in a probe Cs-corrected scanning transmission electron microscope Jeol ARM 200 CF equipped with an SDD Jeol Centurio Energy-dispersive X-ray (EDX) spectrometer. The operation voltage was set to 200 kV. High Angle Annular Dark Field (HAADF) images were taken with 68 and 180 mrad for inner and outer semiangles. Convergence angle was set to 25 mrads.

Identical Location Transmission Electron Microscopy (IL-TEM)):

The electrocatalyst suspension (1 mg mL^{-1}) was ultrasonicated for 15 minutes and diluted 10 times (100 uL of the suspension, 900 uL of Mili-Q water). After additional 5 minutes of ultrasonication (diluted suspension), 5 uL of the suspension was deposited on Au-grid (Plano Au finder grid (NH7) coated with a Lacey carbon film). Once dried, the grid was inspected under TEM. Several spots were registered in the finder grid under TEM and STEM. Locations of the spots were recorded at different magnifications to facilitate the afterward tracking. EDX maps and line scans were performed spending the minimum time to avoid any possible beam damage. The grid was afterward removed from the microscope to perform the electrochemical tests as following. After the inspection, the grid was mounted on a glassy carbon disc, embedded in Teflon (Pine Instruments) with a geometric surface area of 0.196 cm^2. Electrochemical activation was conducted in a two-compartment electrochemical cell in a 0.1 M $HClO_4$ (Merck, Suprapur, 70 %) electrolyte with a conventional three-electrode system controlled by a potentiostat (Compact stat, Ivium technologies). The electrode was mounted on the rotator (Pine Instruments). The electrode was placed in Ar saturated electrolyte under potential control at 0.05 V (*vs.* RHE). The electrocatalyst on the Au-grid was electrochemically activated for 200 cycles between 0.05 and 1.35 V_{RHE} with a scan rate of 300 mV s^{-1}. All potentials are given against the reversible hydrogen electrode (RHE). After electrochemical activation, the Au-grid was dipped into fresh Mili-Q water and left to dry at room temperature. Once dried, the gird was once again inspected under TEM and STEM. IL was identified by the low magnification images which hold marked locations of previously analyzed areas on the TEM grid labeled with letters. The images and the EDX spectra are then taken under the same conditions as previously.

Electrochemical flow cell coupled to ICP-MS (EFC ICP-MS)

A replica of BASi electrochemical flow cell (Cross-Flow Cell Kit MW-5052) made of TECAPEEK material was coupled with an Agilent 7500ce ICP-MS instrument (Agilent Technologies,Palo Alto, USA) equipped with a MicroMist glass concentric nebulizer and a Peltier-cooled Scott-type double-pass quartz spray chamber. A forward radio frequency power of 1500 W was used with the following Ar gas flows: carrier 0.85 L min^{-1}, makeup 0.28 L min^{-1}, plasma 1 L min^{-1}, and cooling 15 L min^{-1}. $HClO_4$ (0.1 mol L^{-1}, Merck, Suprapur, 70 %) carrier solution for the electrochemical experiments was pumped at 263 L min^{-1} by using a peristaltic pump into the BASi EC flow cell and then directly into the nebulizer of the ICP-MS. The carrier solution and electrochemical cell were electrically grounded with respect to the ICP-MS to minimize the possibility of ICP-MS response spikes from static charging at the peristaltic pump rollers. The ICP-MS was tuned for high sensitivity to obtain the best possible signal-to-noise ratio for the measurements. The concentration of catalyst suspension was set to 1 mg mL^{-1}. The suspension was drop-casted by micropipette over one of the GC electrodes and stabilized by a 5 µL of Nafion® (5 wt.% water suspension) diluted by isopropanol (1/50). Second GC electrode was used as a counter electrode. The orientation of the working electrode (WE) and counter electrode (CE) was adjusted so that WE was placed after CE in direction of the electrolyte

flow. An electrochemical protocol performed consisted of 200 cycles (300 mV s^{-1}) between 0.05 and 1.35 V_{RHE}.

Monte Carlo simulations

Kinetic Monte Carlo (KMC) modeling was performed by simply applying Arrhenius equation for the overall bond energy of the atom (first: activation energy is depended on bond type; second: the overall bond energy of the atom is rising with number of neighbors). In the iterative loop atom was randomly chosen to perform specific process (dissolution or diffusion) which corresponds to updated crystal mesh. The loop was running until the specific dealloying time was achieved (for more details look in ref. "Atomically resolved dealloying of structurally ordered Pt nanoalloy as oxygen reduction reaction electrocatalyst"). By varying initial chemical compositions, atoms distribution and shape/size of the nanoparticles, obtained by TEM and EDX observations, KMC simulations resulted in different morphological changes.

Results and discussion

We prepared three $PtCu_3$/C analogs: (i) the starting or as-prepared $PtCu_3$/C, (ii) Pt-doped $PtCu_3$/C and (iii) Au-doped $PtCu_3$/C. For the preparation of the last two samples, the first one was used as a precursor. This means that all samples have the same particle size distribution. Since Pt and Au are more noble than Cu [31] the galvanic displacement can occur. Therefore, some surface superficial Cu is replaced by Pt and in the last sample by Au cations form the solution. This results in the removal of less than 1 % of Cu. The additional annealing step is needed for the formation of the Pt or PtAu skin [14]. For this reason, we can also consider that the composition of the three samples is very similar. The idea behind doping of $PtCu_3$/C nanoparticles skin was to study the effects caused by very small additions of Au, and also Pt as a reference point.

First cyclic voltammograms (Fig. 1a), which is a part of the electrochemical activation (EA) protocol of 200 cycles, 300 mV s^{-1}, 0.05 – 1.35 V_{RHE}, performed with TF-RDE shows comparison of Cu dealloying in the first cycle of the EA. By measuring the charge obtained in the first cycle of EA (Fig. 1a), we notice that in the case of both Au and Pt decoration, the total amount of dealloyed Cu is smaller compared to the as-prepared $PtCu_3$/C. This is a direct proof of successful galvanic displacement of superficial Cu. The success of galvanic displacement is further confirmed by the presence of an additional Au peak at approximately 38.5 ^{o} 2θ (Fig. 1c, dash blue), while we cannot observe any additional peaks in the case of Pt decoration which points towards too small size of the Pt clusters (Fig. 1b, dash red). Surprisingly, there is a visible difference in the intensity of both pm3m peaks ($PtCu_3$ ordered phase) upon decorating with both Pt and Au. After annealing, Au doping is shown to have an effect on the bulk structure of the $PtCu_3$ nanoparticles by further decreases the intensity of the peaks corresponding to the pm3m phase, while also slightly broadening the peaks corresponding to the fm3m phase (Fig 1c, blue). The phenomena could be directly correlated to the doping process itself, as it could point towards Au acting as an impurity in the crystal lattice of the $PtCu_3$ nanoparticles and consequently decreasing the average size of a domain. One can also notice that the peak for pure Au disappeared, while there is an appearance of weak new peaks that most likely correspond to the small number of small-ternary nanoparticles. The same phenomena cannot be noticed in the case of Pt doping, where we don't observe any major changes to the crystal lattice upon annealing (Fig. 1c, red). Although we are dealing with very similar size distribution, we observe a huge difference in the case of the electrochemically active surface area (ESA) (Fig. 1d). This is due to the decreased degree of porosity in the case of the Au-doped $PtCu_3$/C analog [25].

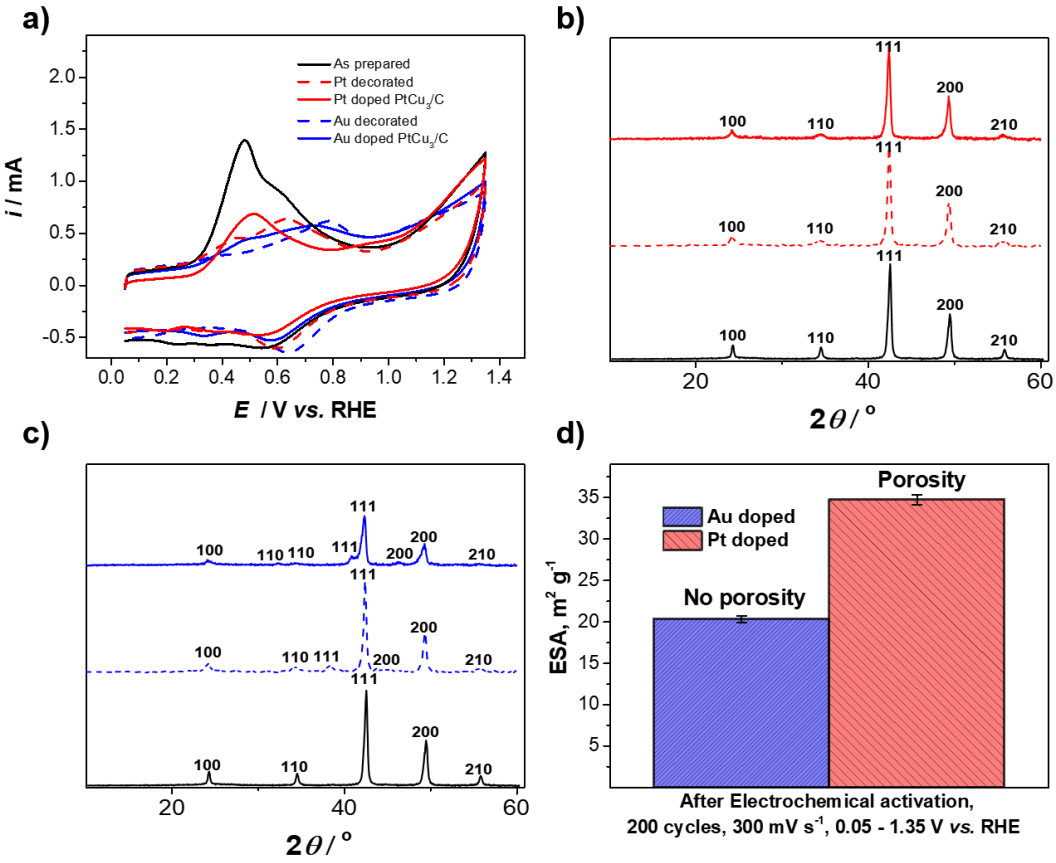

Figure 1. (a) *first cyclic voltammogram of EA of (i) as-prepared $PtCu_3$/C, (ii) decorated $PtCu_3$/C and doped $PtCu_3$/C analogs,* ***(b)*** *and* ***(c)*** *powder XRD comparison (colors and patterns match the legend in figure a) and* ***(d)*** *ESA measurement (from CO stripping) after EA of (i) Au-doped $PtCu_3$/C and (ii) Pt-doped $PtCu_3$/C.*

Formation of porous nanoparticles in the case of Pt-doped $PtCu_3$/C analog results in the increase in the ESA. This surface area is, however, not stable due to the coarsening of the porous structure even at mild degradation simulations till 1 V_{RHE} [15]. This is nicely seen from the Fig. 2 where ESA of both analogs after degradation is limiting towards a similar value. Fig. 3a shows the drop of the specific activity of both doped analogs. Au-doped $PtCu_3$/C analog exhibits about 25 % lower initial specific activity. We presume that this is due to the increased activity of the porous nanoparticles on account of the confinement effect [32]. However, as can be seen in the same figure, the specific activity is decreasing faster for the Pt-doped sample. This is because of the increased loss of Cu and the fact that porous particles are not stable [15]. The trend indicates that further degradation would result in the faster loss of specific activity, as well as ESA of the Pt-doped $PtCu_3$/C analog.

Removal of the Cu from the two doped $PtCu_3$ electrocatalysts was measured by energy-dispersive X-ray spectroscopy detector in the SEM (SEM-EDX). In Fig. 4 it is clearly seen that Au-doped $PtCu_3$/C analog losses much less Cu upon EA and also upon all follow-up degradation protocols. EFC-ICP-MS measurements (Fig. 5a) directly prove the enhanced retention of Cu from the Au-doped $PtCu_3$/C analog. Leached Cu cations present a serious threat to the real application of PEM FC. It can increase the internal resistance of polymer membrane and can also poison the electrocatalyst active Pt surface [1–4]. And on the other hand, retention of Cu is essential to sustain enhanced ORR activity via ligand and/or strain effects [13]. The negative effect of Cu dealloying under long-term PEM FC operating conditions (*e.g.*, simulated via degradation protocol of 50 000 cycles, 0.4 – 1.0 V_{RHE}, 1 $V\ s^{-1}$) can be visible in the change of the slope of ORR polarization curve (Fig. 5b) in the case of Pt-doped $PtCu_3$/C analog.

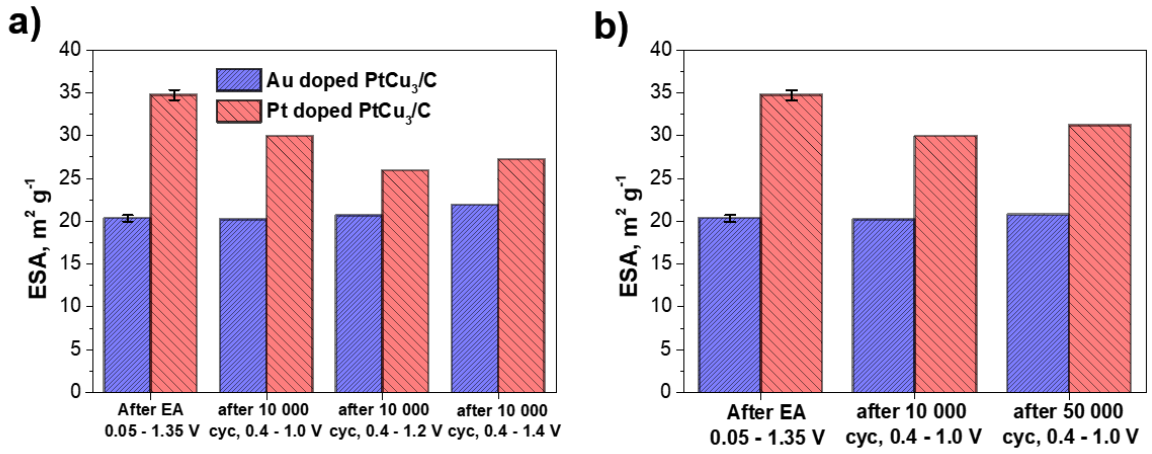

Figure 2. *The absolute decrease of ESA of the two doped $PtCu_3$ analogs: Au-doped $PtCu_3$/C and Pt-doped $PtCu_3$/C upon different degradation protocols.* ***(a)*** *Comparison of ESA for both analogs when varying the upper potential limit of the degradation protocol (0.05 – 1.X V_{RHE}, X = 0, 2, 4), while keeping number of cycles constant and (b) comparison of both analogs when varying the number of cycles (10 000 and 50 000), while keeping the upper potential limit of the degradation protocol constant. Both analogs were electrochemically activated prior to each degradation protocol.*

Such a change in slope can be explained by the redeposition of dealloyed and subsequently underpotentially deposited Cu (Cu_{UPD}) [21]. Furthermore, when comparing CO stripping of Pt-doped $PtCu_3$/C, a slight but clear decrease in ESA is observed (Fig. 5c,d). That further proves the sintering of the pores even under mild degradation conditions. On the other hand, the slope of ORR polarization curve in the case of Au-doped $PtCu_3$/C analog hasn't changed (Fig 5b). This further proves the benefit of higher Cu retention. Additionally, full ESA has been retained (Fig. 5d) in comparison to the CO stripping experiment after EA (Fig. 5c).

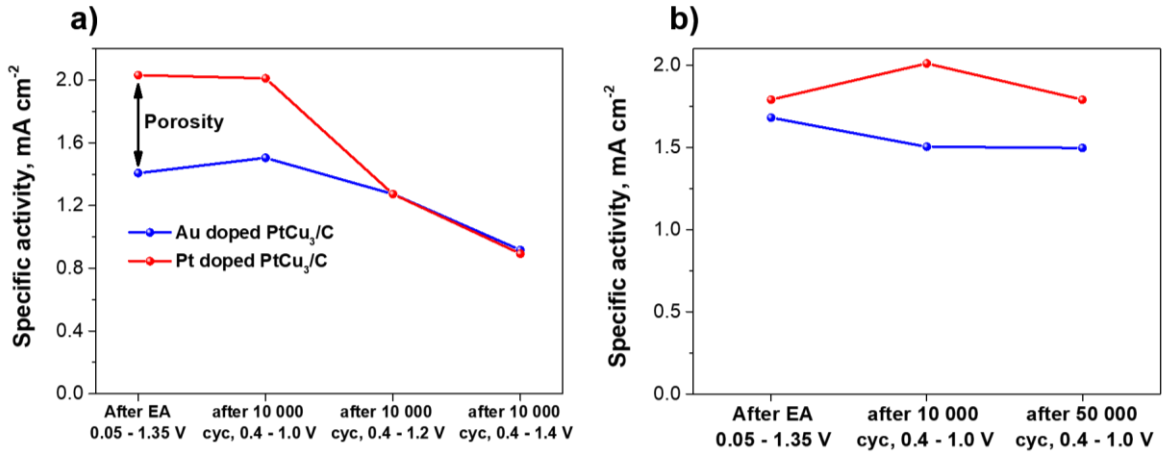

Figure 3. *Loss of specific activity of the two doped $PtCu_3$ analogs Au-doped $PtCu_3$/C and Pt-doped $PtCu_3$/C upon different degradation protocols.* ***(a)*** *Shows comparison of specific activity for both analogs when varying the upper potential limit of the degradation protocol (0.05 – 1.X V_{RHE}, X = 0, 2, 4), while keeping number of cycles constant and* ***(b)*** *shows comparison of both analogs when varying the number of cycles (10 000 and 50 000), while keeping the upper potential limit of the degradation protocol constant. Both analogs were electrochemically activated prior to each degradation protocol.*

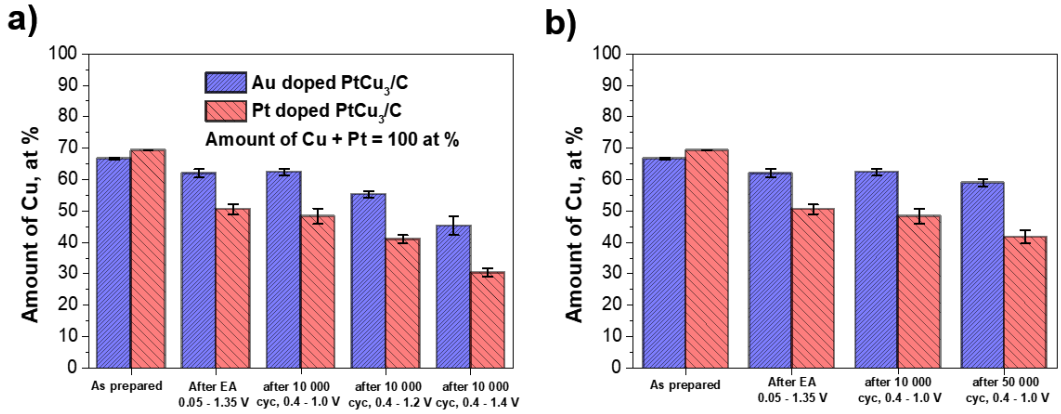

Figure 4. *SEM-EDX measurements of Cu loss, % of the two doped $PtCu_3$ analogs: Au-doped $PtCu_3$/C and Pt-doped $PtCu_3$/C upon different degradation protocols.* ***(a)*** *Shows comparison of Cu loss, % for both analogs when varying the upper potential limit of the degradation protocol (0.05 – 1.X V_{RHE}, X = 0, 2, 4), while keeping number of cycles constant and* ***(b)*** *shows comparison of both analogs when varying the number of cycles (10 000 and 50 000), while keeping the upper potential limit of the degradation protocol constant. Both analogs were electrochemically activated prior to each degradation protocol.*

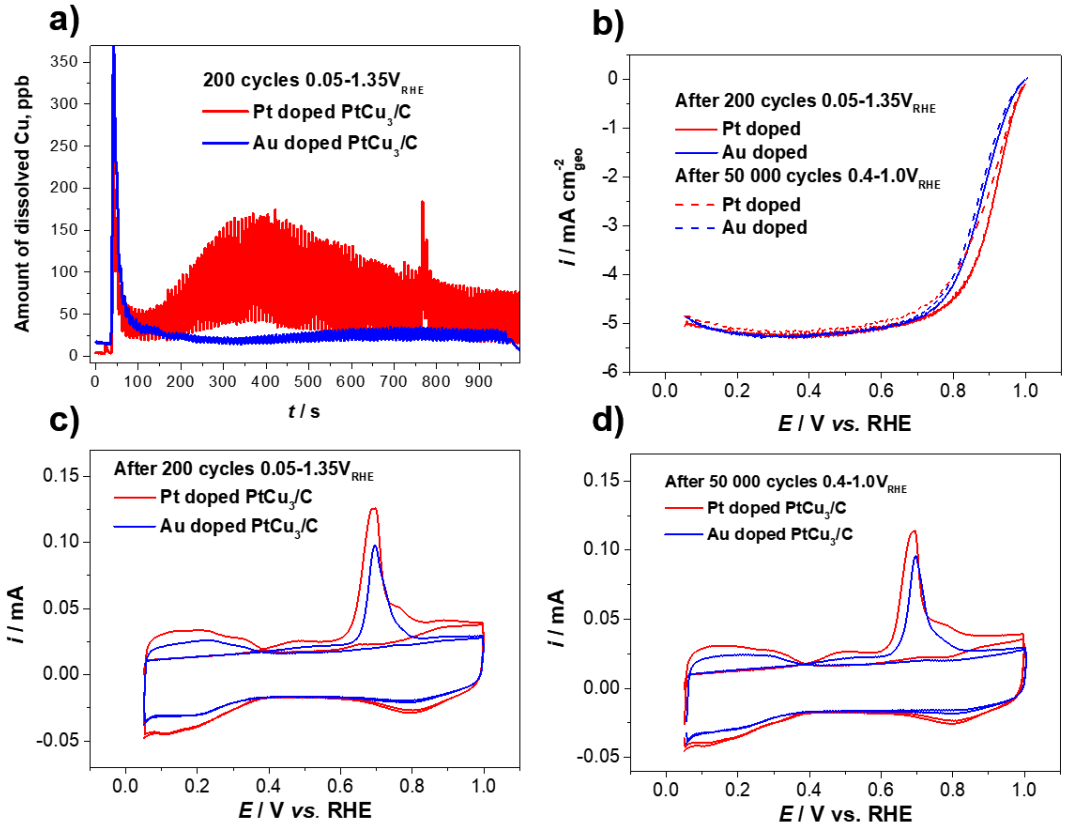

Figure 5. (a) *Shows EFC-ICP-MS measurement of Cu dealloying from the two doped $PtCu_3$/C analogs during 200 cycles of EA (300 mV/s, 0.05 – 1.35 V_{RHE}). (b) Shows polarization ORR curves after both the activation and degradation experiment in O_2 saturated electrolyte (0.1 M $HClO_4$). CO stripping of Pt & Au-doped $PtCu_3$/C electrocatalysts after* ***(c)*** *200 cycles of EA (0.05 – 1.35 V_{RHE}, 300 mV s^{-1}) and after* ***(d)*** *50 000 cycles of degradation (0.4 – 1.0 V_{RHE}, 1 V s^{-1}).*

Transmission electron microscopy investigation confirms the results above on the sub-nano-scale. Pt-doped $PtCu_3$/C analog exhibits extensive porosity formation and shrinkage in diameter as a result of Cu dealloying. In Fig. 6 IL-STEM HAADF images of the same Pt-doped nanoparticle before and after activation dealloying is shown. Line scan EDX profiles clearly confirm the formation of

pores. Careful observation of the Pt line profile (red curve in Fig. 6) reveals the formation of the Pt surface enrichment. Kinetic Monte-Carlo simulations of dealloying process of the same size $PtCu_3$ nanoparticle are in fascinating accordance with the IL-STEM images. As an input parameter, the $PtCu_3$ nanoparticle already had two monolayers of Pt on the surface. If either none, one or three monolayers were chosen, results did not resemble the ones observed in the IL-STEM images [25]. For this reason, we presume that as-synthesized Pt-doped sample has, on average, already 2 monolayers of Pt on the surface. This atomistic insight into $PtCu_3$ dealloying was only possible due to the coupling of the advanced characterization techniques with computer simulations.

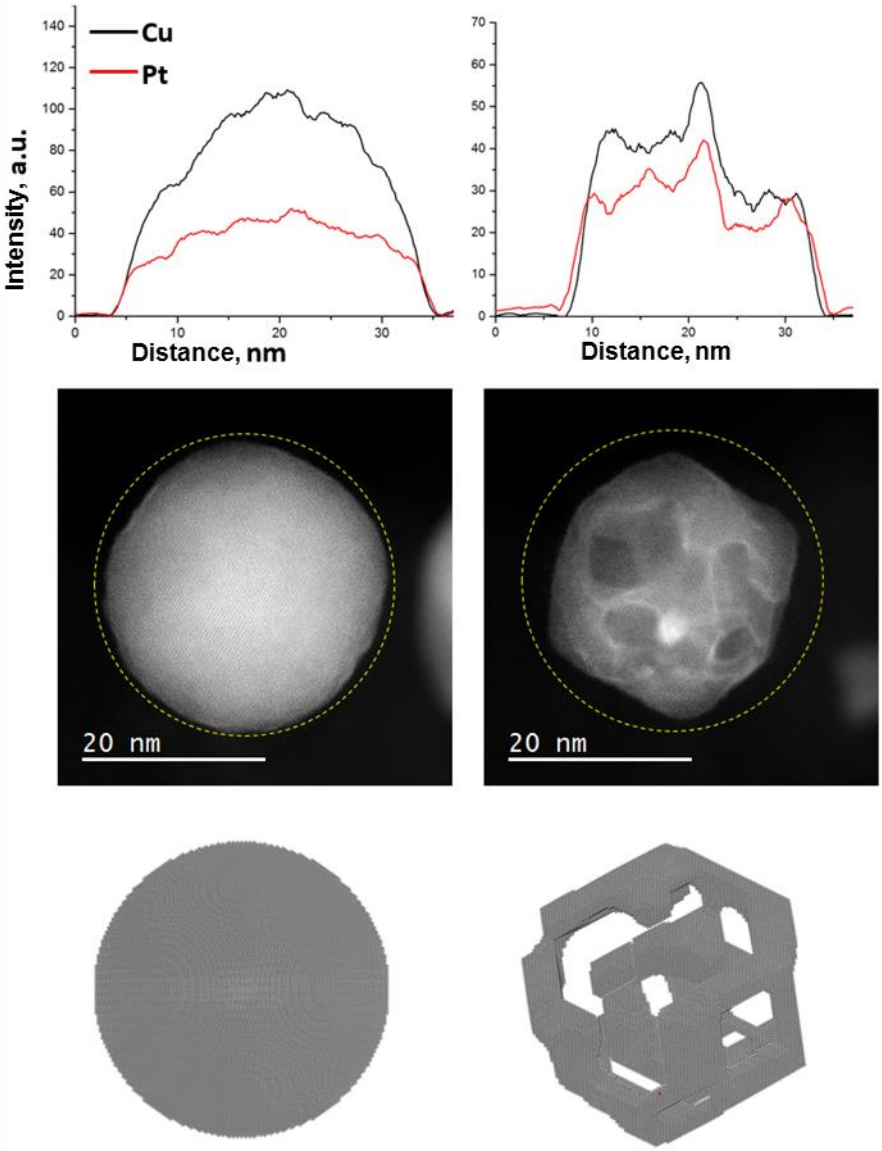

Figure 6. *IL-STEM EDX line scan (top), HAADF image (middle) and Kinetic Monte Carlo simulations (bottom) of the same Pt-doped $PtCu_3$ electrocatalyst before and after EA. An increase in the thickness of the Pt skin is observed after EA, additionally, faceting and pore formation are observed.*

For the Au-doped $PtCu_3$/C analog no porosity is observed (Fig. 7). This is in complete accordance with the previous results showing much lower Cu removal. Careful inspection of the IL-STEM HAADF (yellow dot circle around the particle in Fig. 7) also reveals small shrinkage and the formation of facets [13]. EDX Cu line profile indicates that negligible amount of Cu was removed at the activation protocol, unlike in the case of the Pt-doped sample. Again, the formation of Pt or probably PtAu skin is evident. Monte-Carlo simulation indicates that 4 monolayers of noble atoms (Pt and Au) are present on the surface. As an approximation, here the surface diffusivity of Au and Pt were chosen

to be the same. However, it is known from the literature that Au surface mobility is faster compared to Pt and has, therefore, better ability to "heal" the surface [33]. Therefore it is less probable that the porosity formation takes place even with the same thickness of pure Pt layer [17]. The formation of the facets is also seen in the Monte Carlo simulation.

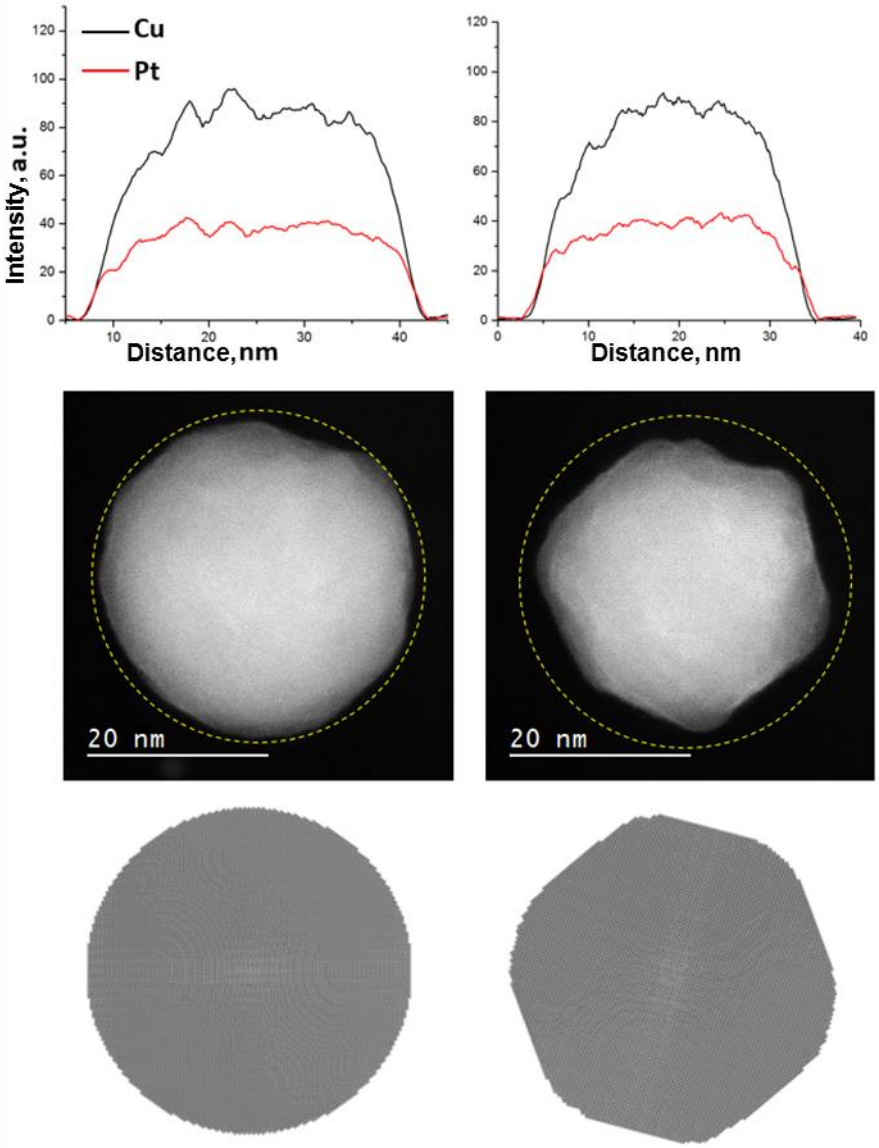

Figure 7. *IL-STEM EDX line scan (top), HAADF image (middle) and Kinetic Monte Carlo simulations (bottom) of the same Au-doped $PtCu_3$ electrocatalyst before and after electrochemical activation. An increase in the thickness of the Pt skin is observed after EA, but only faceting and no pore formation is observed.*

The formation of the PtAu skin is also observed in the IL-STEM and IL-EDX elemental map images of the same Au-doped $PtCu_3$ nanoparticles before and after electrochemical activation protocol in Fig. 8. In the IL-STEM images, the formation of more defined edges and also facets is seen (*i.e.*, faceting) [13,16]. This is in accordance with Fig. 7. In IL-STEM HAADF the intensity of the edges is brighter, which indicates the presence of the metal with higher Z like Pt and Au. This is confirmed by the IL-EDX elemental map. Careful observation also reveals the enrichment of the Pt on the surface even before the dealloying. This is in accordance with the Monte Carlo simulation results in Fig. 7.

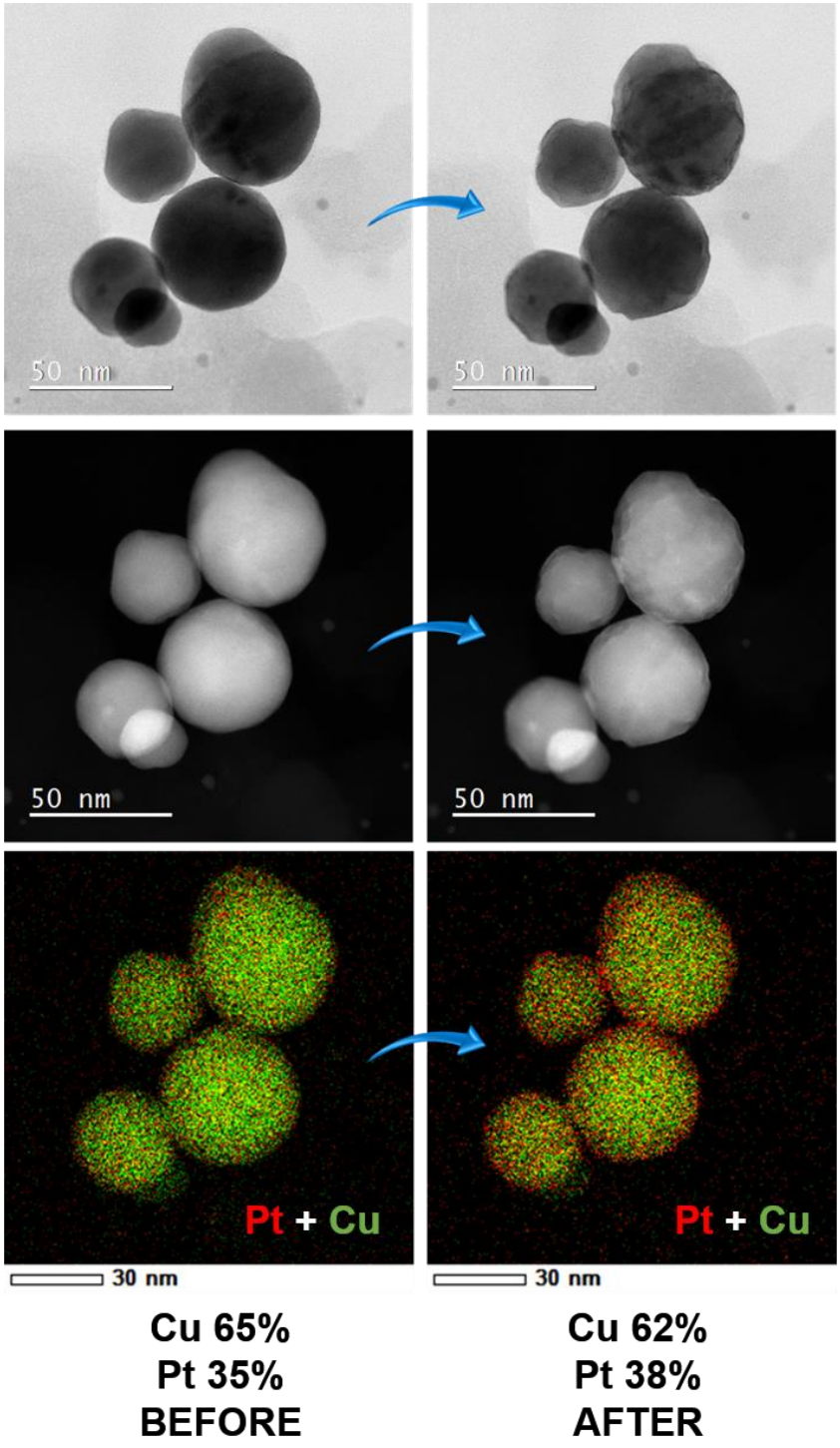

Figure 8. IL-STEM Bright Field (top), IL-STEM High Angle Annular Dark Field (middle) and EDX elemental mapping (bottom) of the same Au-doped $PtCu_3$ electrocatalyst before and after EA. Notice the etching of the surface in the particles and the increase of Pt skin thickness after EA.

In the Fig. 9 the exact atomic composition of the representative activated Au-doped $PtCu_3$ nanoparticle is measured with longer EDX elemental mapping and EDX line scan exposure. This was, however, avoided in the IL-EDX experiments to prevent alteration or damage of the nanoparticles structure by the electron beam. This is also the reason why Au signal could not be distinguished from the dominant Pt signal. Au is distributed over the entire crystal lattice of the nanoparticle. However, it can be presumed from the flat shape [34] of the Au line scan (Fig. 9c) that the concentration of Au lowers when moving from the surface towards the core. If Au was uniformly

distributed, Au line scan would resemble the shape of the Cu scan. We can also distinguish that the surface is formed from at least 5 monolayers of PtAu skin (Fig. 9b).

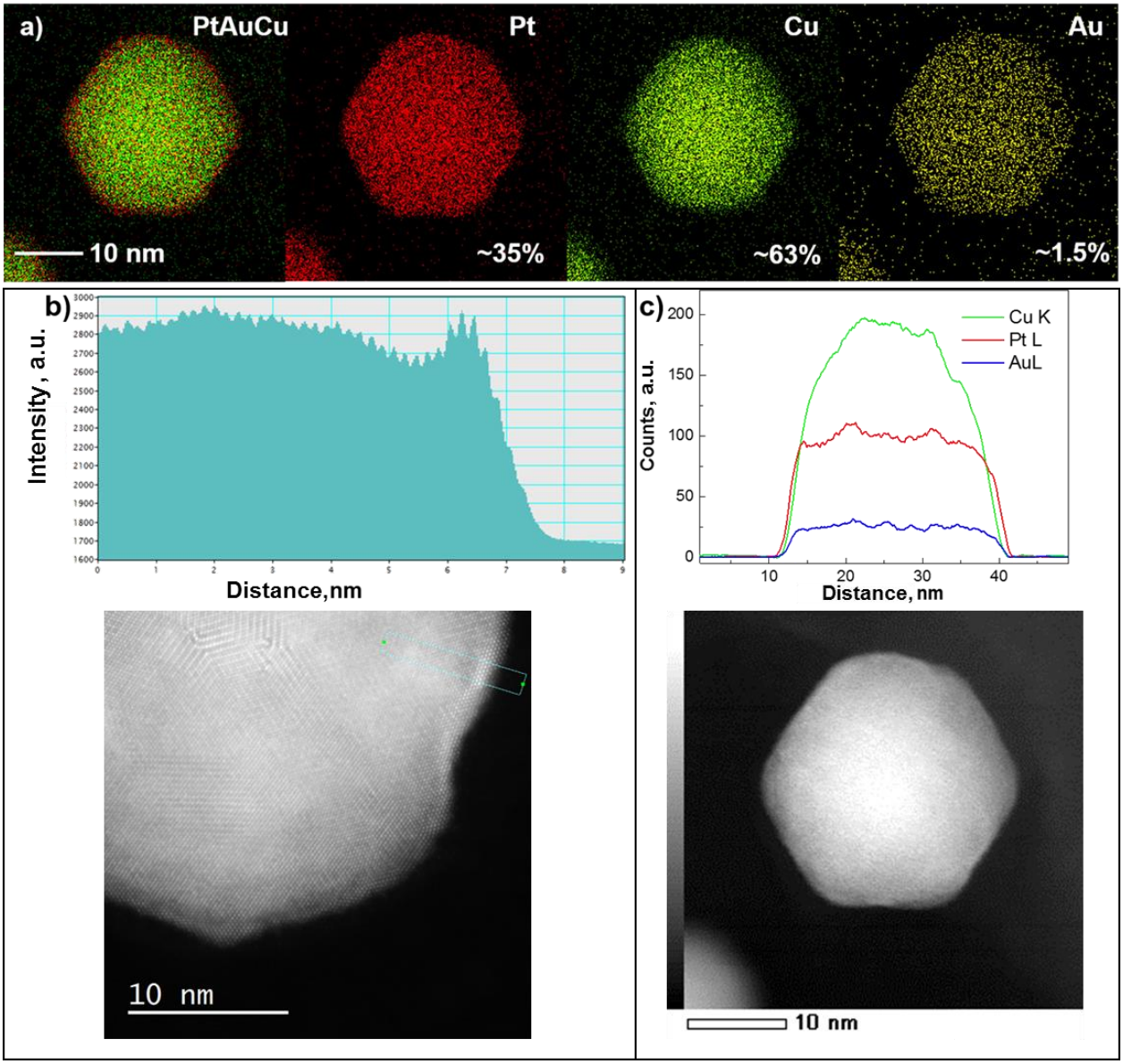

Figure 9. (a) *EDX elemental mapping,* ***(b)*** *HAADF intensity line profile across particle and* ***(c)*** *line elemental scans of the Au-doped $PtCu_3$ dealloyed nanoparticle.*

Conclusions

Two completely comparable materials which differ only in the small amount of noble metal addition (Au or Pt) have been prepared from the initial 5 g bath of highly active intermetallic ordered $PtCu_3$/C electrocatalyst. In contrast to Pt doping (specific activity ≈ 2 mA cm^{-2}_{Pt}), Au doping of the $PtCu_3$/C electrocatalyst results in approximately 25 % lower initial specific activity, as well as lower ESA due to inhibition of porosity formation during 200 cycles of EA (0.05 – 1.35 V_{RHE}, 300 mV s^{-1}). However, upon the degradation till 1.2 V_{RHE} or higher, the difference between both Pt and Au-doped $PtCu_3$/C analogs becomes negligible because Au-doped $PtCu_3$/C analog exhibits much better stability, or in other words much lower stability of Pt-doped $PtCu_3$/C analog. The increased stability of Au-doped $PtCu_3$/C analog is due to the prevention of the porosity formation and due to higher Cu retention. The most impressive result of the current study is the much-improved retention of Cu that presents potentially serious issues in the real PEM FC applications.

***Acknowledgements**: Authors gratefully acknowledge the financial support of the Slovenian Research Agency (ARRS) through the Research Core Funding Programme P2-0152, P2-0393 and Project Z2-8161.*

References

[1] M. K. Debe, *Nature* **486** (2012) 43-51.
[2] N. M. Markovic, *Angewandte Chemie International Edition* **53** (2014) 102-121.
[3] H. A. Gasteiger, S. S. Kocha, B. Sompalli, F. T. Wagner, *Applied Catalysis B: Environmental* **56** (2005) 9-35.
[4] M. Bele, P. Jovanovic, A. Pavlisic, B. Jozinovic, M. Zorko, A. Recnik, E. Chernyshova, S. Hocevar, N. Hodnik, M. Gaberscek, *Chemical Communications* **50** (2014) 13124-13126.
[5] C. Chen, Y. Kang, Z. Huo, Z. Zhu, W. Huang, H. L. Xin, J. D. Snyder, D. Li, J. A. Herron, M. Mavrikakis, M. Chi, K. L. More, Y. Li, N. M. Markovic, G. A. Somorjai, P. Yang, V. R. Stamenkovic, *Science* **343** (2014) 1339-1343.
[6] Z. W. Seh, J. Kibsgaard, C. F. Dickens, I. Chorkendorff, J. K. Nørskov, T. F. Jaramillo, *Science* **355** (2017).
[7] B. Han, C. E. Carlton, A. Kongkanand, R. S. Kukreja, B. R. Theobald, L. Gan, R. O'Malley, P. Strasser, F. T. Wagner, Y. Shao-Horn, *Energy & Environmental Science* **8** (2015) 258-266.
[8] L. Gan, M. Heggen, R. O'Malley, B. Theobald, P. Strasser, *Nano Letters* **13** (2013) 1131-1138.
[9] A. S. Aricò, P. Bruce, B. Scrosati, J.-M. Tarascon, W. van Schalkwijk, *Nature Materials* **4** (2005) 366.
[10] D. Wang, Y. Yu, J. Zhu, S. Liu, D. A. Muller, H. D. Abruña, *Nano Letters* **15** (2015) 1343-1348.
[11] I. E. L. Stephens, A. S. Bondarenko, U. Gronbjerg, J. Rossmeisl, I. Chorkendorff, *Energy & Environmental Science* **5** (2012) 6744-6762.
[12] N. Hodnik, C. Jeyabharathi, J. C. Meier, A. Kostka, K. L. Phani, A. Recnik, M. Bele, S. Hocevar, M. Gaberscek, K. J. J. Mayrhofer, *Physical Chemistry Chemical Physics* **16** (2014) 13610-13615.
[13] M. Gatalo, P. Jovanovič, G. Polymeros, J.-P. Grote, A. Pavlišič, F. Ruiz- Zepeda, V. S. Šelih, M. Šala, S. Hočevar, M. Bele, K. J. J. Mayrhofer, N. Hodnik, M. Gaberščček, *ACS Catalysis* **6** (2016) 1630-1634.
[14] C. Baldizzone, L. Gan, N. Hodnik, G. P. Keeley, A. Kostka, M. Heggen, P. Strasser, K. J. J. Mayrhofer, *ACS Catalysis* **5** (2015) 5000-5007.
[15] C. Jeyabharathi, N. Hodnik, C. Baldizzone, J. C. Meier, M. Heggen, K. L. N. Phani, M. Bele, M. Zorko, S. Hocevar, K. J. J. Mayrhofer, *ChemCatChem* **5** (2013) 2627-2635.
[16] N. Hodnik, M. Zorko, M. Bele, S. Hočevar, M. Gaberščček, *The Journal of Physical Chemistry C* **116** (2012) 21326-21333.
[17] M. Zorko, B. Jozinović, M. Bele, N. Hodnik, M. Gaberščček, *Ultramicroscopy* **140** (2014) 44-50.
[18] M. Oezaslan, M. Heggen, P. Strasser, *Journal of the American Chemical Society* **134** (2012) 514-524.
[19] N. Hodnik, G. Dehm, K. J. J. Mayrhofer, *Accounts of Chemical Research* **49** (2016) 2015-2022.
[20] Q. Jia, D. E. Ramaker, J. M. Ziegelbauer, N. Ramaswamy, A. Halder, S. Mukerjee, *The Journal of Physical Chemistry C* **117** (2013) 4585-4596.
[21] L. W. H. Leung, T. W. Gregg, D. W. Goodman, *Langmuir* **7** (1991) 3205-3210.
[22] Z. Yu, J. Zhang, Z. Liu, J. M. Ziegelbauer, H. Xin, I. Dutta, D. A. Muller, F. T. Wagner, *The Journal of Physical Chemistry C* **116** (2012) 19877-19885.
[23] P. Jovanovič, V. S. Šelih, M. Šala, S. B. Hočevar, A. Pavlišič, M. Gatalo, M. Bele, F. Ruiz-Zepeda, M. Čekada, N. Hodnik, M. Gaberščček, *Journal of Power Sources* **327** (2016) 675-680.
[24] F. Ruiz-Zepeda, M. Gatalo, P. Jovanovič, A. Pavlišič, M. Bele, N. Hodnik, M. Gaberščček, *ChemCatChem* **9** (2017) 3904-3911.
[25] Y. Kang, J. Snyder, M. Chi, D. Li, K. L. More, N. M. Markovic, V. R. Stamenkovic, *Nano Letters* **14** (2014) 6361-6367.
[26] N. Hodnik, M. Bele, S. Hočevar, *Electrochemistry Communications* **23** (2012) 125-128.
[27] M. Bele, M. Gaberscek, G. Kapun, N. Hodnik, S. Hocevar, US9147885B2, 2015.
[28] D. van der Vliet, D.S. Strmcnik, C. Wang, V. R. Stamenkovic, N. M. Markovic, M. T. M. Koper, *Journal of Electroanalytical Chemistry* **647** (2010) 29-34.
[29] K. J. J. Mayrhofer, D. Strmcnik, B. B. Blizanac, V. Stamenkovic, M. Arenz, N. M. Markovic, *Electrochimica Acta* **53** (2008) 3181-3188.

[30] M. Pourbaix, *Atlas of Electrochemical Equilibria in Aqueous Solutionis*, National Association of Corrosion Engineers1966.
[31] J. Snyder, I. McCue, K. Livi, J. Erlebacher, *Journal of the American Chemical Society* **134** (2012) 8633-8645.
[32] I. McCue, J. Snyder, X. Li, Q. Chen, K. Sieradzki, J. Erlebacher, *Physical Review Letters* **108** (2012) 225503.
[33] L. Dubau, J. Durst, F. Maillard, L. Guétaz, M. Chatenet, J. André, E. Rossinot, *Electrochimica Acta* **56** (2011) 10658-10667.

J. Electrochem. Sci. Eng. **8(1)** (2018) 101-110; DOI: http://dx.doi.org/10.5599/jese.476

Open Access : : ISSN 1847-9286

www.jESE-online.org

Original scientific paper

Influence of aging on the heat and gas emissions from commercial lithium ion cells in case of thermal failure

Michael Lammer✉, Alexander Königseder, Peter Gluschitz, Viktor Hacker

Institute of Chemical Engineering and Environmental Technology, Graz University of Technology, Inffeldgasse 25C, 8010 Graz, Austria

Corresponding authors E-mail: ✉michael.lammer@tugraz.at; Tel.: +43 316 873 8795; Fax: +43 316 873 8782

Received: November 22, 2017; Revised: December 27, 2017; Accepted: January 8, 2018

Abstract

A method for thermal ramp experiments on cylindrical 18650 Li-ion cells has been established. The method was applied on pristine cells as well as on devices aged by cyclisation or by storage at elevated temperature respectively. The tested cells comprise three types of $LiNi_{0.8}Co_{0.15}Al_{0.05}O_2$ cells for either high power or high energy applications. The heat flux to and from the cell was investigated. Degradation and exothermic breakdown released large amounts of heat and gas. The total gas and heat emission from cycled cells was significantly larger than emission from cells aged by storage. After aging, the low energy cell ICR18650HE4 did not transgress into thermal runaway. Gas composition changed mainly in the early stage of the experiment. The composition of the initial gas release changed from predominantly CO_2 towards hydrocarbons. A comparable mixture of H_2, CO and CO_2 were emitted in all tests during thermal runaway.

Keywords

Battery characterisation; thermal runaway; gas analysis; heat quantification

Introduction

Recent events like burning phone batteries, notebook computers and battery fires on planes and electric car incidents have shown the intrinsic hazard potential connected to lithium ion battery systems [1–5]. The high energy density of these devices also implies the risk of catastrophic failure in case of malfunction. Safety and risk related issues thus are not only of concern for end users, but also for producers of cells and battery packs and for transportation policy makers [6]. In Li-ion cells the two highly reactive electrodes are separated by a thin polymer separator to prevent direct contact. Ionic conductivity is achieved by an organic aprotic solvent containing the conducting salt. Electrolyte flammability further increases the volatility of this particular electrochemical system. Accumulation of heat within the cell, *i.e.* either excessive external heat influx or heat generation

surpassing the ability of dissipation, poses a serious threat to the integrity of the device [7,8]. Thermally induced degradation processes comprise the evolution of gas from evaporation and degradation of the electrolyte, melting of the separator leading to internal short circuits, changes of the electrodes' structure releasing oxygen and lithium respectively and other fast self-accelerating exothermic reactions leading to thermal runaway [9–14]. Lithium ion cells not only offer a higher energy density but also more resistance towards aging than other types of electrochemical secondary cells like Pb-acid batteries and NiMH systems [15–17]. Aging affects the overall capacity by loss of active material and decay in conductivity and reactivity. After reaching their end of usability, Li-ion cells are still reactive and potentially dangerous devices though.

Due to their importance and intrinsic risks, lithium ion cells and battery systems are subjected to rigorous testing. Most of these tests provoke thermal issues by short circuiting, heating, decay of components or combinations of these damaging effects. Widely applied mechanical testing methods involve dropping cells from defined altitudes (drop tests), crushing or piercing cells with conductive (nail tests) and non-conductive (wedge/crush tests) tools [6,18–20]. Electrical testing is performed by overcharging, deep discharging and externally short circuiting the cells [6,20–22]. Most thermal stress tests are conducted by heating the cells continuously (thermal ramp tests), step-by-step (heat-wait-seek tests) or subjecting the devices to thermal shock [6,9,10,23,24]. Investigation of thermal characteristics, especially heat flux, is typically performed using calorimetric methods like cone calorimetry or accelerated rate calorimetry (ARC) [8,24–28]. Most commonly, tests are conducted on a single cell level [29–31], but fire tests on battery packs and full size electric vehicles are also reported in the literature [32]. In these tests, cone calorimetry is usually employed to gain insight into the burning and fire evolution under air atmosphere [33]. Thermal degradation of battery components and single cells is performed using adiabatic calorimetry. The complex nature and high reactivity of lithium ion cells, especially during the fast gas release by rapid degradation reactions, raises the need for specialised equipment and specific operating procedures [33–35].

Investigations into the behaviour of aged cells under thermal stress in comparison to pristine ones are part of this work. Our group compared the heat and gas emissions of commercial cells of the cylindrical 18650 format in previous studies [9,10,36]. In this work, the tested cells comprise pristine devices as well as cells artificially fast-aged by cycling and cells aged by storing them at 60 °C. 80 % of remaining capacity was set as termination criterion for aging. This limit corresponds to the drop-out criterion for automotive application of Li-ion cells. The fully charged cells (state of charge, SoC = 100 %) are heated continuously by an external heat source in order to trigger thermally induced failure. The quantification of heat consumed and released from the device under test is performed at points of rapid temperature change. A time resolved acquisition of the venting behaviour enhanced the understanding of gas evolution. Due to the quasi-adiabatic conditions at the points of interest, reproducible data has been collected. Characteristic events like initial sudden gas release, the onset temperature of exothermic behaviour, the transgression into thermal runaway and the rapid cell deflagration have been identified. These events are subsequently used for accurate gas sampling to gain additional insight into the degradation of lithium ion cells at elevated temperature.

Experimental

A custom made test rig for thermal ramp tests on cylindrical lithium ion cells of the 18650 format was used for all of the experiments. Detailed information on the test rig has been published in RSC

Advances in 2017 [9].The test rig consists of a tube furnace equipped with a stainless steel tubular reactor for heating the cell. Inert gas (N_2) is used for purging the system and as a carrier gas stream for transporting the gaseous emissions towards the gas sampling device. Characterisation of the emission profile and gas sampling are performed by separate experiments on the same cell type. No carrier gas is used for determining the emission profile. The test rig is flushed with inert gas and left at ambient pressure. By switching to a set of communicating vessels, gas emissions directly displace fluid from the tubes. The mass of the displaced water is directly quantified by weighing and directly corresponds to the volume of released gas. A time-resolved characterisation of the gas emission is achieved by this setup.

Gas sampling is achieved by a syringe pump withdrawing a sample from the off-gas stream and transferring it into a sample vial via a multi-port valve. After the sampling operation, the valve is automatically switched and a new vial becomes available for sampling. The previously filled vial is taken to the ex-situ gas analysis by micro-GC (Agilent micro-GC 3000, USA). This method is used to collect gas samples at defined points of interest during the experiment. The first, sudden gas emission (first venting), the consecutive exothermic phase and the terminal venting after thermal runaway are considered points of interest in this work. Figure 1 shows the generic profile of a thermal ramp test.

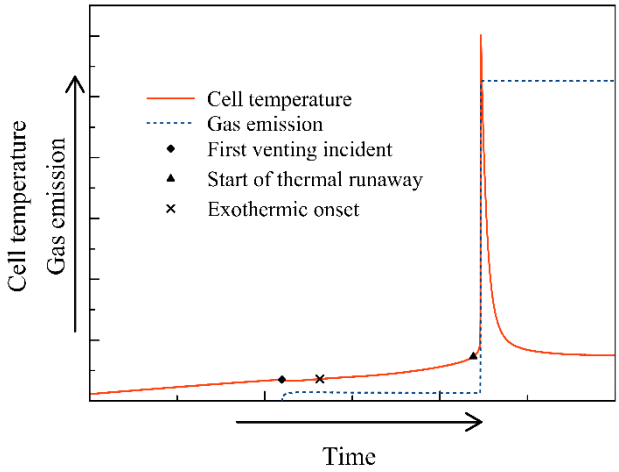

Figure 1. *Generic overview containing the characteristic events on the temperature curve and the corresponding gas emission profile*

The cells tested within this work were NCR18650BF, INR18650-35E and ICR18650HE4. All these cells consist of $LiNi_{0.8}Co_{0.15}Al_{0.05}O_2$ cathodes and graphite anodes. Although NCR18650BF and INR18650-35E are similar in regards of energy density, the cells are working quite differently, as the three types of 18650 cells show different application profiles (Table 1). Cells were used in pristine or artificially aged condition. Aging was carried out either by cyclisation or storing cells at 60 °C until a remaining capacity of 80 % was reached. The cells were cycled four times for determination of the capacity during storage. All cells were prepared by charging to 100 % of state of charge according to the manufacturer's data sheet applying a constant current/constant voltage charging routine. A BaSyTec Battery Test System (BaSyTec GmbH, Germany) was used for conditioning the cells. After charging, the plastic cover was removed, and the cell's mass was recorded. Three type-K thermocouples were fixed to the can by a sheet of glass fibre cloth. This sheet also acted as insulation material preventing short circuiting of the cell within the stainless steel sample holder. The sample holder both allowed reproducible positioning of the cell under test within the tubular reactor and leaving enough space for unhindered gas and particle emission.

Table 1. *Cells tested within the study; the application profile was established on base of the maximum discharge current and energy content calculated from manufacturer datasheets.*

Cell	Mass, g	Capacity, Ah	Energy, J	Application profile
NCR18650BF	44.87	3.35	43404	Long runtime at low power consumption
INR18650-35E	47.70	3.35	45386	High power and high energy applications
ICR18650HE4	45.50	2.50	32416	Short runtime at high power consumption

Flushing the reactor and piping with inert gas (N_2; 1 l min^{-1}, 20 min) purged the system of air. The furnace was preheated to 80 °C. Then a heating ramp of 70 W (corresponding to approx. 0.5 °C min^{-1}) was applied until the terminal venting of the thermal runaway and cell deflagration occurred. Continuous heating led to electrolyte degradation and evaporation, initiating pressure build-up within the can. To prevent uncontrolled cell rupture caused by the pressurisation of the cell by gaseous degradation products, cells of the cylindrical 18650 format are equipped with a safety rupture disk. Breaking of this disk relieved critical pressure. This event of first gas release is denominated first venting within this work. Further application of external heat influx induced a degradative condition where the cell itself became a heat source – the exothermic phase was reached. From the exothermic phase a rapid transgression into the thermal runaway was observable. As there are no specifications on thermal runaway of electrochemical devices found in literature, a self-heating rate of ≥2 °C min^{-1} had been chosen in this work to define the beginning of thermal runaway. This very fast, self-accelerating exothermic breakdown of cell components was characterised by a final release of large amounts of gas and heat, consuming the reactive components of the cell. After this deflagration event, the cell under test cooled down to reactor temperature, as indicated in Figure 1.

Basic information on a cell type was gained by a test at ambient pressure under nitrogen atmosphere with no set gas flow. Any gas release increased the pressure within the system, displacing water from the communicating tubes. This type of experiment yielded the gas emission profile as well as the thermal features of the cell, i.e. the critical temperatures of the first venting, onset of exothermic behaviour, transgression into thermal runaway and the maximum temperature during cell deflagration. Previous studies of our group have shown that the characteristic events are reproducible at the temperatures found for each type of cell [9]. Thus, the follow-up test was conducted using a nitrogen carrier gas stream of 70 cm^3 min^{-1} to transfer the gaseous degradation products from the site of emission to the sampling device. An automated syringe pump was actuated at the characteristic temperatures to withdraw a gas sample at this point. The sample was fed into sealed and argon purged vials by means of a motorised multiport valve. This method combined the timed accuracy with the reproducibility of automatized gas sampling from the vent gas stream. Once the individual vials were filled with vent gas, they were collected, and the *ex-situ* analysis was carried out on a micro-GC system set up for the quantification of H_2, CO, CO_2, CH_4, C_2H_2, C_2H_4 and C_2H_6. Designed as a two-column system, argon and helium were used as carrier gases within the gas chromatograph. This setup made argon a viable filling gas for the “empty” sample vials, as it did not interfere with the analysis.

Results and discussion

Thermal characterisation and characteristic events

The characteristic events were determined by interpretation of the cell’s (self-)heating rate. The first venting was related to the appearance of a negative heating rate, as the Joule-Thomson effect

cooled the cell. The point of inflexion in the rate vs temperature plot indicated the transgression into exothermic behaviour. A (self-)heating rate of ≥2 °C min^{-1} was defined to be the initiation of thermal runaway. An exemplary rate vs temperature plot is shown in Figure 2.

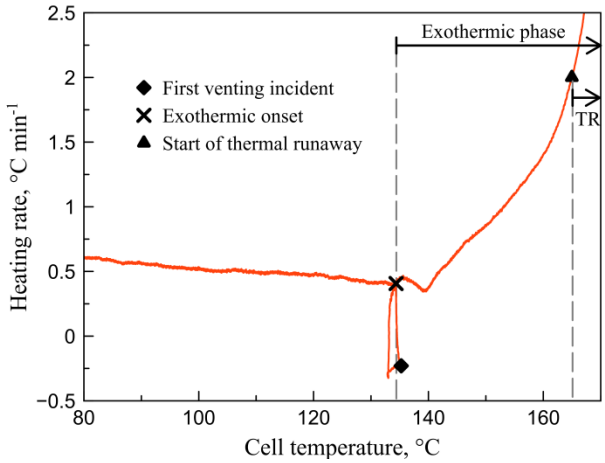

Figure 2. *Rate plot of INR18650-35E (pristine), indicating the characteristic events and the corresponding phases of exothermic behaviour and thermal runaway (TR).*

Calculation of the heat consumption and emission during the first venting incident and the thermal runaway was calculated from the temperature of the cell in relation to the thermal ramp at the respective points due to the quasi-adiabatic nature of these events. An overview of the cell temperature at the characteristic events is given in Table 2. Table 3 offers detailed information on the heat consumption and release as well as the gas emission at the respective events. Figure 3 shows the comparison of the cells under test at different states of aging. Aging effects are clearly visible in the trends of decreasing heat transfer during venting and thermal runaway respectively. The volumetric gas release does not show any clear trend. Heat calculations were performed in reproducible manner in three distinct experiments for each cell.

Table 2. *Temperature of the tested* Cells at the characteristic events*;* Status *indicates whether a cell is pristine* (a) *or aged by either cyclisation* (b) *or storage at 60 °C* (c)*;* T_{VENT} *relates to the cell temperature upon the first venting,* T_{ONSET} *is the temperature during the exothermic onset,* T_{TR} *is the temperature, at which thermal runaway was imminent and* T_{MAX} *is the maximum temperature recorded during thermal runaway.*

Cell	Status	T_{VENT} / °C	T_{ONSET} / °C	T_{TR} / °C	T_{MAX} / °C
NCR18650BF	a	134	124	172	771
INR18650-35E	a	135	115	171	695
ICR18650HE4	a	118	113	204	690
NCR18650BF	b	139	125	177	681
INR18650-35E	b	136	135	175	702
ICR18650HE4	b	116	182	203	373
NCR18650BF	c	138	119	174	618
INR18650-35E	c	136	135	172	687
ICR18650HE4	c	121	112	n.a.	n.a.

Gas release during the first venting is roughly dependent on the capacity of the cell, though the venting characteristic of NCR18650BF (new) does not fit into the scheme. The heat consumption of the first venting (Q_{VENT}) is highly consistent. Though NCR18650BF and INR18650-35E have comparable energy content, INR18650-35E consumed considerably less energy for venting. The significantly lower energy content – indicating the lowest reactivity – of ICR18650HE4 was directly

reflected by the lowest gas emission and heat consumption. The progress of the thermal runaway was consistent in regards of gas and heat release. INR18650-35E also showed lower emissions than the comparable NCR18650BF.

Table 3. *Heat and gas characteristics of the tested cells; Status indicates whether a cell is pristine (a) or aged by either cyclisation (b) or storage at 60 °C (c);* V_{VENT} *and* V_{TR} *give the amount of gas at the first venting and the thermal runaway respectively;* Q_{VENT} *and* Q_{TR} *show the relevant heat transfer;* $Q_{VENT\ REL}$ *and* $Q_{TR\ REL}$ *indicate the amounts of heat for the venting and thermal runaway relative to pristine cells;* V_{TOTAL} *gives the total gaseous emission for the duration of the test*

Cell	Status	V_{VENT} / cm³	Q_{VENT} / J	$Q_{VENT\ REL}$ / %	V_{TR} / cm³	Q_{TR} / J	$Q_{TR\ REL}$ / %	V_{TOTAL} / cm³
NCR18650BF	a	61	-212	-	5261	25541	-	5637
INR18650-35E	a	167	-136	-	5491	23682	-	5680
ICR18650HE4	a	83	-103	-	2899	21126	-	3381
NCR18650BF	b	212	-148	70	4967	22192	87	5246
INR18650-35E	b	151	-134	99	5493	17165	72	5795
ICR18650HE4	b	31	-79	77	172	7876	37	378
NCR18650BF	c	212	-135	64	5242	20624	81	5610
INR18650-35E	c	67	-78	58	5816	14482	61	5879
ICR18650HE4	c	68	-60	58	n.a.	n.a.	n.a.	69

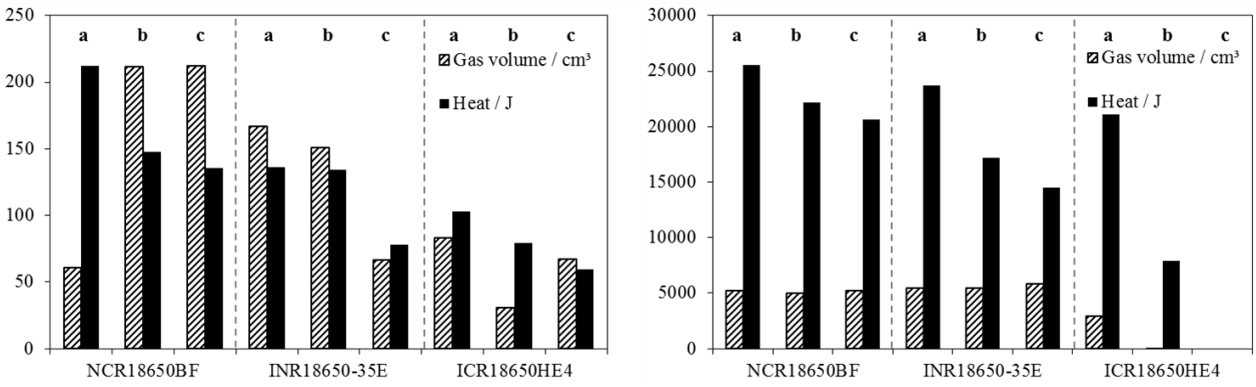

Figure 3. *Volume of released gas and heat transfer for pristine devices (a), cells aged by cyclisation (b) and cells aged by storage at 60 °C (c). The left diagram compares the first venting incident; the right diagram compares the thermal runaway. Note that heat transfer during venting is heat consumption; heat transfer during thermal runaway is heat release.*

This indicates an overall reduced reactivity of this type of cell. The low energy ICR18650HE4 degraded most severely during aging. It showed significantly lower gas and heat emissions and did not transgress into thermal runaway after aging by storage at 60 °C. Though the tested cells have the same electrode chemistry, the respective behaviour under thermal strain is different. Non-only does the electrochemically active material influence this behaviour, but also other components like the separator material and thickness, the susceptibility of the rupture disk, *etc.* Separators with higher thermal stability prevent internal short circuits until higher temperatures are reached, making the cell itself more resistant towards thermally induced failure. Venting at lower internal pressure eases the mechanical strain on the cell components. These factors have an influence on battery safety in addition to reactions within cells of similar chemical composition. In regard of reactivity loss, aging by storage at 60 °C appeared to have a more degrading effect than cyclisation. This is indicated by the lower heat consumption and emission of cells aged this way, as shown in Table 3. Total emission of gas over the duration of the experiment consisted of gas release from the

first venting after the safety rupture disk had opened, the slight gas release during the exothermic phase and the violent venting marking the terminal phase of thermal runaway. The total emission of gas is thus larger than the sum of V_{VENT} and V_{TR}.

Gas analysis at characteristic events

Gas samples were collected at the characteristic events of first venting, during the exothermic phase and after the thermal runaway. Figure 4 depicts the vent gas composition for the characteristic stages of sampling (vertical separation) and different conditions (horizontal separation).

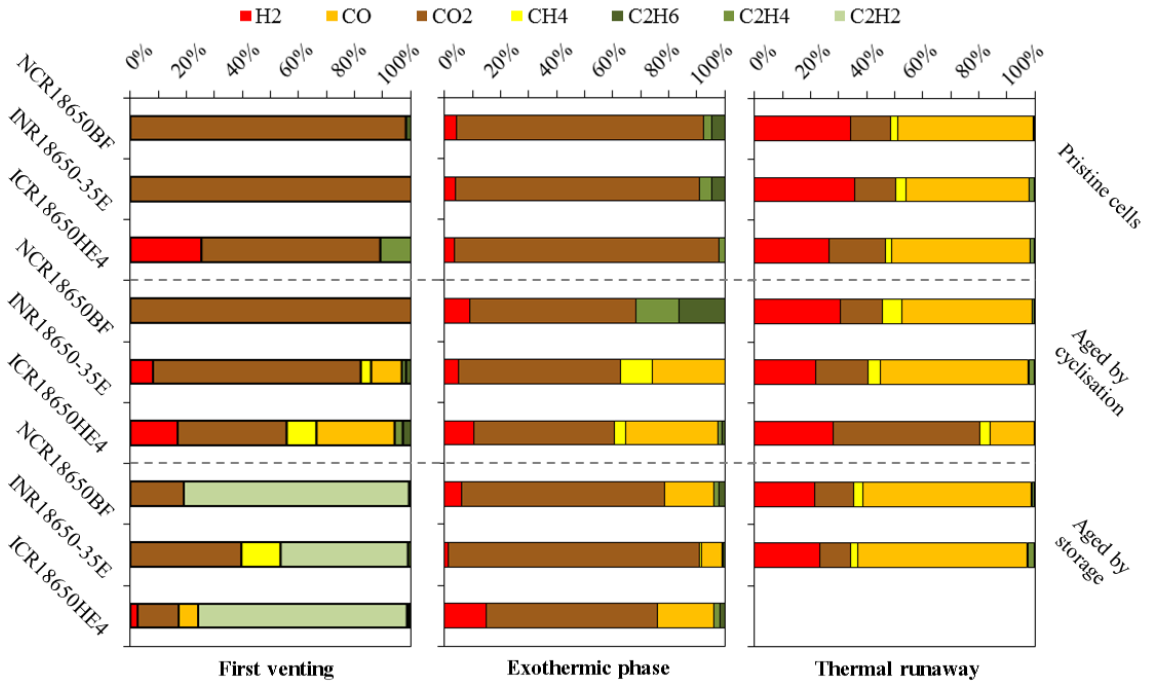

Figure 4. *Vent gas compositions at first venting, exothermic phase and thermal runaway, given for pristine specimens, cells aged by cyclisation and cells aged by storage at 60 °C. Note that ICR18650HE4 did not go into thermal runaway after aging by storage.*

Main component of the vent gas after the first release of gas was CO_2; ICR18650HE4 also released other gases like H_2, CO and CH_4 in larger concentrations than 10 %. Aging by storage drastically changed the vent gas composition at this stage, as most of the detected gas was C_2H_2 for all the cells. The exothermic phase was characterised by large quantities of CO_2. Most aged cells also emitted 10 % or more of H_2 and CO. The cycled NCR18650BF did not exhibit any CO but C_2-hydrocarbons like ethane and ethene. Gas emissions during the final stage of thermal runaway were roughly similar for all the tested cells. ICR18650HE4 showed deviations here, as the cell released larger quantities of CO_2 after aging by cyclisation and did not go into thermal runaway after aging by storage at 60 °C. This means that no gas sampling was carried out.

Gas evolution is determined by numerous factors. Decay and regeneration of the SEI layer at various states of health, reaction temperature as well as pressure within the cells influence the gas evolution and composition. Degradation of components like the organic electrolyte and consecutive gas formation within the cell during aging is not observable by the test setup, until the rupture disk gives in. A gas mixture formed during aging as well as degradation by elevated temperature is collected by the system. CO_2 is mainly deriving from decarboxylation of the organic carbonate electrolyte; CO is attributed to oxidation of carbonaceous species by oxygen released from the oxide electrode. The H_2 emission appears to be a product of the reduction of H_2O deriving from the

combustion of carbohydrates. Detailed mechanisms on the gas formation within the complex system of a Li-ion cell under thermal stress were not in the direct focus of this work and will be the aim of future investigations.

Safety considerations

In regard to safety, cells of large heat consumption during venting are considered as safer due to the possibility of cool-down below a critical level. Low emissions of heat during the thermal runaway also mark safer cells, as less heat is then spread through a battery pack or system. The evolution of gas also has to be considered, as large quantities may both exert mechanical strain on components and pose a danger due to toxic effects, fire and explosion. Large quantities of gas containing high concentrations of flammable gases, *e.g.* H_2, CO and hydrocarbons, which are in part highly toxic (*e.g.* CO), were detected in the vent gas of all cells. Thermal runaway is thus considered a highly dangerous condition also in regards of gas emission. Even cells which have reached the drop-out criterion of 80 % remaining capacity are still potentially hazardous. Safety is not determined by a universal feature – critical conditions transform devices regarded as safe into critically unsafe pieces of technology.

Conclusions

Lithium ion cells are highly susceptible to thermal stress. Inducing thermal stress by means of a tubular furnace allowed studying the associated effects in a detailed and reproducible way. Operation of the test rig under ambient pressure prevented pressure induced side reactions and created a safe and easy way to determine a gas emission profile. An estimation of the characteristic events was achieved based on these data. These events comprise the first venting, i.e. the release of gas from the previously sealed cell, the exothermic phase when the cell itself becomes a heat source and the thermal runaway. Thermal runaway of electrochemical devices is not defined in literature, thus a self-heating rate of ≥2 °C min^{-1} is used in this study. Three types of 18650 format cells were conditioned for operation – NCR18650BF, INR18650-35E and ICR18650HE4. Tests were conducted on pristine cells, devices aged by cyclisation and devices aged by storing them at 60 °C. All tests were carried out on fully charged cells.

The characteristic events were verified by investigating the (self-)heating rate of the cell. A sudden drop to negative rates was directly related to Joule-Thomson cooling initiated by gas expansion form the pressurised can. The inflexion in the heating rate signified the transgression into self-heating and thus the onset of the exothermic phase. Thermal runaway started at a self-heating rate of 2 °C min^{-1} and progressed towards total breakdown of the cell and its components, releasing large quantities of gas and heat. The heat consumed for venting and emitted in the thermal runaway had been calculated from the respective temperatures relative to the thermal ramp. Aging by storage at 60 °C showed the largest influence on the reactivity in regards of the heat and gas emissions. Cells aged this way showed the lowest emission of heat in comparison to new cells – 81 % for NCR18650BF, 61 % for INR18650-35E and no thermal runaway in case of ICR18650HE4. Gas release was only affected in the low energy cell ICR18650HE4. This device degraded the most and after aging by cyclisation it released 6 % of the volume compared to the pristine specimen. As for ICR18650HE4 aged by storage no thermal runaway was observable, no gas emission took place. We suppose that cells of similar chemistry and energy density react differently because of non-electrochemically active components like the separator setup and also because of the early venting behaviour. Thermally resistant separators shift the initiation of catastrophic internal short circuit to

higher temperature; venting releases mechanical strain on the cell components and also cools the cell. Investigation on these components is going to be conducted in the future.

Gas samples were taken at the characteristic events and analysed ex-situ. Analysis showed fairly similar behaviour for all of the cells within the same condition. Aging by storage at 60 °C led to the emission of a large proportion of C_2H_2 during the first venting. C_2H_2 is a gas observed only in traces in all other tests and situations. The evolution of C_2-hydrocarbons appears to be tightly connected to the degradation of electrolyte. The quantity of hydrocarbon emission is larger in cells aged by storage. As these cells exhibit comparable temperature at the first venting incident, it is assumed that the formation is favoured by degradation before the event, i.e. during the aging process. The main component of the vent gas during thermal runaway was CO, making the vent gas a flammable and toxic mixture. It poses a high risk of fire and explosion in regard to the high temperature associated with the event of thermal runaway.

Battery safety cannot be attributed to single features. In respect to cool-down capability during venting, heat emission during thermal runaway and gas evolution during the thermal breakdown, cells can be defined as safe. As not all types of cell show all safety criteria, e.g. a large cool-down as well as low heat emission and the release of low quantities of mainly CO_2, cells are not universally safe. Two methods for aging Li-ion cells to reach the automotive drop-out criterion of 80 % remaining capacity were applied. Aging did decrease the heat release from the cells, but still they posed a threat in case of thermally induced failure. The low capacity ICR18650HE4 cells exhibited the least reactivity after aging by storage, making them somewhat safer under these conditions. This of course comes at the price of low energy density in the first place.

***Acknowledgements**: This work and the project ISALIB is funded by the Austrian Ministry of Transport, Innovation and Technology (BMVIT) and The Austrian Research Promotion Agency (FFG) through the program "Mobilität der Zukunft" (2014-2017). Support by our research and industry partners Kompetenzzentrum - Das virtuelle Fahrzeug and Samsung SDI is gratefully acknowledged.*

References

[1] K. Bullis, *MIT Technol. Rev.* (2013). https://www.technologyreview.com/s/521976/are-electric-vehicles-a-fire-hazard/ (accessed November 15, 2017).
[2] T. V. Wilson, HowStuffWorks (2017). https://computer.howstuffworks.com/dell-battery-fire.htm (accessed November 15, 2017).
[3] A. St. John, CR Consum. Reports (2017). https://www.consumerreports.org/product-safety/whats-behind-the-increase-in-lithium-ion-battery-fires-on-planes/ (accessed November 15, 2017).
[4] A. St. John, CR Consum. Reports (2017). https://www.consumerreports.org/laptop-computers/what-to-do-if-your-laptop-catches-fire/ (accessed November 15, 2017).
[5] E. Weise, USA Today (2016). https://www.usatoday.com/story/tech/news/2016/09/02/samsung-battery-lithium-ion-fire-burning-explosion/89782856/ (accessed November 15, 2017).
[6] V. Ruiz, A. Pfrang, A. Kriston, N. Omar, P. Van den Bossche, L. Boon-Brett, *Renew. Sustain. Energy Rev.* **81** (2017) 1–26.
[7] C. Y. Jhu, Y. W. Wang, C. Y. Wen, C. M. Shu, *Appl. Energy.* **100** (2012) 127–131.
[8] Y. Fu, S. Lu, K. Li, C. Liu, X. Cheng, H. Zhang, *J. Power Sources.* **273** (2015) 216–222.
[9] M. Lammer, A. Königseder, V. Hacker, *RSC Adv.* **7** (2017) 24425-24429.
[10] A. W. Golubkov, S. Scheikl, R. Planteu, G. Voitic, H. Wiltsche, C. Stangl, G. Fauler, A. Thaler, V. Hacker, *RSC Adv.* **5** (2015) 57171–57186.
[11] P. Andersson, J. Anderson, F. Larsson, B.-E. Mellander, ESFSS 2015 2nd Eur. Symp. Fire Saf. Sci. 16 - 18 June 2015 Eur. Univ. Cyprus, Chalmers Publication Library, 2015: pp. 1–5.
[12] C. R. Birkl, M. R. Roberts, E. Mcturk, P. G. Bruce, D. A. Howey, *J. Power Sources* **341** (2016) 1–35.

[13] M. Börner, A. Friesen, M. Grützke, Y. P. Stenzel, G. Brunklaus, J. Haetge, S. Nowak, F. M. Schappacher, M. Winter, *J. Power Sources* **342** (2017) 382–392.
[14] R. Hausbrand, G. Cherkashinin, H. Ehrenberg, M. Gröting, K. Albe, C. Hess, W. Jaegermann, *Mater. Sci. Eng. B Solid-State Mater. Adv. Technol.* **192** (2015) 3–25.
[15] P. G. Balakrishnan, R. Ramesh, T. Prem Kumar, *J. Power Sources* **155** (2006) 401–414.
[16] V. Etacheri, R. Marom, R. Elazari, G. Salitra, D. Aurbach, *Energy Environ. Sci.* **4** (2011) 3243–3262.
[17] R. Zhao, S. Zhang, J. Liu, J. Gu, *J. Power Sources* **299** (2015) 557–577.
[18] D. Doughty, E.P. Roth, *Electrochem. Soc. Interface* **21(2)** (2012) 37–44.
[19] T. H. Dubaniewicz, J. P. DuCarme, *IEEE Trans. Ind. Appl.* **49** (2013) 2451–2460.
[20] R. Spotnitz, J. Franklin, *J. Power Sources* **113** (2003) 81–100.
[21] R. A. Leising, M. J. Palazzo, E. S. Takeuchi, K. J. Takeuchi, *J. Electrochem. Soc.* **148** (2001) A838.
[22] K.-H. Yen, M. Tabaddor, Y. Y. Chiang, L.-J. Chen, C. Wang, *Proceedings of the 44th Power Sources Confernce*, Las Vegas, Nevada, USA, 2010, pp. 14-18.
[23] A. Friesen, F. Horsthemke, X. Mönnighoff, G. Brunklaus, R. Krafft, M. Börner, T. Risthaus, M. Winter, F. M. Schappacher, *J. Power Sources* **334** (2016) 1–11.
[24] T. Waldmann, M. Wohlfahrt-Mehrens, *Electrochim. Acta* **230** (2017) 454–460.
[25] E. P. Roth, D. H. Doughty, D. L. Pile, *J. Power Sources* **174** (2007) 579–583.
[26] H. J. Bang, H. Joachin, H. Yang, K. Amine, J. Prakash, *J. Electrochem. Soc.* **153** (2006) A731–A737.
[27] A. Eddahech, O. Briat, J. M. Vinassa, *Energy 61* (2013) 432–439.
[28] F. Larsson, *Assessment of safety characteristics for Li-ion battery cells by abuse testing*, Thesis, Chalmers University of Technology, Göteborg, 2014.
[29] A. Hofmann, N. Uhlmann, C. Ziebert, O. Wiegand, A. Schmidt, T. Hanemann, *Appl. Therm. Eng.* **124** (2017) 539–544.
[30] E. Sarasketa-Zabala, I. Gandiaga, E. Martinez-Laserna, L. M. Rodriguez-Martinez, I. Villarreal, *J. Power Sources* **275** (2015) 573–587.
[31] Y. Troxler, B. Wu, M. Marinescu, V. Yufit, Y. Patel, A. J. Marquis, N. P. Brandon, G. J. Offer, *J. Power Sources* 247 (2014) 1018–1025.
[32] A. Lecocq, M. Bertana, B. Truchot, G. Marlair, *Proceedings from 2nd International Conference on Fires in Vehicles*, Chicago, USA, 27-28 September 2012, pp. 183-193..
[33] X. Liu, S. I. Stoliarov, M. Denlinger, A. Masias, K. Snyder, *J. Power Sources* **280** (2015) 516–525.
[34] X. Feng, M. Fang, X. He, M. Ouyang, L. Lu, H. Wang, M. Zhang, *J. Power Sources* **255** (2014) 294–301.
[35] E. Schuster, C. Ziebert, A. Melcher, M. Rohde, H. J. Seifert, *J. Power Sources* **286** (2015) 580–589.
[36] A. W. Golubkov, D. Fuchs, J. Wagner, H. Wiltsche, C. Stangl, G. Fauler, G. Voitic, A. Thaler, V. Hacker, *RSC Adv.* **4** (2014) 3633–3642.